ARL

US Army Research Laboratory

A Quantum Network with Atoms and Photons

by Ronald E Meyers, Keith S Deacon, Arnold D Tunick, Qudsia Quaraishi, Patricia Lee

NOTICES

Disclaimers

The findings in this report are not to be construed as an official Department of the Army position unless so designated by other authorized documents.

Citation of manufacturer's or trade names does not constitute an official endorsement or approval of the use thereof.

Destroy this report when it is no longer needed. Do not return it to the originator.

ARL

US Army Research Laboratory

A Quantum Network with Atoms and Photons

by

Ronald E Meyers, Keith S Deacon, and Arnold D Tunick
Computational and Information Sciences Directorate, ARL
Qudsia Quraishi and Patricia Lee
Sensors and Electron Devices Directorate, ARL

REPORT DOCUMENTATION PAGE		*Form Approved* *OMB No. 0704-0188*

Public reporting burden for this collection of information is estimated to average 1 hour per response, including the time for reviewing instructions, searching existing data sources, gathering and maintaining the data needed, and completing and reviewing the collection information. Send comments regarding this burden estimate or any other aspect of this collection of information, including suggestions for reducing the burden, to Department of Defense, Washington Headquarters Services, Directorate for Information Operations and Reports (0704-0188), 1215 Jefferson Davis Highway, Suite 1204, Arlington, VA 22202-4302. Respondents should be aware that notwithstanding any other provision of law, no person shall be subject to any penalty for failing to comply with a collection of information if it does not display a currently valid OMB control number.
PLEASE DO NOT RETURN YOUR FORM TO THE ABOVE ADDRESS.

1. REPORT DATE *(DD-MM-YYYY)* September 2016	2. REPORT TYPE DSI	3. DATES COVERED (From - To)
4. TITLE AND SUBTITLE A Quantum Network with Atoms and Photons		5a. CONTRACT NUMBER
		5b. GRANT NUMBER
		5c. PROGRAM ELEMENT NUMBER
6. AUTHOR(S) Ronald E Meyers, Keith S Deacon, Arnold D Tunick, Qudsia Quraishi, and Patricia Lee		5d. PROJECT NUMBER
		5e. TASK NUMBER
		5f. WORK UNIT NUMBER
7. PERFORMING ORGANIZATION NAME(S) AND ADDRESS(ES) US Army Research Laboratory ATTN: RDRL-CIN-T 2800 Powder Mill Road Adelphi, MD 20783-1138		8. PERFORMING ORGANIZATION REPORT NUMBER ARL-TR-7786
9. SPONSORING/MONITORING AGENCY NAME(S) AND ADDRESS(ES)		10. SPONSOR/MONITOR'S ACRONYM(S)
		11. SPONSOR/MONITOR'S REPORT NUMBER(S)

12. DISTRIBUTION/AVAILABILITY STATEMENT
Approved for public release; distribution unlimited.

13. SUPPLEMENTARY NOTES

14. ABSTRACT

The objective of our Director's Strategic Initiative (DSI) research is to help pioneer a quantum repeater network beyond the US Army Research Laboratory (ARL) environment. The long-term goal is to achieve a quantum repeater network capability for the US Army. Initially, a quantum channel between ARL and the Joint Quantum Institute (JQI) at the University of Maryland - College Park was investigated. Quantum repeaters will allow secure quantum communications to extend to distances where photon attenuation normally becomes a limiting factor, and also allow quantum information to be transmitted and stored. The incipient quantum repeater network development is based on an architecture where nodes are entangled with their nearest neighbors through photon interference, and entanglement chains are established and purified through entanglement swapping. We established a dark optical fiber link between our quantum network laboratory and a quantum laboratory at JQI. We verified that the fiber link can carry entangled photons and quantum information. We constructed the rubidium (^{87}Rb) atomic memory magneto optical trap (MOT) cell and laser controls, and developed protocols, hardware, and software to control the secure teleportation of information between quantum memories at ARL and JQI. Notably, we performed successful in-laboratory proof-of-principle photonic teleportation experiments. In this report, we present initial progress in developing the scientific underpinnings towards implementing an expandable quantum network with atoms and photons (QNET-AP) to facilitate an intra-city quantum network connecting atomic memories.

15. SUBJECT TERMS
Quantum, atoms, photons, entanglement, teleportation, communications, network, memory

16. SECURITY CLASSIFICATION OF:			17. LIMITATION OF ABSTRACT	18. NUMBER OF PAGES	19a. NAME OF RESPONSIBLE PERSON Ronald E Meyers
a. REPORT Unclassified	b. ABSTRACT Unclassified	c. THIS PAGE Unclassified	UU	114	19b. TELEPHONE NUMBER (Include area code) (301) 394-2111

Standard Form 298 (Rev. 8/98)
Prescribed by ANSI Std. Z39.18

ii

Contents

iv

List of Figures

Acknowledgments

We thank the US Army Research Laboratory for support. Ms. Carol Johnson and Ms. Jessica Schultheis provided expert help in editing and formatting this report.

INTENTIONALLY LEFT BLANK.

Executive Summary

The objective of our Director's Strategic Initiative (DSI) research is to help pioneer a quantum repeater network beyond the US Army Research Laboratory (ARL) environment. Research was conducted to establish the scientific underpinnings to facilitate developing a quantum repeater network between ARL and nearby institutions. The long-term goal is to achieve a quantum repeater network capability for the US Army. Initially, a quantum channel between ARL and the Joint Quantum Institute (JQI) at the University of Maryland - College Park was investigated. Quantum repeaters will allow secure quantum communications to extend to distances where photon attenuation normally becomes a limiting factor, and also allow quantum information to be transmitted and stored. The incipient quantum repeater network development is based on an architecture where nodes are entangled with their nearest neighbors through photon interference, and entanglement chains are established and purified through entanglement swapping. In our investigation, we established a dark optical fiber link between our quantum network laboratory and a quantum laboratory at JQI. We verified that the fiber link can carry entangled photons and quantum information. We built the rubidium (^{87}Rb) atomic memory magneto optical trap (MOT) cell and laser controls, and developed protocols, hardware, and software to control the secure teleportation of information between quantum memories at ARL and JQI. In this report, we present the progress achieved towards the quantum network with atoms and photons (QNET-AP) goals of providing the scientific underpinnings to facilitate an intra-city quantum network connecting atomic memories, with the potential to expand to other nearby Government and academic institutions, and in the long-term, intercity and globally via free-space and satellites.

Technical details for selected DSI accomplishments are presented and are organized into distinct sections. We begin by presenting background and fundamental quantum descriptions of photons and teleportation (Section 5). Later we discuss the setup and results from initial probabilistic teleportation experiments conducted by CISD (Section 5.4.7). The CISD team further explored photonic entanglement swapping using an entangled photon source (Section 5.4.9) and a related patent (Section 5.4.10). CISD also investigated wavelength conversion in an atomic Rb cloud (Section 6), new methods to generate entangled photons at selected wavelengths (Section 7), and a study on the environmental effects on polarized photon transmission through installed dark optical fibers (Section 8). Finally in Section 9, we describe some of the progress of the QNET-AP DSI project conducted primarily by the Sensors and Electron Devices Directorate (SEDD) quantum team. We describe research toward 1) building the atomic memory, and 2) testing the polarization stability of the ARL to JQI to ARL fiber-optic line, which will be used to carry the photon "flying qbits" that will entangle dis-

tant atomic memories. The research also includes development of a photon frequency filter for the atomic memory that will help exclude photons at the wrong frequencies.

1. Introduction

In this report, we detail the progress for this Director's Strategic Initiative (DSI) to develop the scientific underpinnings for a quantum network with atoms and photons (QNET-AP). In fiscal year 2012 (FY12), we set up the quantum network laboratory, configured newly acquired equipment, and began to conduct several initial QNET-AP experiments. In FY13, we tested the control of the atomic transitions in the rubidium (^{87}Rb) atomic memory magneto optical trap (MOT) cell, investigated atomic to telecom wavelength conversion, and explored polarization entangled photon transmission to the Joint Quantum Institute (JQI). In FY14, we investigated several schemes for conversion of photons between telecom and atomic frequencies, and investigated potential capabilities for quantum memory and quantum repeater transmissions between the US Army Research Laboratory (ARL) and JQI. We also supported collaborative international work with the Institute of Photonic Sciences (ICFO) that demonstrated frequency conversion between atomic and telecom frequencies. ARL is at the US hub for developing quantum internet technology[1,2] (Fig. 1) and ARL has connections to the key institutions, thus cutting down costs and helping initiate the critical scientific test of loop-hole free quantum nonlocality. National and international experts have collaborated with this DSI. It was recently noted that the Department of Defense (DOD) has the key research capabilities necessary for the US in its strategic race to develop secure quantum communications and computing for US economic and defense well being.[3]
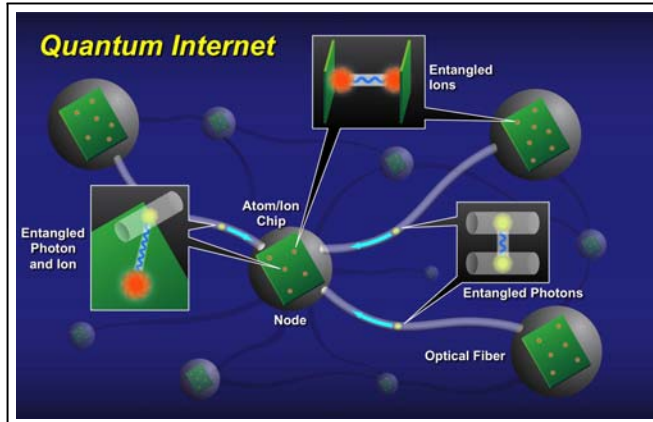
Fig. 1 Quantum internet concept depiction by Ronald E Meyers, Keith S Deacon, and Arnold D Tunick, ARL (2011)[4]

1

2. Objective

The objective of our research is to initiate long-term research to pioneer a quantum repeater network capability beyond the ARL laboratory environment. Research was conducted to establish the scientific underpinnings to facilitate developing a quantum repeater network between ARL and nearby institutions. Initially, a quantum connection between ARL and JQI at the University of Maryland - College Park was investigated. Quantum repeaters will allow secure quantum communications to extend to distances where photon attenuation normally becomes a limiting factor and also allow quantum information to be transmitted and stored. The incipient quantum repeater network development is based on an architecture where nodes are entangled with their nearest neighbors through photon interference, and entanglement chains are established and purified through entanglement swapping. We established the dark optical fiber link between our network laboratory and an atomic laboratory at JQI. We verified that the fiber link can carry entangled photons and quantum information. We built the ^{87}Rb atomic memory MOT cell and laser controls, and developed the hardware and software to control the secure teleportation of information between quantum memories at ARL and JQI. In this report, we present the progress achieved toward completing the QNET-AP goals of providing the scientific underpinnings to facilitate an intra-city quantum network connecting atomic memories, with the potential to expand to other nearby Government and academic institutions, and in the long-term, intercity, and globally via free-space and satellites.

This research is directed toward developing the scientific underpinnings for building a quantum repeater network beyond the laboratory environment. Quantum repeaters will allow secure quantum communication to extend to distances where photon attenuation normally becomes a limiting factor and also allow quantum information to be transmitted and stored. The long-term goal is to entangle distant atomic memories between ARL and JQI, and explore the possibility of entangling hybrid quantum memories.
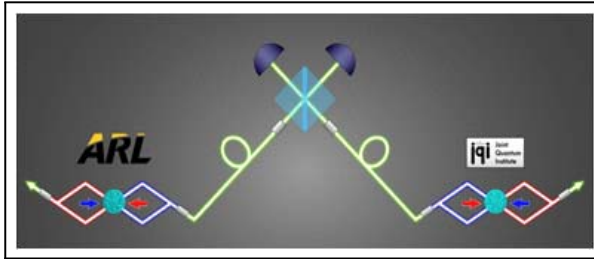
Fig. 2 ARL to JQI atom entanglement scheme. Photon entanglement swapping between distant atom-photon pairs results in distant atomic memory entanglement.

3. Approach

Our DSI quantum repeater network architecture is based on a previously outlined architecture,[5–7] where nodes are entangled with their nearest neighbors through photon interference, and entanglement chains are established and purified through entanglement swapping (Fig. 2). Our approach uses a modified version of the Duan, Lukin, Cirac, and Zoller (DLCZ) scheme,[7] where quantum bits (qubits) are stored in 2 modes of an atomic ensemble. In this scheme, an off-resonant weak Raman scattering process can produce a photon that is entangled with the spin wave stored in the atomic ensemble; the stored quantum information can be retrieved at a later time through the emission of a second photon. Photons emitted from the atomic ensembles at ARL would be converted from the near IR to the telecommunication band and then transmitted to JQI through a dark optical fiber (Fig. 3). The wavelength conversion reduces the attenuation in the fiber and increases the signal strength at the remote location. Initially, we performed the wavelength conversion via four-wave mixing (FWM) in an atomic ensemble, but we also explored difference frequency generation (DFG) in nonlinear crystals such as periodically poled lithium niobate (PPLN). The transmitted photon would then be converted to a different wavelength to interfere with photons emitted from the quantum memory at JQI.

4. Key Results

Below we highlight some of the key results from the DSI investigations. In the sections following the listing of the key results, we elaborate on some of our findings. Other findings have been or will be published in the open literature or as patents, or will be published as supplemental reports for this or follow-on programs. We have listed some of the publications in Section 4.4 Transitions.

1. We successfully established 2 strands of single-mode dark optical fibers connecting the

3

Fig. 3   ARL to JQI dark optical fiber: 5 km direct, 13.5 km by fiber

QNET-AP lab at ARL and the atomic physics labs at JQI (see Fig. 3). The fiber is 13.5 km long (the direct distance between ARL and JQI is 5 km). We have characterized the losses in the fiber and eliminated all major problematic spots along the fiber. We also measured the polarization stability in the fiber over an extended period of time, which is sufficiently stationary with periodic feedback to transmit qubits encoded in photon polarization (Fig. 4). We also established a 6-strand dark optical fiber link between the Computational and Information Science Directorate (CISD) and Sensors and Electron Devices Directorate (SEDD) quantum laboratories.
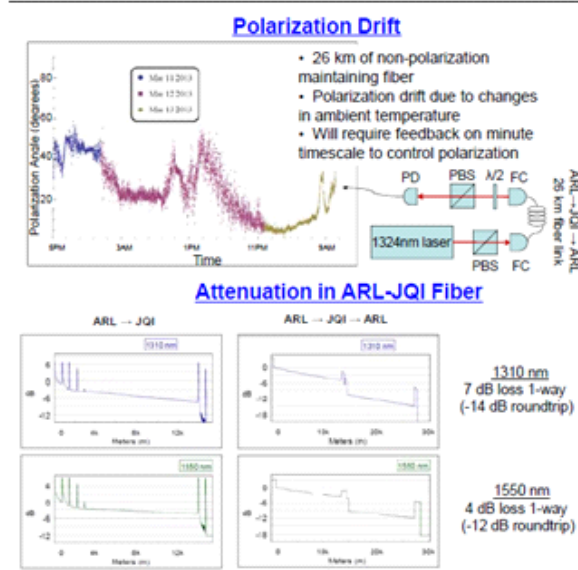
Fig. 4   Photon polarization drift in ARL to JQI using a 27-km dark fiber link

2. Entangled photons were generated in our laboratory and were injected into the optical fiber through a path that went round trip from ARL to JQI. Entangled photons near

4

1550 nm were generated from a commercial fiber source via FWM in a nonlinear fiber. We conducted entangled photon visibility tests that confirmed that the photons were indeed entangled. We characterized the entangled photon transit time, jitter, and survival for the ARL to JQI round trip. We also performed laboratory experiments enabling entanglement swapping between photon pairs created in 2 different time bins over a laboratory optical network.

3. We successfully trapped cold ^{87}Rb atoms in a MOT (Fig. 5), a system that is suitable for quantum memory and quantum frequency conversion via FWM. The 13.5-km distance from ARL to JQI requires the coherence of the quantum memory to be at least 45 μs, which a cloud of ^{87}Rb atoms in a MOT should be able to achieve (~100-μs coherence time). The write step was accomplished through an off-resonant Raman process, for which we had the laser and the optoelectronics to control, and the read step was accomplished through resonant scattering. We achieved initial implementation of the hardware and software for controlling the lasers and electronics for the memory read/write processes.
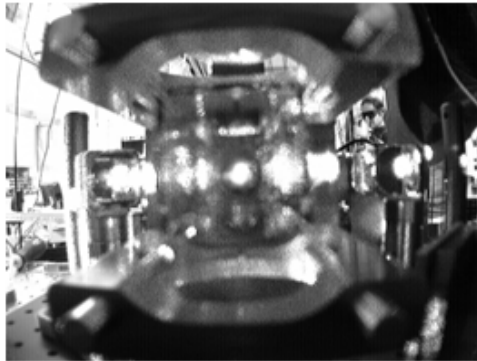
Fig. 5 QNET-AP ^{87}Rb cold atom memory operation shown by light emitted at the MOT center

4. We built a cavity transfer lock for the FWM process to convert single photons at 780 to 1324 nm in an ^{87}Rb MOT by accessing the higher excited electronic states. The cavity transfer lock will enable feedback to the lasers at 2 different wavelengths (795 and 1367 nm) with respect to a 780-nm reference to convert photons to 1324 nm. We also implemented a new MOT cell that is anti-reflection coated for all 4 wavelengths to optimize the signal.

5. We generated correlated photons using 2 ^{87}Rb MOTs and characterized the emitted photons coincidences (see Section 9.1.1).

5

6. We explored environmental effects on polarized light distribution through a dark optical fiber. We found that small temperature changes are enough to significantly affect the polarization property of the propagating photons. Temperature fluctuations cause birefringence in the optical fiber, which results in a phase difference between 2 polarization modes. This degrades the state of output polarization and also makes the quantum state of the photon unstable. In our analysis, a comparison of the measured output state of polarization after propagating 26 km through optical fiber as function of the time of day compared to a predicted theoretical result of the output state of polarization for the same experimental conditions agreed well.

7. We investigated color-controllable polarization entanglement generation in optical fiber at telecommunication and atomic wavelengths. Our analysis indicates that polarization entangled photon pairs can be generated in an optical fiber by a FWM process. The key feature of this entangled photon source is the controllable generation of specified signal and idler colors (wavelengths). In this case, the color (wavelength) selections may be accomplished by varying the pump power. Another important quality of this source is its feature of very low Raman noise photon pair generation. These kinds of color-controllable entangled photon pairs would be useful in certain applications for quantum communications, quantum computing, and quantum imaging.

8. We investigated teleportation and performed in-laboratory probabilistic teleportation experiments. For our laboratory probabilistic teleportation experiments, we used a triple coincidence criteria to record that a valid teleportation occurred. Our preliminary experiments indicated that, based on the triple-coincidence criteria, teleportation was occurring during our experiments. These results indicated that probabilistic teleportation of input states took place over a distance of 2 m in the laboratory. We are designing further improvements to our experimental setup for future follow-on research. We successfully performed experiments of entanglement swapping between entangled photons generated in 2 different time bins. The results were characterized by the quantum density matrix. The quantum density matrix was generated for the 2-photon system using quantum state tomography. We have developed novel designs for measuring Bell states for probabilistic teleportation and have proposed novel schemes for compression of information sent by teleportation between communicating parties. These designs and schemes were filed and subsequently issued as US patents for the Army.

9. We modeled the Rb cold atom diamond configuration to help understand how to achieve high efficiency telecom frequency conversion for quantum communications.

6

The main concern for both frequency down conversion and frequency up conversion to achieve a robust quantum network is the need for high conversion efficiency. While frequency conversion efficiencies that occur in atomic ensembles of Rb via FMW in a diamond configuration are usually very low due to absorption of the input beam, we found in our analysis that the conversion efficiencies can be as high as 90.5% for the down conversion case and 96% in the up conversion case by implementing the idea of electromagnetically induced transparency (EIT). Here, a high transparency regime can be created to overcome the problem of low conversion efficiency. We expect that our proposed configurations will enable progress toward future quantum communication networks over long distances.

4.1 Synergy

CISD and SEDD collaborated on the QNET-AP DSI research, and despite also making significant independent contributions, the synergy from the research contributions is much greater that the contributions of either independently!

4.2 Collaboration

ARL: R Meyers, P Lee, Q Quraishi, K Deacon, A Tunick, D Stack, S Karmakar, J Alexander, I Grissom, V Prieto, N Solmeyer, V Malinovsky, C Adams, T Trout.

Other US partners: JQI - C Monroe, L Orozco, and S Rolston; National Institute of Standards and Technology (NIST) - X Tang; University of Maryland, Baltimore County (UMBC) - Y Shih; Texas A&M University (TAMU) - P Hemmer.

4.3 Coordination with Army, Air Force, and Navy Quantum Programs

Army Research Office (ARO), Air Force Office of Scientific Research (AFOSR), National Ground Intelligence Center (NGIC), Department of Energy (DOE) National Laboratories

4.4 Transitions

4.4.1 Scientific Publications/Presentations/Patents

1. D Stack, Q Quraishi, I Grissom, RE Meyers, KS Deacon, A Tunick, P Lee, Progress toward a quantum memory with telecom wavelength conversion. American Physical Society (5 June 2013).

2. D Stack, P Lee, Q Quraishi, Progress toward a quantum memory with telecom wavelength conversion. SPIE (22 May 2014).

3. D Stack, P Lee, Q Quraishi, Progress toward a quantum memory with telecom wavelength conversion. Proc. SPIE 9123, 91230D-7 (2014).

4. DT Stack, PJ Lee, Q Quraishi, A simple and efficient absorption filter for single photons from a cold atom quantum memory, Optics Express 23, 6882 (05 Mar 2015).

5. N Solmeyer, Q Quraishi, "High teleportation rates for long-distance quantum networks using multiple Rydberg excitations in an atom ensemble," in preparation.

6. RE Meyers, YH Shih, KS Deacon (eds.), Proceedings Quantum Communications and Quantum Imaging XI, SPIE 8875 (2013).

7. RE Meyers, YH Shih, KS Deacon (eds.), Proceedings Quantum Communications and Quantum Imaging XII, SPIE 9225 (2014).

8. RE Meyers, KS Deacon, USPTO Patent US 8503885 (ARL 04-62CIP), Quantum Based Information System and Method (06 August 2013).

9. RE Meyers, KS Deacon, USPTO Patent US 8983303 (ARL 04-62CIP2) Quantum Based Information Transfer System and Method (17 March 2015).

10. RE Meyers, KS Deacon, Patents US 8,811,768, US 8,811,763, US 8594,455 (2013); Invention of quantum ghost imaging encryption, compression and transmission methods.

11. S Karmakar, RE Meyers, Color controllable polarization entanglement generation in optical fiber at telecommunication wavelengths. Optics Express 23(16), 20605-20616 (10 Aug 2015).

12. S Karmakar, RE Meyers, Environmental Effects on QNET-AP, Draft Report, ARL (2013).

13. S Karmakar, RE Meyers, Modeling the Rubidium Cold Atom Diamond Configuration, Draft Report, ARL (2013).

14. RE Meyers, KS Deacon, AD Tunick, Free-space and atmospheric quantum communications. Chapter 10 in Advanced Free Space Optics: A System Approach, Springer Publishing (2014).

15. RE Meyers, ARL Presentations.

16. Q. Quarishi, ARL Presentations.

4.4.2 Developed Patents

We developed patents for improved efficiency of quantum network information transmission including teleportation and frequency conversion:

RE Meyers, KS Deacon, USPTO Patent US 8503885, ARL04-62CIP, Quantum Based Information System and Method (6 Aug 2013) 24 pages.

The following patent relates to the compression of information for transmission, wherein the next quantum state transmitted is dependent on the outcome of the previous transmitted state measurement:

RE Meyers, KS Deacon, USPTO Patent US 8983303 (ARL 04-62CIP2), Quantum Based Information Transfer System and Method (17 March 2015).

This patent extends the compressed information transmission to teleportation communication channels, also includes exfiltration and frequency conversion embodiments with PPLN and other nonlinear media.

4.5 International Collaborations

The following international collaborations were set up with the aid of the US Army Research Development & Engineering Command (RDECOM) International Technology Center (ITC) and ARL to support the QNET-AP DSI objectives. In addition, the international collaborations will help ARL quantum mission objectives.

1. Y Silberberg, Integrated Quantum Optics, Weizmann Institute, Israel; RDECOM ITC-Atlantic/ ARL seedling, Report and visit to ARL (2013).

2. W Hensinger, Ion Trap Chip Fabrication, U. Sussex, UK; ARL–U. Sussex Cooperative Agreement, ARL and RDECOM ITC-Atlantic funded (2012).

9

3. J O'Brien, Quantum Photonic Chip, U. Bristol, UK; Army supported and RDECOM ITC-Atlantic and Air Force European Office of Aerospace Research and Development (EOARD) facilitated., Photonic Based Quantum Chip Delivered to ARL (2013).

4. H de Reidmatten, Photon Frequency Conversion for Rb wavelengths, ICFO, Spain; RDECOM ITC-Atlantic-France Seedling funded, ARL collaborating (2013-2014).

4.6 References

1. Hemmer, P. Closer to a quantum internet. Physics. 2013; 6:62.

2. Kimble, HJ. The quantum internet. Nature. 2008; 453:1023-1030.

3. Wertheimer, M. Director of Research National Security Agency, The Prospects of a Quantum Economy. Oral presentation at the Naval Research Laboratory 2012; 27 August.

4. Meyers, RE, Deacon, KS, and Tunick, AD. Quantum Internet concept depiction. US Army Research Laboratory; 2011.

5. Meyers, RE, Lee, P, Deacon, KS, Tunick, A, Quraishi, Q, Stack, D. A quantum network with atoms and photons. Proc. SPIE 8518. 2012;8518-14.

6. Briegel, HJ, Dur, W, Cirac, JI, Zoller, P. Quantum repeaters: The role of imperfect local operations in quantum communication. Physical Review Letters. 1998; 81:5932–5935.

7. Duan, LM, Lukin, MD, Cirac, JI, Zoller, P. Long-distance quantum communication with atomic ensembles and linear optics. Nature. 2001; 414:413-418.

5. Photon Entanglement and Quantum Teleportation

5.1 Introduction

A new CISD ARL effort is directed at developing the underpinning science for distributed quantum information teleportation networks or quantum internet (Fig. 6). Initial efforts include the development of an entangled photon and atom teleportation testbed network under the DSI entitled "A Quantum Network with Atoms and Photons (QNET-AP)".[1] This research is directed toward developing quantum communications between remote sites that have quantum memories. One of the goals of the US Army demonstration plan is to determine how to entangle distant atomic memories between ARL and JQI of NIST that are separated by kilometers in free-space and along a fiber optical path (Figs. 7 and 8). This distance will further allow for a locality loop-hole free test of the Bell inequalities.[2,3] Another key goal is to develop secure quantum teleportation architectures, schemes, and protocols. This research will lead to the teleportation of quantum information between remote locations and a demonstration of "tamper resistant" quantum communications.
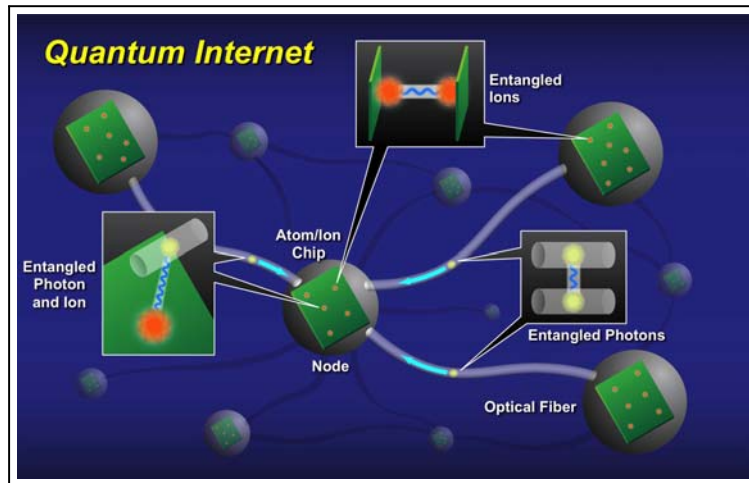
Fig. 6 Quantum internet concept depiction by Ronald E Meyers, Keith S Deacon, and Arnold D Tunick, ARL (2011)[4]

5.1.1 Teleportation Background

Laboratory experiments in quantum communications and teleportation[5,6] are needed to characterize the quantum phenomena, test the assumptions used in quantum information distribution, and optimize protocols that can later be used together for long-distance networking. Recently, there have also been key international experimental demonstrations of the telepor-
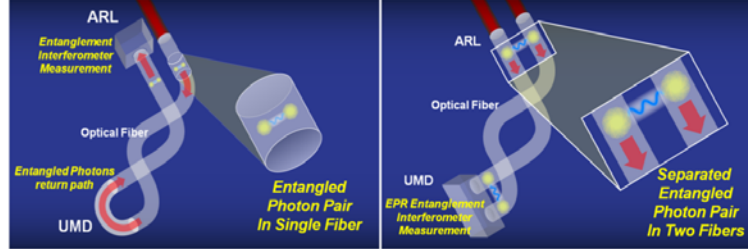
Fig. 7   Depictions of QNET-AP entangled photons ARL to JQI roundtrip and entangled photons ARL to JQI

Fig. 8   CISD dark optical fiber from ARL to JQI (5 km direct, 13.5 km through fiber) enables quantum communications experiments between ARL (CISD-SEDD) and JQI

tation of quantum information using free-space optical quantum communications channels.[6] Two key experiments were performed as precursors to teleportation of quantum information over long distances between ground stations and from the ground to satellites. The first took place in China[7] over a 97-km optical path and used pointing and tracking systems using lasers at 532 and 671 nm coupled to the entangled photon that is at $\sim$788 nm. A GPS was used to enable 1-ns timing accuracy between the remote stations. A wireless classical communications channel was used by Alice and Bob to complete the teleportation protocol. Fidelities of 76 to 89% were reported for the teleportation states that were tested. The article also reported that their acquisition, pointing and tracking (APT) system can be applied to any moving object with high accuracy. The second long-distance free-space teleportation experimental demonstration took place between the Canary Islands of Tenerife and La Palma with a distance of 143 km.[8] A similar pointing to the one above was used and a 1064-nm free-space optical communications link was employed to instruct Bob on how to complete the teleportation protocol. Timing between the islands was coarsely set using GPS and then fine-tuned using an entanglement-assisted clock synchronization[9] to achieve

13

1-ns time accuracy between the locations and a 3-ns coincidence window was used for the measurements. Entanglement fidelities exceeding the classical limit of 67% were reported. Also noted were conditions of extremely bad weather that prevented some experiments from being conducted. Research into the generation of solid-state[10] and other advanced memories with measurement and photon sources will inevitably lead to high-speed network teleportation implementations where the networks are between fixed and moving ground nodes and satellite nodes.[11]

In the following section, we describe the process of quantum teleportation and results from laboratory probabilistic teleportation experiments. While this is a small study, it is indicative of the types of processes that can be used, the problems that may be encountered, and the enormous benefits that can be achieved with quantum communications in general and quantum teleportation in particular. First, we review some of the notation and fundamentals associated with quantum measurements and the mathematics of teleportation. Entanglement is a quantum mechanical phenomenon in which the interacting states of 2 or more quantum systems cannot be described independently. Teleportation involves non-local transfer of information between quantum particles. Teleportation can be between 2 or more entangled particles such as entangled photons or entangled atoms/ions, or can involve hybrid systems that teleport information using both photons and atoms/ions. Quantum teleportation is a qualitatively different method for communication, which has potential benefits of non-locality and improved security well beyond classical communications. Our objective is to help achieve this capability for the US Army and the United States.

5.2   Theory and Technical Background

The fundamentals of quantum physics describe the properties of quantum particles and quantum wavefunctions. Classical particles, such as a baseball, can be described by Newtonian physics where each particle simultaneously has a precise position and momentum. However, quantum particles such as photons and electrons have an uncertainty associated with both position and momentum such that quantum's uncertainty relationship holds, $\frac{\hbar}{2} \leq \Delta x \Delta p$, where $\hbar$ is Planck's constant over 2π.[12,13] Experimental measurements of position and momentum always have a variability in the measured values. Thousands of careful experiments have verified this relationship. Quantum particles are said to have both particle and wave properties. When a photon detector responds with a "click" it is measuring a photon in the sense of a particle. When light passes through a double slit and interferes, the light is exhibiting its interference wave properties. When a series of single photons are passed

through a double slit, the same interference patterns are measured. The way to describe the evolution of quantum properties has relied upon the construct of the wavefunction, Ψ. The wavefunction is in general a complex function having both real and imaginary values. When the wavefunction is multiplied by its complex conjugate, $\Psi^*\Psi$, it forms a positive function, which when normalized, gives the probability of the quantum particle being found in a particular state. In the case of a photon, the probability may describe where the photon is likely to be found in space. It is a peculiar property of quantum physics that the Fourier transform of the wavefunction in configuration space gives the wavefunction in momentum space. Position and momentum are called conjugate variables. In the following section, we discuss the quantum mathematical background and formalism.

5.2.1 Quantum Mathematical Background and Formalism

In this section, we present notation and symbols often used in describing and developing quantum physics, quantum communications, and quantum information. Dirac developed the physics "bra" and "ket" notation. A "bra" is written as $\langle|$ and can be thought of as a row vector (i.e., $\langle A| = [A_1\mathbf{e}_1 + A_2\mathbf{e}_2 + A_3\mathbf{e}_3]$) and a "ket", $|\rangle$, is a column vector $|B\rangle = \begin{pmatrix} B_1\mathbf{e}_1 \\ B_2\mathbf{e}_2 \\ B_3\mathbf{e}_3 \end{pmatrix}$, where the $\mathbf{e}_1, \mathbf{e}_2, \mathbf{e}_2$ are orthogonal unit vectors.[12] An inner product operation using bra-ket notation is written as $\langle A|B\rangle = A_1 B_1 + A_2 B_2 + A_3 B_3$. Another operator that is used when considering composite systems of more than one particle is the tensor, or direct product operator $\otimes$. For a 2-particle composite system, this operation acts as shown:

$$|A\rangle \otimes |B\rangle = \begin{pmatrix} A_1 \begin{Bmatrix} B_1 \\ B_2 \end{Bmatrix} \\ A_2 \begin{Bmatrix} B_1 \\ B_2 \end{Bmatrix} \end{pmatrix} = \begin{pmatrix} A_1 B_1 \\ A_1 B_2 \\ A_2 B_1 \\ A_2 B_2 \end{pmatrix}. \tag{1}$$

Infinite dimensional systems can also be represented in "bra-ket" notation but instead of discrete vector type components the inner, outer, and direct products are integrals over functions.

5.2.2 Quantum Wavefunctions

Wavefunctions describe the probability amplitudes used to describe the state of a quantum particle. Quantum particles are physical entities such as photons, electrons, protons, and neutrons. They are often expressed using Dirac's bra-ket notation, where the state of a

15

particle can be written as

$$|\Psi\rangle = \sum_{i=1}^{N} c_i |\phi_i\rangle \tag{2}$$

where the c_i and ϕ_i are the amplitude and quantum state, respectively. The c_i can be complex valued and ϕ_i can be a measurable state such as a horizontal or vertical polarization for a photon or spin up/spin down for an electron spin. The probability that a quantum particle will be measured in particular states is given by

$$P = \Psi^* \Psi. \tag{3}$$

Wavefunction evolution can be described by a Schrodinger equation, such as the one below:

$$i\hbar \frac{\partial}{\partial t} \Psi(\mathbf{r}, t) = -\frac{\hbar^2}{2m} \bigtriangledown^2 \Psi(\mathbf{r}, t), \tag{4}$$

where $\hbar$ is Planck's constant over 2π, m is mass, t is time, and $\mathbf{r}$ is the position in space. A more accurate wavefunction propagation or evolution equation for free-space or fiber quantum communications would have to include terms added to Eq. 4 to incorporate the effects of absorption, scattering, and index of refraction fluctuations as functions of space and time. It must be kept in mind that turbulence is not stationary, is inhomogeneous, and is a dynamic function of space and time.

5.2.3 Polarization

Polarization in optics is generally associated with the E_x and E_y components of an electromagnetic plane wave propagating in the z direction. In quantum communications, linear polarization is restricted to 2 orthogonal bases; the horizontal-vertical (H-V) basis or the 45° rotated basis (A-D). The properties of these linear polarizations are that a particular polarization has a 100% chance to propagate through a polarization filter aligned parallel with the polarization of the light and 0% chance to propagate through a polarization filter aligned in a direction orthogonal to the polarization of the light. The orientation of the polarizing filter may uniformly vary the transmission from 0% to 100% (Table 1). For instance, a photon with vertical polarization has the following transmission probabilities (Table 1) for a prescribed set of polarization filter orientations.

Table 1. Polarization transmission

Polarization Filter Orientation	Transmission Probability
H	0%
V	100%
$+45$	50%
-45	50%

This property of polarization is useful for quantum information purposes as a simple way to create and manipulate a qubit, where one polarization would (when measured) take the logical value of 0 and the other measurement a value of 1. However, unlike classical logical bits, a single qubit is simultaneously both 0 and 1 in superposition until measured. For instance, an equal superposition of 0 and 1 as a polarization qubit could be

$$|\Psi\rangle = \alpha |H\rangle + \beta |V\rangle \tag{5}$$

where $|H\rangle = 0$, $|V\rangle = 1$ and $\alpha = \beta = \frac{1}{\sqrt{2}}$.[14,15]

5.2.4 Measurement Processes and Bases Used in Quantum Protocols

This section discusses the measurement bases used in quantum protocols. Measurement bases for quantum communications protocols include linear polarizations $|\Psi\rangle = \alpha |H\rangle + \beta |V\rangle$, circular polarizations $|\Psi\rangle = \alpha |R\rangle + \beta |L\rangle$, orbital angular momentum $|\Psi\rangle = \alpha |L_0\rangle + \beta |L_1\rangle$ (L_n in this superposition indicate the Laguerre mode), and time-bin superpositions $|\Psi\rangle = \alpha |L\rangle + \beta |S\rangle$, where L and S refer to a superposition of long and short paths propagated by a quantum particle through an unbalanced Mach-Zehnder interferometer. Any quantum basis that has a measurable superposition with at least 2 possible results may be used in a quantum protocol.

There are several important aspects with regard to quantum measurement processes. The probabilities for measuring a quantum state can be given by

$$P(n) = \sum_n |c_n|^2 |\psi_n\rangle \langle\psi_n| \tag{6}$$

where the ψ_n correspond to the quantum states to be measured, such as the horizontal or vertical polarization of a photon, and the c_n are the wavefunction amplitudes for that quantum state. As an example, if one prepares a photon in a diagonal polarization ($\nearrow$) and then performs a measurement for horizontal or vertical in the perpendicular basis ($\perp$), the

17

c_n are equal to $\frac{1}{\sqrt{2}}$ and there is a 50% probability that the photon will be measured as either an H or a V photon. When measuring a composite quantum system made up of 2 states the Bell basis measurement is often used.[12,14] The 4 possible Bell basis states using polarization are

$$\psi^+ = \frac{1}{\sqrt{2}} \left(|H_A\rangle |V_B\rangle + |V_A\rangle |H_B\rangle \right) \tag{7}$$

$$\psi^- = \frac{1}{\sqrt{2}} \left(|H_A\rangle |V_B\rangle - |V_A\rangle |H_B\rangle \right)$$

$$\phi^+ = \frac{1}{\sqrt{2}} \left(|H_A\rangle |H_B\rangle + |V_A\rangle |V_B\rangle \right)$$

$$\phi^- = \frac{1}{\sqrt{2}} \left(|H_A\rangle |H_B\rangle - |V_A\rangle |V_B\rangle \right).$$

The following identities also hold for the Bell states:

$$|H_A\rangle |H_B\rangle = \frac{1}{\sqrt{2}} \left(|\phi^+\rangle + |\phi^-\rangle \right) \tag{8}$$

$$|H_A\rangle |V_B\rangle = \frac{1}{\sqrt{2}} \left(|\psi^+\rangle + |\psi^-\rangle \right)$$

$$|V_A\rangle |H_B\rangle = \frac{1}{\sqrt{2}} \left(|\psi^+\rangle - |\psi^-\rangle \right)$$

$$|V_A\rangle |V_B\rangle = \frac{1}{\sqrt{2}} \left(|\phi^+\rangle - |\phi^-\rangle \right).$$

A Bell measurement is a coincidence measurement that discriminates the actual state of an unknown 2-photon polarization system. A primary distinction between entangled states and non-entangled states is that an entangled state is not factorizeable into the product of 2 states:

$$\frac{1}{\sqrt{2}} \left(|H_A\rangle |V_B\rangle - |V_A\rangle |H_B\rangle \right) \neq \left(|H_A\rangle \pm |V_A\rangle \right) \otimes \left(|H_B\rangle \pm |V_B\rangle \right). \tag{9}$$

This non-factorizeability makes the entangled states quite powerful for quantum communications, quantum computing, and quantum imaging.[16,17] In this case, we are talking about photons that have polarization entangled states. The quality of a quantum measurement is often reported in terms of "fidelity". A quantum state is said to be "faithful" if the function $F(p,q) = \sqrt{pq}$ is sufficiently close to 1, where p indicates the probability that quantum state $|\Psi\rangle$ has been prepared and q is the probability that state $|\Phi\rangle$ was measured. This idea may also be reversed to say if state $|\Phi\rangle$ was measured then the "fidelity" of how well $|\Psi\rangle$ was prepared can be assessed.[14]

Another measurement technique is that of the positive operator valued measurement (POVM)

18

in distinction to projective measurements.[14,18,19] POVMs reduce the probability of inconclusive measurements with the use of ancilla modes. For instance, if photons that are polarized either horizontally (H) or $+45°$ in equal amounts are passed through a V polarizer or a $-45°$ polarizer, then if a photon passes through the V polarizer, it must have been a $+45°$ photon, and if the photon passes through the $-45°$ polarizer, it must have been a H polarized photon. This would yield a 25% chance to determine the polarization state of the transmitted photon. With the addition of certain "ancilla" modes of the optical fields a POVM can determine the polarization state of the transmitted photon, for this example, with a probability of 29.3%.[14]

5.2.5 Quantum Sources

All light is quantum all of the time but not all measurements and analyses readily reveal distinctly quantum properties of light. There are various ways to characterize sources of light in terms of their general properties such as incoherent radiation, coherent radiation, and non-classical sources of radiation. Incoherent sources of radiation are sources of light that are most familiar to us. Light bulbs, lamps, and solar light are all sources of incoherent thermal light. These incoherent light sources typically have broad spectral characteristics. We note that pseudo-thermal light[20,21] produced by the transmission of laser light through a scattering media such as a rotating ground glass plate has a much narrower spectral bandwidth than the more commonly experienced sources of thermal radiation. Coherent sources, such as lasers, are available in a variety of wavelengths and can be used for many quantum applications. Non-classical sources of light include entangled photons, produced by nonlinear processes such as spontaneous parametric down conversion (SPDC) and FWM, and squeezed light, where there is a trade-off between phase information and photon number information. To highlight the differences between coherent, thermal light, and non-classical light, Hanbury-Brown and Twiss (HBT) 2-photon interferometry is often used.[22–24] A HBT experiment is performed when light is split by a beam splitter toward 2 detectors. The detectors measure incident photons and the times that the measurements took place. The measurements at the 2 detectors are then correlated with each other, with results shown in Table 2.

Table 2. HBT experiment results

Light Source	HBT Result
Coherent (Laser)	No Correlation[23]
Incoherent (Thermal)	Positive Correlation (Peak)[16]
Non-Classical (Entangled)	Negative Correlation (Dip)[16]

19

The coincident deviations of the intensities from the mean of each detector tend to be positively correlated for incoherent light and negatively correlated (anti-correlated) for non-classical light.[16] The coincident deviations of the intensities for coherent light tend to be uncorrelated. Variations from standard experimental conditions may produce results that vary from these.

5.2.6 Quantum Coherence

Quantum coherence refers to a property associated with photons or other quantum particles. Quantum coherence represents an ideal quantum state where the uncertainty between conjugate variables are a minimum and are equally distributed.[22] For example, position x has an uncertainty of Δx and momentum p has an uncertainty Δp and the uncertainties are both a minimum and are equally distributed between Δx and Δp in the equation (e.g., when $\frac{\hbar}{2} = \Delta x \Delta p$). The closer a system is to this ideal uncertainty relationship, the more coherent it is said to be. For example a laser is often a very coherent system. Conversely, when the product $\Delta x \Delta p$ is much greater than $\frac{\hbar}{2}$ the system is said to be more incoherent. For example, thermal light sources such as the sun or an incandescent light bulb would radiate incoherent light. Pseudo-thermal sources created by propagating a laser beam through a rapidly rotating ground glass plate also can produce light that has incoherent properties.[20,21] Pseudo-thermal sources provide a convenient experimental source of partially coherent or incoherent radiation with relatively large coherence time and space scales. Coherence and incoherence can be best defined in the following manner. Similarly, light may be described as being spatially coherent if the coherence area of the light is larger than the largest aperture of an optical system.[15,22]

5.2.7 Quantum Decoherence and Quantum Memory

Quantum memories need to be able to preserve a quantum state long enough for operations to be performed on that quantum state. Quantum decoherence is the effect that occurs when quantum states interact with the environment and lose their quantum interference effects. Better quantum memories preserve a quantum state for a longer time.[25,26]

5.2.8 Energy-Time Entanglement

Energy-time entanglement and time-bin entanglement are closely related. Two particles can be energy-time entangled. Earlier we mentioned that photons can be polarization entangled. Quantum particles may be entangled in one or more properties. Energy-time entanglement has been achieved using an unpulsed pump laser and time-bin entanglement has been achieved using a pulsed laser.[27] Time-bin entanglement is a state where photons are entangled in between long and short paths of an unbalanced interferometer. That is, in quantum

systems, not only can quantum particles be entangled but also their paths can be entangled. Both path- and particle-based entanglement features can be exploited for developing quantum communications systems and networks.

5.2.9 Spontaneous Parametric Down conversion (SPDC) and Up Conversion

For quantum detection of correlated photons pairs at greater detection efficiencies, spontaneous parametric down conversion and up conversion methods have been developed.[16,28,29] Generally speaking, the SPDC process employs a χ^2 nonlinearity of a material such as beta-barium borate (BBO) or lithium borate (LBO) to split a pump photon into 2 photons subject to the condition

$$\nu_P = \nu_s + \nu_i \tag{10}$$

where ν_P is the frequency of the pump photon and ν_s and ν_i are the frequencies of the 2 down converted photons. The frequencies of ν_s and ν_i need not be equal to each other, which has useful applications for quantum communications. The subscripts s and i represent signal and idler, respectively. Historically, "signal" refers to the higher frequency anti-Stokes photon and "idler" is the lower frequency Stokes photon.[30] Similarly, up conversion uses a nonlinear process whereby a photon, say at the telecommunications wavelengths (1300–1500 nm) where detector efficiency is low and noisy, is up converted to the visible or near IR where silicon-based photon detectors have much higher efficiencies and less noise. In this case, the equation appears as

$$\nu_T + \nu_P = \nu_U \tag{11}$$

where ν_T is the frequency of the telecommunications wavelength photon and ν_U is the up converted detector photon. The frequency ν_P, the nonlinear media and the tuning of the phase-matching conditions must all be chosen to optimize the efficiency of the up conversion to ν_U for the particular detectors involved. We note that the relationship between the frequency ν and wavelength λ is given by the following:[13,31]

$$\nu = \frac{c}{\lambda} \text{ and } \lambda = \frac{c}{\nu}. \tag{12}$$

There is research to develop better entangled photon sources for free-space applications[32] where the wavefunctions for the polarization entangled photons generated by this implementation are of the form

$$|\Psi(\phi)\rangle = \frac{1}{\sqrt{2}}(|V_{\lambda_s}V_{\lambda_i}\rangle + e^{i\phi(\lambda_s,\lambda_i)}|H_{\lambda_s}H_{\lambda_i}\rangle) \tag{13}$$

21

where λ_s and λ_i are the wavelengths of the downconverted photons and ϕ is a relative phase between the 2 wavelengths in their device. In practice, the phase ϕ must be considered; however, it is often left out of theory formalism to simplify the presentation.

5.3   Teleportation Implementation

Entanglement is a quantum mechanical phenomenon in which the interacting states of 2 or more quantum systems cannot be described independently. Teleportation uses entanglement and is a quantum process whereby quantum information can be transmitted over long distances.[33,34] As an example of the process of quantum teleportation, assume that Alice and Bob share half of an entangled photon pair that is in the state $|\Psi\rangle_{AB} = \frac{1}{\sqrt{2}} (|H_A\rangle |V_B\rangle - |V_A\rangle |H_B\rangle)$ and that Alice wants teleport to Bob a photon with a defined polarization $|\Omega_C\rangle = \frac{1}{\sqrt{\alpha^2+\beta^2}} [\alpha |H_C\rangle + \beta |V_C\rangle]$. Alice would perform a joint Bell measurement on her half of the entangled photon pair with the photon she wants to teleport. Prior to the joint-measurement, the state of the 3 photons is $|\Psi\rangle_{AB} \otimes |\Omega_C\rangle = \frac{1}{\sqrt{2}} (|H_A\rangle |V_B\rangle - |V_A\rangle |H_B\rangle) \otimes \frac{1}{\sqrt{\alpha^2+\beta^2}} (\alpha |H_C\rangle + \beta |V_C\rangle)$. The physics of teleportation describes how the photons of Alice and Bob's entangled pair and the photon to be teleported are changed in Alice's basis to appear as if Alice's photon $|\Psi\rangle_A$ is in an entangled state with $|\Omega_C\rangle$. Using Eqs. 7 and 8, the 3-photon state

$$\frac{1}{\sqrt{2(\alpha^2+\beta^2)}} \{ \alpha (|H_A\rangle |V_B\rangle |H_C\rangle - |V_A\rangle |H_B\rangle |H_C\rangle) \tag{14}$$
$$+ \beta (|H_A\rangle |V_B\rangle |V_C\rangle - |V_A\rangle |H_B\rangle |V_C\rangle) \}$$

can be rewritten as

$$\frac{1}{2} \frac{1}{\sqrt{\alpha^2+\beta^2}} \{ |\phi^+\rangle_{AC} \otimes (\alpha |V_B\rangle - \beta |H_B\rangle) + |\phi^-\rangle_{AC} \otimes (\alpha |V_B\rangle + \beta |H_B\rangle) \tag{15}$$
$$+ |\psi^+\rangle_{AC} \otimes (-\alpha |H_B\rangle + \beta |V_B\rangle) + |\psi^-\rangle_{AC} \otimes (\alpha |H_B\rangle + \beta |V_B\rangle) \}.$$

Alice has 4 possible outcomes for her joint measurement of the state $|\Psi\rangle_{AC}$

$$\left|\Psi^1\right\rangle = \frac{1}{\sqrt{2}}\left(|H_A\rangle\,|V_c\rangle - |V_A\rangle\,|H_c\rangle\right) \tag{16}$$

$$\left|\Psi^2\right\rangle = \frac{1}{\sqrt{2}}\left(|H_A\rangle\,|V_c\rangle + |V_A\rangle\,|H_c\rangle\right)$$

$$\left|\Psi^3\right\rangle = \frac{1}{\sqrt{2}}\left(|H_A\rangle\,|H_c\rangle - |V_A\rangle\,|V_c\rangle\right)$$

$$\left|\Psi^4\right\rangle = \frac{1}{\sqrt{2}}\left(|H_A\rangle\,|H_c\rangle + |V_A\rangle\,|V_c\rangle\right)$$

and she would transmit 2 bits to Bob that would instruct him on what transform T to use to operate on his remaining photon of the entangled pair to complete the teleportation. The 4 cases and operations are 1) $T_1 = \begin{bmatrix} 1 & 0 \\ 0 & 1 \end{bmatrix}$, 2) $T_2 = \begin{bmatrix} 1 & 0 \\ 0 & -1 \end{bmatrix}$, 3) $T_3 = \begin{bmatrix} 0 & 1 \\ 1 & 0 \end{bmatrix}$, and 4) $T_4 = \begin{bmatrix} 0 & -1 \\ 1 & 0 \end{bmatrix}$. Case 1 is the identity operation and indicates that Bob's photon is in the state of the photon that Alice teleported to him. Case 2 applies a π phase shift to the $|V\rangle$ component of Bob's photon to complete the teleportation. Case 3 rotates the polarizations from $\alpha\,|H_B\rangle + \beta\,|V_B\rangle$ to $\alpha\,|V_B\rangle + \beta\,|H_B\rangle$ and Case 4 performs an operation similar to Case 3 with a π phase applied shift to the $|H\rangle$ component of Bob's photon.

5.4   Entanglement and Teleportation Experiments

This section describes experimental approaches, setups, and results of initial photonic teleportation experiments at ARL. The feasibility of performing entanglement and teleportation experiments between ARL and JQI either one way or round trip were investigated. Figures 6 and 7 are depictions of the QNET-AP entangled photon paths involving ARL to JQI roundtrip, ARL to JQI one way, and a distributed network with atom chips and entangled photons. In the sections that follow, we present features of the ARL entanglement source and results from our preliminary entangled photon transmission characterization of the ARL to JQI fiber link (Fig. 8). To examine photonic teleportation capabilities, an initial experiment for probabilistic teleportation was designed and implemented. The details of the photonic teleportation experiments (Fig. 9) are given in Section 5.4.7. In Section 5.4.9, we experimentally explored the capability of entanglement swapping to entangle photons from entangled pairs created in 2 different time bins. Results from these experiments were characterized using the quantum density matrix of the 2-photon state. We also present in Section 5.4.10

a concise description of our designed and patented system and method protocol to compress and probabilistically optimize information transfer during quantum communication by means of teleportation. Finally, we summarize the results and achievements attained from the ARL entanglement and teleportation experiments.
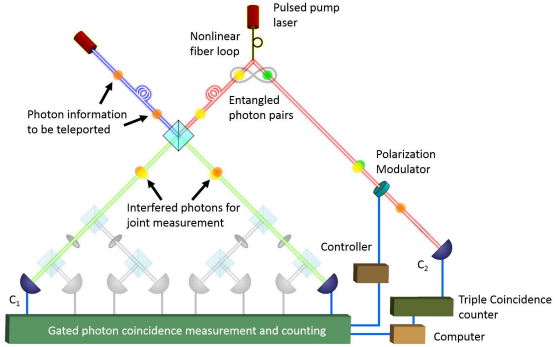
Fig. 9 Setup of teleportation experiments

5.4.1   Entangled Photon Transmission Over the Fiber Setups in CISD

It is important to characterize the effects of entanglement propagation over long distances through the ambient environment. To investigate the transmission of entangled photons from ARL to nearby institutions, such as depicted in Fig. 7, we designed a setup that allowed us to perform entangled photon experiments with the round trip paths between ARL and JQI. The decoherence of entangled photons in fiber has been documented in important studies that include the sudden death of entanglement,[35] non-local compensation of polarization mode dispersion (PMD),[36] and loss of entanglement.[37] These experiments were performed in fibers on spools housed within a laboratory. We characterized the ability of the fiber connection between ARL to JQI and return (Fig. 8) to transmit entangled photons. The fiber link between ARL and JQI is subject to environmental effects that cannot be reproduced in the laboratory. To test the entangled photon round trip transmission from ARL to JQI and back over installed dark optical fiber, we coupled our entangled photons into and out of the fiber loop with wave division multiplexers, as shown in Fig. 10. Entangled photons were transmitted through the fiber 27-km round trip from ARL to JQI and we measured surviving entangled photons within our time windows. To get a baseline, these initial tests used a local timing clock provided by the entangled photon source to gate the detectors. For this initial set of experiments, we measured 70 entangled photon pairs per second. The time of propagation of the entangled photon pairs through the optical path showed a fluctuating ± 250 ps offset with respect to the local clock. If timing offsets are sufficiently large, they will

24
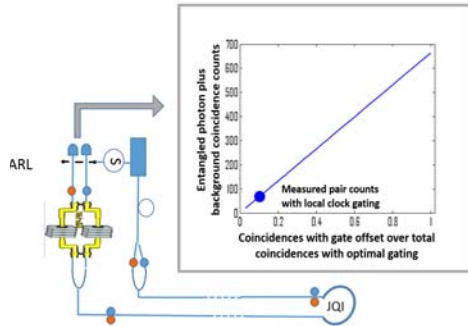
Fig. 10 Experimental setup to determine long-distance entangled photon transmission baseline using a local clock for gating detectors. The setup includes 2 wave division multiplexers (WDMs) to couple the entangled photons into and out of a single optical fiber.

reduce signatures of constructive (destructive) quantum interference from entangled photons; however, calculations can be made of what the effect would be if the timing offsets (timing jitter) were reduced.[47] The long path to JQI and return added timing offsets to our setup. In summary, based on the results of these experiments we developed an improved design,
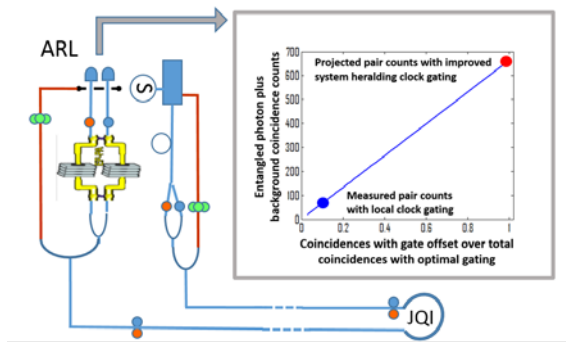
Fig. 11 Planned experimental setup for efficient long distance entangled photon transmission using an optical timing pulse to gate detectors. The setup includes 2 WDMs to couple the entangled photons into and out of a single optical fiber. Two additional WDM components are included that couple an optical clock pulse, shown by the green circles and orange lines, that travel with the entangled photons and be subject to the same phase timing disturbances. Projected photon pair counts would increase to more than 600 pairs per second.

illustrated in Fig. 11, that would couple in an optical timing pulse to the entangled photon path where we would expect a reduction in the timing offsets that had been due to the path propagation variability with respect to the local clock. We anticipate that this could yield an increase from 70 pairs per second to more than 600 pair counts per second; nearly a factor of 10 improvement in coincidence counts. Furthermore, it is important to mention that polarization entangled photons are less affected by fiber-optic phase variations than single photon polarizations because the entangled photon pair polarizations are not set until

25

measured after transiting the fiber. This provides a key benefit for implementing entangled photons in quantum communication schemes that can exploit this feature.

5.4.2   Entanglement Experiments

We also performed measurements on our entangled photon source and established the non-classical character of the entangled photons using 2-photon interference visibility tests (Figs. 13 and 15). The setup for these experiments is shown in Fig. 12. In these experiments an
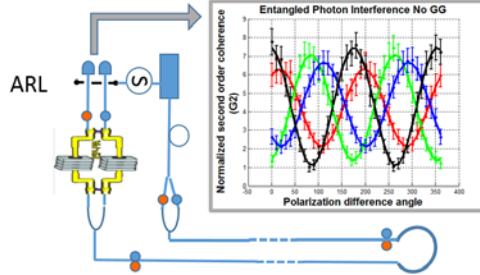
Fig. 12   Setup to measure polarization entangled photon 2-photon interference visibility. An entangled photon source generates pairs of polarization entangled photons. Each photon is directed to pass through a polarization analyzer prior to being measured.

entangled photon source generates pairs of polarization entangled photons. Each photon of the entangled pairs is directed to pass through a polarization analyzer prior to being measured. One polarizer is set to a fixed polarization angle θ_1 and the second polarizer angle θ_2 is rotated through 360°. The results are shown in terms of $\Delta\theta$, which is the difference between the 2 polarizer angle settings.
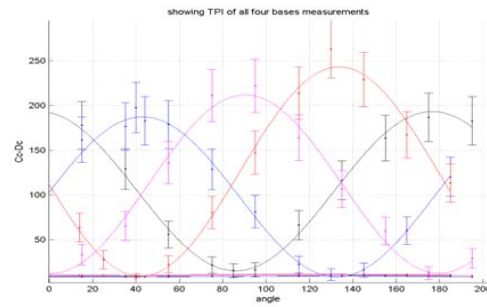
Fig. 13   Two-photon polarization interference coincidence measurements in 4 measurement basis

5.4.3   Measures of Non-Classicality and Entanglement

Entanglement is a quantum mechanical phenomenon in which the interacting states of 2 or more quantum systems cannot be described independently. Also, photons as part of a quan-

26

tum mechanical system may be characterized as to whether they obey predominantly classical statistics or non-classical statistics. Entangled photons are distinctly non-classical, but there are also other non-classical states. Properties of non-classicality may include, but are not limited to, non-locality, superposition, indistinguishability, and interference in space and time. Quantum mechanical systems obey rules that are described by probability amplitudes or wavefunctions. There are various tests for entanglement and non-classicality of photon systems. Violation of Bell inequalities, Hong-Ou-Mandel (HOM) visibility tests, fidelity measures, n^{th}-order interference experiments, and other approaches are used to help characterize entanglement and are used as entanglement witnesses.[49] The violation of Bell's inequality has been considered an important marker for entanglement,[51] nevertheless research to improve the methodology is still active.[55] The Clauser-Horne-Shimony-Holt (CHSH)[52] test was developed to characterize non-classicality and entanglement. The CHSH parameter "S" is calculated from measured quantum data. A value of S greater than 2 under the right conditions indicates a violation of Bell's inequality as an indicator of entanglement, non-locality, and non-classicality. The normalized second-order coherence function, $G^{(2)} = G^{(2)}\left(t_1, x_1; t_2, x_2\right)$, provides a measure of entanglement for polarization entangled photons.[47] Although it may be described in other ways, it is important to realize that the HOM interference is, in fact, between quantum probability amplitudes and not between photons.[50] Thus in our analysis we work with quantum probability amplitudes.

5.4.4 Entanglement Propagation Through Scattering and Decohering Media
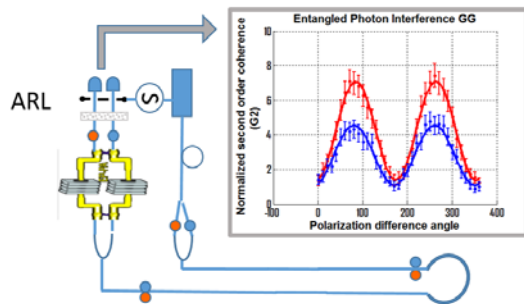
Fig. 14 Setup to measure polarization entangled 2-photon interference visibility after propagating through scattering and absorbing media. An entangled photon source generates pairs of polarization entangled pho-tons. Each photon is directed to pass through a polarization analyzer prior to being measured. Prior to being measured, each or both photons of the entangled pairs may pass though scattering and absorbing media (i.e., ground glass).

The photons in an installed fiber network undergo decoherence due to a number of factors including network conections and changing environmental conditions. In order to gain better understanding of the effects of scattering on entanglement decoherence laboratory tests were conducted that measured the propagation of entangled photons through scattering and

27

decohering media. The entangled photon pairs were generated and one or both of the photon pairs were propagated through a piece of ground glass prior to passing through a polarization analyzer and being measured. The setup for these experiments is shown in Fig. 14. The primary distinction between the setup described in Fig. 12 is the inclusion of a ground glass plate shown in Fig. 14 in one or both of the entangled photon propagation paths to simulate a scattering and absorbing media. We characterized the effect of propagation of entangled
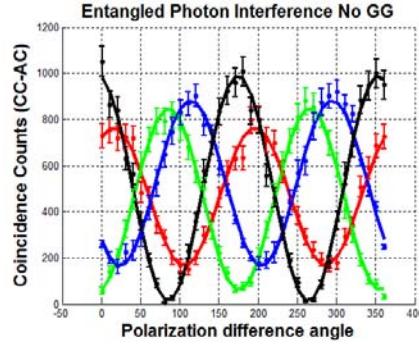
Fig. 15 Entangled photon CC measured for experiments without a ground glass in the path of entangled photon propagation

photons through ground glass and found a reduction in entangled photon visibility due to the ground glass. Figure 15 presents the results of entangled photon polarization visibility coincidence counts (CC) measured without propagating through ground glass. Figure 16 presents the results of entangled photon polarization visibility coincidence counts measured when the entangled photons propagated through ground glass prior to measurement. Comparing Figs. 15 and 16, one can see that while there was a significant decrease in coincidence measurements, the character of the entanglement was retained with propagation through ground glass.
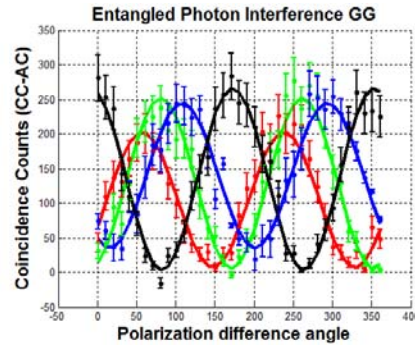
Fig. 16 Entangled photon CC measured for experiments with a ground glass in the path of entangled photon propagation

28

A second metric for visibility and non-classicality is the second-order coherence of 2 photons (i.e., the Glauber $G^{(2)}$ function).[22] $G^{(2)}$ is typically represented by

$$G^{(2)} = \frac{\langle CC_{1,2} \rangle}{\langle C_1 \rangle \langle C_2 \rangle} \tag{17}$$

where the $CC_{1,2}$ are the coincidence counts measured between detectors 1 and 2 and the $C_i, i = 1, 2$ are the single photons measured by detectors 1 and 2.[57] The angled brackets $\langle \rangle$ indicate an ensemble average such that $\langle CC_{1,2} \rangle$ is the expected value, or probability of measuring a coincidence between detectors 1 and 2 and $\langle C_i \rangle$ are the probabilities of detectors 1 and 2 to make a single photon detection. A violation of the Cauchy-Schwartz inequality
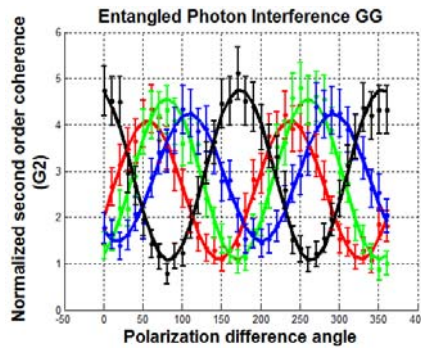
Fig. 17 Entangled photon $G^{(2)}$ as a function of polarizer setting for experiments with ground glass

regarding the second-order coherence function for indistinguishable bosons is an indicator of the quantum properties of nonclassicality and entanglement of the particles.[53] Figures 17 and 18 show the values of $G^{(2)}$ as a function of the difference in angle of the polarization analyzers. One can see that in Fig. 17, where the entangled photons propagated through ground glass, that $G^{(2)}$ ranged from 1 to ~5, which shows that the ground glass did not completely destroy the nonclassical nature of the entangled photons. In contrast for the experiments performed without ground glass, as shown in Fig. 18, the value of $G^{(2)}$ ranged from 1 to nearly 8.

To emphasize the comparison of ground glass deterioration, Fig. 19 compares the $G^{(2)}$ results of a no-ground glass experiment in red and the $G^{(2)}$ results using the same polarization settings with ground glass in blue. There is about a factor of 2 decrease in the peak $G^{(2)}$ values while the low values for both cases are approximately 1. This is due to the fact that $G^{(2)}$ is dependent on the number of coincidence measurements and when, for our entangled photon source, the difference between the polarizers is ~90°, the coincidence rate drops nearly to 0. Similarly, Fig. 20 also presents $G^{(2)}$ curves for ground-glass and no-ground-glass

29
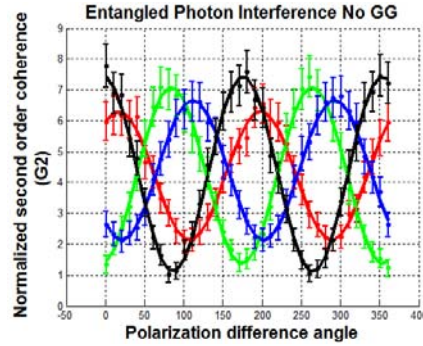
Fig. 18 Entangled photon $G^{(2)}$ as a function of polarizer setting for experiments without ground glass
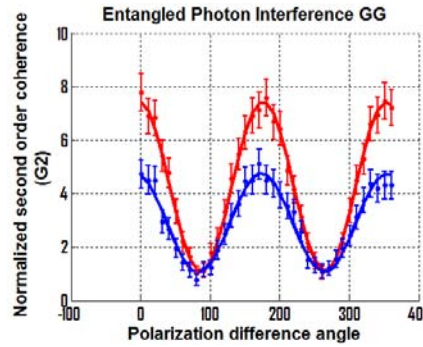
Fig. 19   Comparison of entangled photon $G^{(2)}$ as a function of polarizer setting for experiments with and without ground glass

experiments at a different polarization analyzer setting such that peaks of coincidence are at settings of $\sim$90° difference. The results from these experiments show that while there is a decrease in the visibility of the 2-photon interference the properties of entanglement can survive propagation through scattering and decohering media. This feature of entanglement may prove useful for Army applications in challenging environments.

5.4.5   Entangled Photon Tests by Bell Inequality Violations

To understand the effects of decoherence on the propagation of entangled photons through scattering and decohering media, Bell inequality violation tests were conducted with transmission through ground glass. Entangled photons going through fibers will decohere as a function of such factors as index of refraction changes, scattering, absorption, and imperfections. Because of its scattering and decohering effects, ground glass serves as a severe test of entangled photon survivability compared to the effects of fiber on transmission. Entangled photons were propagated through ground glass as shown in the setup of Fig. 14. Results of the entangled photon tests to measure the violation of Bell inequalities are shown in the following figures. Accidental coincidence counts can be subtracted from the total measured

30
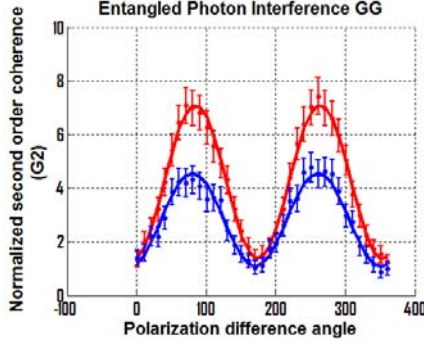
Fig. 20 Comparison of entangled photon $G^{(2)}$ as a function of polarizer setting for experiments with and without ground glass

coincidence counts to obtain corrected coincidence counts according to procedures analogous to those of Shadbolt et al.[55]
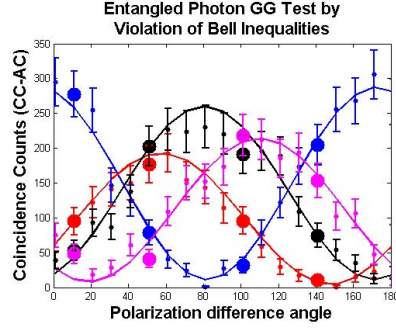
Fig. 21 Bell inequality violation S-parameter equal to 2.1928 (accidentals subtracted)

Figure 21 shows the measured joint detections as a function of polarization difference angles. The difference angles refer to the setting of the polarization analyzer in Fig. 14. The larger dots indicate the locations in the measurement interference curve which were used in the violation of Bell inequalities test. The Bell inequality violation parameter for the indicated measurement locations yielded a value of S=2.2067. An S value greater than 2 indicates the presence of entanglement.[52] Data from many trials can be combined in a manner consistent with the CHSH Bell inequality tests to achieve better statistical confidence. Probabilities of joint detections were determined from a series of measurements in 4 different bases as a function of the polarizer settings in the polarization analyzers. CC measurements were made with the correlated photon detection system (CPDS) as the entangled photons exited the polarization analyzers. Typically 100M gated measurements were made at each point in each of the 4 bases. Figure 22 shows a second set of locations selected from the measurement interference curves that sampled alternative coincidence count measurements. The lines show

31
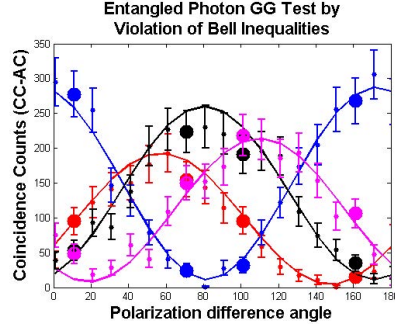
Fig. 22 Bell inequality violation S-parameter equal to 2.0216 (accidentals subtracted)

the measured joint detections as a function of polarization difference angles and the large dots indicate the locations in the measurement interference curve that were used in the violation of Bell inequalities test. The Bell inequality parameter for this second set of measurements of entangled photon transmission through ground glass was S=2.0216.

Experiments were also conducted without the ground glass decohering media using the setup shown in Fig. 12. Illustrative sample results of our Bell inequality violation tests are shown
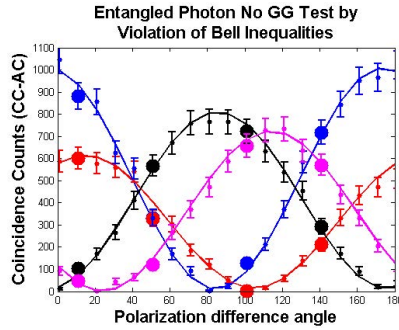
Fig. 23 Bell inequality violation S-parameter equal to 2.4037 (accidentals subtracted)

in Figs. 23 and 24. Figure 23 shows the measured joint detections as a function of polarization difference angles for an experiment without entangled photon transmission through ground glass. The large dots indicate the locations in the measurement interference curve that were used in the violation of Bell inequalities test. These locations are the same as those used in Fig. 21. The Bell inequality violation was 2.4037, which is larger than the corresponding ground glass test. In Fig. 24 the measured joint detections are indicated by lines and the large dots indicate the locations that are the same locations used in Fig. 22 to analyze the Bell inequality. The S-parameter for this case without transmission through ground glass was S=2.1894.

32
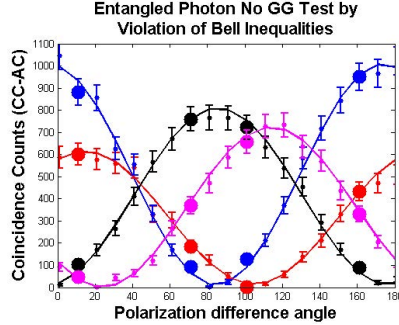
Fig. 24 Bell inequality violation S-parameter equal to 2.1894 (accidentals subtracted)

In summary, Bell inequality violation parameters were found to be S=2.1928 and S=2.0216 for entangled photon transmission through ground glass and S=2.1894 and S=2.4037 for entangled photon transmission in the experimental setup without the ground glass. On average, we found that ground glass decreased the entanglement Bell inequality violation and reduced the number of entangled pairs measured, but sufficient entanglement likely remained to be useful for quantum communications teleportation experiments involving photons over an ARL to JQI type network. Most of the entangled pairs were not severely affected by the phase aberrations of the ground glass. Based on our results, it is recommended that a similar experiment be conducted for propagation of entangled photons from ARL to JQI and the return using the experimental setup illustrated in Fig. 11 where the long distance fiber-optic network takes the place of the ground glass as the scattering and decohering media.

5.4.6 Timing for Teleportation: Measurements of Entangled Photon Jitter

Accurate timing for coincidences and interference is vital for the operation of a quantum network. To understand some of the timing issues related to the generation of entangled photons we performed experiments to determine the time distribution of entangled photon coincidence measurements. These experiments used the setup shown in Fig. 25. The time difference is between the start of a clock cycle, which is related to the pump pulse laser that generates the entangled photons, and the next coincidence measurement. Results of these experiments for the time distribution of entangled photon coincidence measurements are presented in Fig. 26.

These results indicate that a clock which is more tightly coupled to the entangled photon pair may be useful to improve performance of quantum communications across a quantum network.

For some memory entanglement schemes, the polarization properties of transmitted photons

33
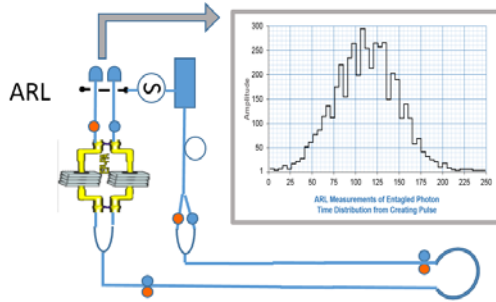
Fig. 25 Setup to measure entangled photon time distribution. The time distribution is characterized by the time difference between the start of a clock cycle, which is related to the pump pulse laser that generates the entangled photons, and the next coincidence measurement.
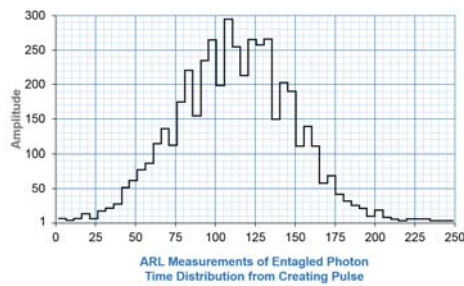
Fig. 26 Entangled photon time distribution from creating pulse

are used. We characterized the stability of the polarized light transmission with regard to the fiber environment. The results of these studies are in Section 8 entitled "Environmental Effects on Polarized Light Fiber Distribution".

We also investigated alternate scientific schemes for establishing a distributed hybrid quantum communications network with entangled photons and atom/ions. To test the potential for quantum communications using entangled photons, we made measurements of probabilistic teleportation.[38,39] Probabilistic teleportation has an advantage in some cases. For one scheme, when the teleportation fails, the sender can recover the unknown state and the process can be repeated until the state is actually teleported.[39]

5.4.7   Laboratory Teleportation Experiments

To examine the potential for long-distance teleportation of information across an installed fiber optical network we performed probabilistic teleportation[39] experiments using setups similar to those shown in Figs. 9 and 27. In the following, we discuss procedures, entanglement source, background, and analysis for some of the initial photonic teleportation experiments.

The characterization of quantum states by measurements was explored by Glauber[22,67] who

34
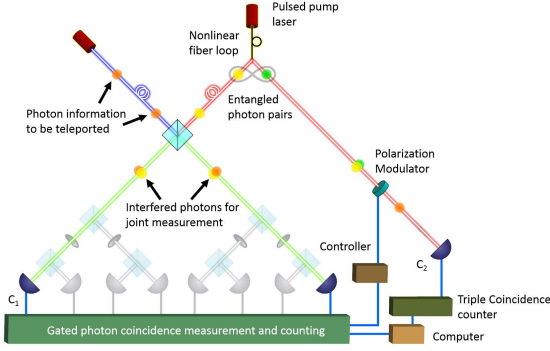
Fig. 27 The entangled photon source uses FWM in a nonlinear fiber loop to generate pairs of entangled photons. The residual pump is polarized and inputs information source photons. One of the entangled photons passes through an optical delay line to ensure wavefunction overlap on a 50/50 beamsplitter with the attenuated residual pump pulse. The photon coincidence measurement component (PCMC) is used to detect coincident measurements between the 2 detectors. An electronic delay is used to compensate for the timing differences. The remaining photon of the entangled photon pair passes through a polarization analyzer and is then measured. The detector output is input into a triple coincidence counter along with the electronically delayed output from the PCMC to detect triple coincidences.

introduced n^{th}-order coherence functions to describe joint measurements with n detectors. The relation of normalized Glauber functions to a Cauchy-Schwarz inequality and other violations provides a metric of the non-classicality (quantumness) of measured states. The second-order Glauber correlation is written as

$$G_{i,j}^{(2)} = \left\langle \hat{a}_i^\dagger \hat{a}_j^\dagger \hat{a}_j \hat{a}_i \right\rangle = \langle : \widehat{n}_i \widehat{n}_j : \rangle$$

where the i, j indicate the detector, $\hat{a}$ and $\hat{a}^\dagger$ are the annihilation and creation operators, $\hat{a}_i^\dagger \hat{a}_i = \widehat{n}_i$ is the photon number operator, and $\langle : : \rangle$ describes the expected value with normal ordering of the operators.[65] Generally the nth-order Glauber correlation $G_{i,...,N}^{(n)}$ is written as

$$G_{i,...,N}^{(n)} = \left\langle \hat{a}_1^\dagger \hat{a}_2^\dagger ... \hat{a}_N^\dagger \hat{a}_N ... \hat{a}_2 \hat{a}_1 \right\rangle = \langle : \widehat{n}_1 \widehat{n}_2 ... \widehat{n}_{N-1} \widehat{n}_N : \rangle$$

where N is the maximum number of detectors. The third-order Glauber correlation was used to describe the 3-fold coincidences from the teleportation experiments where

$$G_{i,j,k}^{(3)} = \left\langle \hat{a}_i^\dagger \hat{a}_j^\dagger \hat{a}_k^\dagger \hat{a}_k \hat{a}_j \hat{a}_i \right\rangle = \langle : \widehat{n}_i \widehat{n}_j \widehat{n}_k : \rangle .$$

Various methods to test for non-classsicality and entanglement have been proposed and studied.[68] Many of these tests are examining the phenomena for a violation of a Cauchy-Schwarz inequality.

35

Teleportation is closely tied to 3-photon states and can be indicated by 3-fold photon coincidence measurements. The first experimental demonstration of teleportation used 3-fold coincidences to determine if the polarization of the information photon had been teleported to the polarization of the remaining photon of the initial entangled pair.[34] Three-fold coincidences and normalized 3-fold coincidences can also be used to characterize other third-order quantum effects. Peaks in 3-fold coincidences and normalized 3-fold coincidences have been reported for experiments on teleportation, quantum relays, and 3-photon sources.[71–74]

Most teleportation experiments are performed under steady conditions. In the following we analyze teleportation under non-steady conditions where the mean photon and coincidence photon fluxes are changing during the experiment. The idea is to test whether 3-fold correlation normalization by the coincidence measurements is indicative, under unsteady conditions, of 3-photon measurement overlap verifying teleportation. The results for these experiments are promising in that they are able to pick up the timing of the nearly optimal teleportation overlap. Further experiments are needed under different conditions to see if the scaling is robust under more general conditions.

5.7.4.1 Analysis of Sample Teleportation Data: Experiment Series 1

While teleportation can be achieved in a photonic system without a quantum memory, repeaters with quantum memories are necessary for robust long-distance teleportation in a quantum network. Nevertheless, teleportation experiments without quantum memory can provide crucial information on the physics timing, scaling, and protocols while practical quantum memories are in development. Though with limitations, even all photonic quantum repeaters have been proposed.[40] Recent proof-of-principle teleportation experiments provide insight into the behavior of multi-photon states in fiber optics networks. Entangled photons for the ARL experiments were generated using a custom made commercial entangled photon source and detectors. The entangled photon source generated entangled photon pairs in a ϕ^+ state given by the superposition

$$\phi^+ = |HH\rangle + e^{i\varphi} |VV\rangle. \tag{18}$$

The information photon emanated from an attenuated channel of the residual pump of the entangled photon source. The information photon is then set to a known polarization state, e.g., $|H\rangle$ or $|V\rangle$. The information photon interacts on a 50/50 beamsplitter with one photon of an entangled pair from the entangled photon source with 4 possible outcomes. After the interaction, the photon paths are directed to photon detectors and are measured. The

photon measurements are then input into a PCMC to determine if the measurements are coincident. Calibration of the interaction of the information photon and one photon of an entangled pair of photons was determined by measuring the coincidence rate of the entangled photon-information photon joint measurement as a function of optically delaying the information photon entering the 50/50 beamsplitter. Good overlap of the information photon wavefunction with the wavefunction of an entangled photon is indicated when this coincidence rate was at a maximum value. A low coincidence rate is indicative of a poor overlap of the wavefunctions which further signifies that the information photon is not interacting efficiently with an entangled photon.

After calibration, a series of longer duration (300 s) measurements were performed to test the teleportation of the information photon state. On registering a coincidence between the information photon and one photon of an entangled photon pair, the PCMC outputs an electronic signal that is input to a triple coincidence counter after passing through an adjustable electronic delay. The electronic delay is used synchronize the measurements of the first pair of photons and the measurement of the remaining photon. The measurement of a coincidence is indicative that the state of the 2-photon sub-system is ψ^-. This occurs when the 2 photons have orthogonal polarizations. Because the state of the information photon is known, then at measurement the polarization of the entangled photon must be orthogonal to the information photon. Since the entangled photons began in a ϕ^+ state and a coincident measurement was recorded, the remaining photon must also be orthogonal to the information photon. The remaining photon of the entangled photon pair then passes through a polarizer and is measured. For example, in this case, the polarizer may be set orthogonal to the polarization of the information photon to allow passage and detection of the teleported photon. The photon measurement is input into a 3-fold coincidence counter along with the output of the PCMC to determine if a 3-fold coincidence has occurred. The coincidence window for each coincidence measurement can be varied.

In the following, we examine 3-fold photon coincidences scaled by 2-fold coincidences. Three-fold coincidences that are scaled by 2-fold coincidences from our teleportation experiments at ARL are shown in Fig. 28. They are analogous to Glauber representations but differ in the normalization. The experimental results indicate that teleportation was achieved using a pulsed fiber-optic based system in the telecom wavelength range generating signal and idler polarization entangled photons with different but nearby wavelengths. The red line in Fig. 28 shows the scaled teleportation indicator, $F(\tau) = \int G^{(3)} dt$, as a function of 3-fold timing overlap adjustment. Varying the timing delay allows monitoring of the arrival time of the teleported photons to characterize the teleportation detection profile. The normalized triple
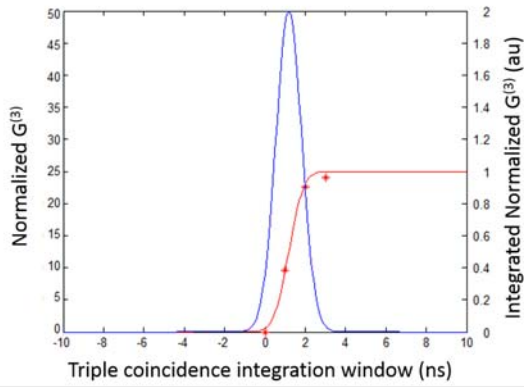
Fig. 28 Examples of experimental teleportation data: Solid red line shows the scaled teleportation indicator; $F(\tau) = \int G^{(3)} dt$ indicating relative teleportation efficiency as a function of delay overlap. The maximum of $F(\tau)$ was set to 1 in the fit to indicate estimated relative efficiency. The variables g_{123} indicates 3-fold coincidences and g_{12}, g_{23}, g_{13} indicate 2-fold coincidences where the numbers identify the detectors. Solid Blue: Normalized above background $G^{(3)}$ distribution calculated from fitted error function.

correlation $G^{(3)} = \frac{g_{123}}{\sqrt{g_{12}*g_{23}*g_{13}}}$ was used to scale the measurements and normalize g_{123}. The term g_{123} indicates 3-fold coincidences and g_{12}, g_{23}, g_{13} indicate 2-fold coincidences where the subscript numbers identify the detectors. We are exploring $G^{(3)}$ as a measure of the quantum non-classicality of a 3-photon state since it ratios measured 3-fold coincidences to a measure of background 2-fold coincidences that may produce accidental 3-fold coincidences. $G^{(3)}$ is a useful measure of teleportation because teleportation occurs when a 3-photon superposition state exists prior to the measurement of photons in the send side and the receive side of the teleportation system. Other normalizations have been explored such as the anti-correlation parameter, $\alpha = \frac{g_1 g_{123}}{g_{12} g_{13}}$.[58,70,75,76] We explored this version of $G^{(3)}$ to investigate its properties since it does not require single photon counts though it does require coincidences between all pairs of the 2-fold coincidences. We found that normalizing triple coincidences by 2-fold coincidences could be used as a stable indicator of teleportation. Nevertheless, we have used and compared various measures of non-classicality including the anti-correlation parameter α.

The probability distribution of normalized 3-fold coincidences above background was modeled as Gaussian distribution where the distribution is a function of the delay between the sender coincidence measurement (CC_{send}) and the measurement of the remaining entangled photon D_{rp}. The coincidence window is moved over the Gaussian distribution as a function of the delay time, which results in a Gaussian error function shape. The data were fit to a Gaussian error function and are displayed as the red line in Fig. 28. The experiment sampled the distribution within a 6-ns coincidence window by electronic adjustment of the

38

CC_{send}, D_{rp} delay. The blue line in Fig. 28 presents a plot of the normalized 3-fold coincidence distribution and indicates where the coincidence window sampled the distribution. The hardware for the programmable electronic delay between the CC_{send} measurements and D_{rp} measurements had a minimum delay of approximately 5 ns. The reported delays are additional programmable delays added to the minimum to place sender coincidence detection events inside a coincidence window with the detection of the remaining entangled photon. The effect of changing the delay was to alter where the normalized 3-fold coincidence distribution was sampled. If a longer optical path of 3 to 4 m were included on the remaining entangled photon for this experimental setup we would expect to be able to more accurately sample the 3-fold coincidence distribution and increase the 3-fold coincidence and normalized 3-fold coincidence values. These results for this experiment is promising in that it was able to pick up the timing of the nearly optimal teleportation overlap. The theory has been developed further to relate to nonclassicality parameters. More details of the theory and analysis will be published in a forthcoming paper.[77]

Measurements used to plot the results shown in Fig. 28 are presented in Table 3, where the coincidences were counted for 300 s at delay settings between 2 and 5 ns. In the following sample of teleportation data, the coincidence window was set to 6 ns. The registration of triple coincidences above background indicates teleportation of the information photon states. Note that the greatest number of triple coincidences occurred at a 3-ns delay with 24 3-fold coincidences per 300 s and this dropped to 13 3-fold coincidences with a delay at 5 ns and 18 3-fold coincidences at a 2-ns delay. To compensate for the varying coincidences rate, it is advantageous to apply an appropriate normalization.

Table 3. Sample of data from triple coincidence measurements

$Delay$	$Coincidences$	$Triples$	$G^{(3)}$	$G^{(3)}\ background subtracted$	$Normalized\ x100$
2 ns	3096	18	$1.04E-4$	$4.165E-5$	98.49
3 ns	3804	24	$1.02E-4$	$3.946E-5$	97.69
4 ns	4312	23	$0.812E-4$	$1.839E-5$	38.2
5 ns	3498	13	$0.628E-4$	0	0

Table 3 lists the number of 2-fold and 3-fold photon coincidences as a function of delay time between the measurement of the joint measurement of the information photon and one photon of an entangled photon pair and the measurement of the remaining photon of the entangled photon pair. At the 5-ns delay time a background of 13 3-fold coincidences

39

was measured and after scaling was considered background for all delay settings. The non-zero triple coincidence measurements level is consistent with the noise background of the detectors that measure photons in the telecom wavelengths. Thus for this experiment, we estimate that the input photon state was teleported approximately 11 times in 300 s over a distance of approximately 2 m in the laboratory. As a follow on, we have been engaged in experiments extending the teleportation capability with higher precision timing, resulting in higher teleportation rates, and these results will be reported separately.

5.7.4.2 Analysis of Sample Teleportation Data: Experiment Series 2

A second series of teleportation experiments were conducted to analyze configuration and timing constraints using improved detectors in a custom modified system. In the following, we discuss the scaling of 3-fold coincidence measurements shown in Fig. 29 from the laboratory teleportation setup. Figure 29 shows $G^{(3)} = \frac{g_{abc}}{\sqrt{g_{ab} * g_{bc} * g_{ac}}}$ as a function of $\sqrt{g_{ab} * g_{bc} * g_{ac}}$. Three-fold coincidences were measured between 2 detectors on the "send" side and each of the detectors on the receive side. To gain insight on the effect of polarization and elapsed time on the overall distribution of the scaled teleportation the normalized results are shown in Fig. 29. It is well known that the normalized second-order coherence $G^{(2)}$ increases with
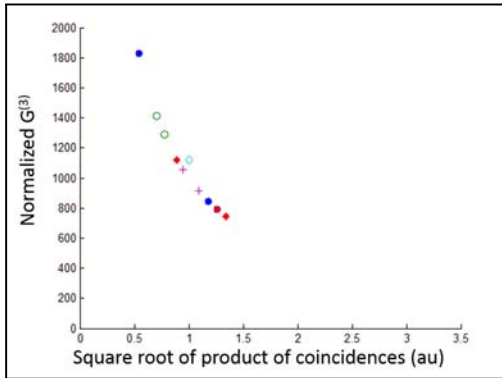
Fig. 29 Normalized triple correlations for experiments run at different times and polarizations.

lower photon flux[59] where a value greater than 2 or less than 1 may indicate quantum non-classicality. $G^{(2)}$ less than 1 is the sub-Poissonian case and greater than 2 is greater than the thermal light case. We are investigating a similar effect with $G^{(3)}$. Formulations analogous to our $G^{(3)}$ have been investigated in other types of systems.[60–63] The normalized 3-fold coincidences $G^{(3)}$ is a ratio of the triple-coincidences to the square root of the product of the probability of 2-photon coincidences. The relationship of the values of $G^{(3)}$ to non-classicality are under investigation and will be described in more detail in future publications.

5.4.8 Entanglement Source, Detection, and Characterization

Entangled photons were generated from a modified entangled photon source. Images of the source and associated measurement electronics are shown in Fig. 30. The wavelengths asso-

Fig. 30 Elements of a teleportation setup including: Entangled photon source, detectors, and photon measurement counting electronics

ciated with the entangled photons generated by the source and pump wavelength are given in Table 4.

Table 4. ARL entangled photon source and detectors

Entangled photon source (1550-1558 nm)	
Pump	1554.1 nm
EP1 (Signal)	1550.92 nm
EP2 (Idler)	1557.36 nm
Two Lasers:	Seed and Amplifier
Timing pulse	1554.1 nm
Entangled photon detectors	
CD1, CD2, CD3, CD4,CD5, CD6	1550 - 1558 nm
IDQ1	1550 - 1558 nm

5.4.9 Entangling Photon Pairs Created at Different Times

It is important to determine the feasibility of entanglement swapping in a fiber network. Prior to having quantum memories we experimentally investigated swapping entanglement between photon pairs created at different times. We performed experiments for this entanglement swapping between photon pairs created in 2 different time bins[45,46] over a laboratory optical network. The experimental setup for these experiments is shown in Fig. 31. In this experiment one photon of each pair of entangled photons generated at time t (i.e., $EP\left(t\right) = P_1\left(t\right) \otimes P_2\left(t\right)$) is delayed such that it can interfere with one photon of an entangled pair generated at time

41

$t + \Delta t$; $EP(t + \Delta t) = P_1 (t + \Delta t) \otimes P_2 (t + \Delta t)$ and the interference would take place, for example, between $P_1 (t)$ and $P_2 (t + \Delta t)$, where EP represents the entangled photon pair and P_1 and P_2 represent the photons that make up the entangled photon pair.
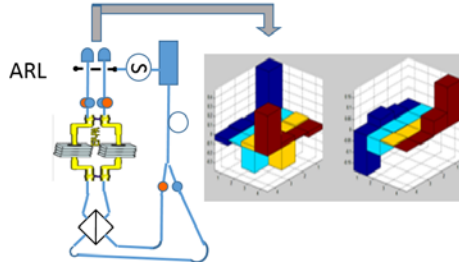
Fig. 31 Experimental setup for entangling photon pairs created at different times. One photon of the entangled photon pairs is delayed such that it will interfere with a photon generated in the next pump pulse on the beam splitter.
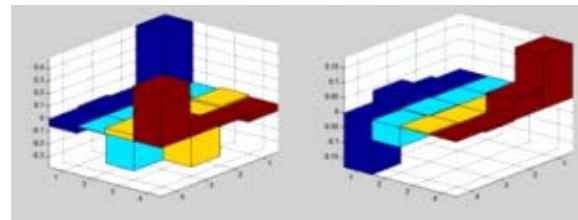
Fig. 32 Initial quantum density matrix tomography measurements: Real (left) and Imaginary (right) portions of density matrix for measurements made at T1 = T2

To characterize the complete quantum density matrix of the 2-photon system for the experiment of Fig. 31 and other experiments, quantum state tomography[14,41,42] was performed on the entangled photon measurements (Fig. 32). In addition to state tomography, we also investigated process tomography[5,14] which can help in the analysis of the teleportation of one or more qubits. Furthermore, Hong-Ou-Mandel (HOM) experiments were performed to test the quantum interference of overlapped entangled photon wavefunctions. Our results indicate that even over a fiber network there is a potential for entanglement swapping between quantum systems.

5.4.10 Teleportation Information Compression Using Conditional Quantum Binary Tree

We designed and patented a system and method protocol to compress and probabilistically optimize information transfer during quantum communication by means of teleportation.[43,44] Data to be sent are compressed and stored among 2^n bits in n qubits via our quantum binary tree (Fig. 33). Data at successive levels of the binary tree are randomly sampled by measurement of quantum outcomes. The receiver of each piece of data indicates what

42

EXAMPLE: 3 QUBITS POTENTIALLY REPRESENT 8 CLASSICAL DATA BINS
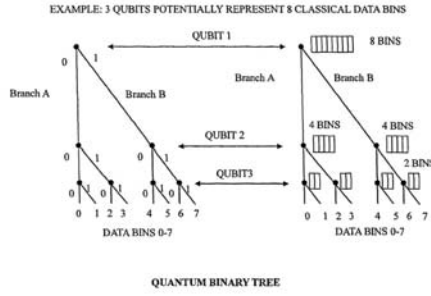
Fig. 33 Quantum binary tree

data were received. The next data sent are further down the tree conditioned on what the receiver received, thus allowing nearly optimal sampling. This algorithm was employed to simulation transmission of an audio speech with over 5,000 to 1 compression. A concept for implementation in hybrid entangled atom and photon setup is depicted in Fig. 34.
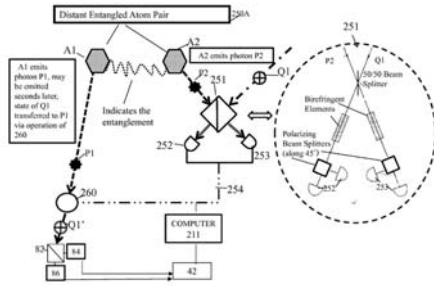
Fig. 34 Teleportation information transmission

5.4.11 Conclusions

In conclusion, we have presented theory for entanglement and the application of entanglement to the teleportation of information between a sender to a receiver. The introduction included background on the notation and described the operations used to recover the state of the teleported qubit. To investigate the potential to teleport information over long distances, we performed experiments to characterize the stability and survivability of entangled photons transmitting over an installed dark fiber loop between ARL and JQI. The round-trip distance was 27 km. The experiments over the 27-km loop using a local clock to gate the detectors indicated that we could improve the coincidence detection rate by using a heralding optical pulse. We then tested schemes for the generation of optical pulses to herald the entangled photon pairs over long-distance paths. These experiments led us to design a WDM

43

implementation for combining the entangled photon pairs and an optical pulse to herald the entangled photon pairs. More experiments were performed investigating polarization drift on the optical fiber loop and those results are detailed later in this report. Prior to performing our probabilistic teleportation experiments, we characterized our entangled photon source with 2-photon interference visibility tests and violation of Bell inequality tests.

For our laboratory probabilistic teleportation experiments, we used a triple-coincidence criteria to record that a valid teleportation occurred. Our preliminary experiments indicated that, based on the triple-coincidence criteria, teleportation was occurring during our experiments. These results indicated that probabilistic teleportation of input states took place over a distance of 2 m in the laboratory. We are designing further improvements to our experimental setup for future follow-on research.

We successfully performed experiments of entanglement swapping between entangled photons generated in different time bins. The results were characterized by the quantum density matrix, which was generated for the 2-photon system using quantum state tomography.

We have developed novel designs for measuring Bell states for probabilistic teleportation and have proposed novel schemes for compression of information sent by teleportation between communicating parties. These designs and schemes were filed and subsequently issued as US patents for the Army.

5.5 References

1.   Meyers, RE, Lee, P, Deacon, KS, Tunick, A, Quraishi, Q, Stack, D. A quantum network with atoms and photons. Proc. SPIE 8518. 2012; 8518–14.

2.   Moehring, DL, Maunz, P, Olmschenk, S, Younge, KC, Matsukevich, DN, Duan, L-M, Monroe, C. Entanglement of single-atom quantum bits at a distance. Nature. 2007; 449, 68–71.

3.   Matsukevich, DN, Maunz, P, Moehring, DL, Olmschenk, S, Monroe, C. Bell inequality violation with two remote atomic qubits. Physical Review Letters. 2008; 100, 150404.

4.   Quantum Internet concept depiction by Meyers, RE, Deacon, KS, Tunick, AD. US Army Research Laboratory; 2011.

5.   Ma, X-S, Kropatschek, S, Naylor, W, Scheidl, T, Kofler, J, Herbst, T, Zeilinger, A, Ursin, R. Experimental quantum teleportation over a high-loss free-space channel. Optics Express. 2012; 20, 23126–23137.

6.   Meyers, RE, Deacon, KS, Tunick, AD. Advanced Free Space Optics: A System Approach. Berlin (Germany): Springer Publishing. Chapter 10, Free-space and atmospheric quantum communications; 2014.

7.   Yin, Y, Ren, J-G, Lu, H, Cao, Y, Yong, H-L, Wu, Y-P, Liu, C, Liao, S-K, Zhou, F, Jiang, Y, Cai, X-D, Xu, P, Pan, G-S, Jia, J-J, Huang, Y-M, Yin, H, Wang, J-Y, Chen, Y-A, Peng, C-Z, Pan, J-W. Quantum teleportation and entanglement distribution over 100-kilometre free-space channels. Nature. 2012;488, 185-188.

8.   Ma, X, Herbst, T, Scheidl, T, Wang, D, Kropatschek, S, Naylor, W, Mech, A, Wittmann, B, Kofler, J, Anisimova, E, Makarov, V, Jennewein, T, Ursin, R, Zeilinger, A. Quantum teleportation using active feed-forward between two Canary Islands. arXiv:1205.3909v1; 2012.

9.   Scheidl, T, Ursin, R, Fedrizzi, A, Ramelow, S, Ma, X, Herbst, T, Prevedel, R, Ratschbacher, L, Kofler, J, Jennewein, T, Zeilinger, A. Feasibility of 300 km quantum key distribution with entangled states. New Journal of Physics. 2009; 11, 085002.

10.   Rogers, LJ, Jahnke, KD, Metsch, MH, Sipahigil, A, Binder, JM, Teraji, T, Sumiya, H, Isoya, J, Lukin, MD, Hemmer, P, Jelezko, F. All-optical initialization, readout, and coherent preparation of single silicon-vacancy spins in diamond. Physical Review Letters. 2014; 113, 263602.

11.   Komar, P, Kessler, EM, Bishof, M, Jiang, L, Sorensen, AS, Ye, J, Lukin, MD. A quantum network of clocks. Nature Physics. 2014; 10, 582–587.

12.   Scarani, V, Lynn, C, Yang, LS. Six Quantum Pieces: A First Course in Quantum Physics. London (UK): World Scientific; 2010.

13.   RP Feynman, RB Leighton, M Sands, The Feynman Lectures on Physics Vol. I–III. Addison Wesley (1997).

14.   Nielsen, MA, Chuang, IL. Quantum Computation and Quantum Information. Cambridge (UK): Cambridge University Press; 2000.

15.   Saleh, BEA, Teich, MC. Fundamentals of Photonics. New York (NY): John Wiley & Sons, Inc; 1991.

16. Shih, YH. An Introduction to Quantum Optics: Photon and Biphoton Physics. Boca Raton (FL): CRC Press, Taylor & Francis, 1st edition; 2011.

17. Meyers, RE, Deacon, KS, Shih, YH. Turbulence-free ghost imaging. Applied Physics Letters. 2011; 98, 111115.

18. Amri, T, Laurat, J, Fabre, C. Characterizing quantum properties of a measurement apparatus: Insights from the retrodictive approach. Physical Review Letters. 2011; 106, 020502.

19. Amri, T. Quantum behavior of measurement apparatus. arXiv:1001.3032; 2010.

20. Martienssen, W, Spiller, E. Coherence and fluctuations in light beams. American Journal of Physics. 1964; 32, 919.

21. Estes, L, Narducci, L, Tuft, R. Scattering of light from a rotating ground glass. Journal of the Optical Society of America. 1971; 61, 1301.

22. Glauber, RJ. Coherent and incoherent states of the radiation field. Physical Review. 1963; 131, 2766–2788.

23. Scully, MO, Zubairy, MS. Quantum Optics. Cambridge (UK): Cambridge University Press, 1st edition; 1997.

24. Hanbury Brown, R. Intensity Interferometer. London (UK): Taylor & Francis; 1974.

25. Sangouard, N, Simon, C, Zhao, B, Chen, Y-A, de Riedmatten, H, Pan, J-W, Gisin, N. Robust and efficient quantum repeaters with atomic ensembles and linear optics. Physical Review A. 2008; 77, 062301.

26. Sangouard, N, Simon, C, de Riedmatten, H, Gisin, N. Quantum repeaters based on atomic ensembles and linear optics. Review of Modern Physics. 2011; 83, 33–80.

27. Cabello, A, Rossi, A, Vallone, G, De Martini, F, Mataloni, P. Proposed Bell experiment with genuine energy-time entanglement. Physical Review Letters. 2009; 102, 040401.

28. Klyshko, DN. Photons and Nonlinear Optics. Boca Raton (FL): CRC press, Gordon & Breach; 1998.

29. Kuo, P, Pelc, J, Slattery, O, Fejer, M, Tang, X. Dual-channel, single-photon upconversion detector near 1300 nm. Proc SPIE 8518. 2012; 8518–28.

30. Tu, H, Jiang, Z, Marks, D, Boppart, S. Intermodal four-wave mixing from femtosecond pulse-pumped photonic crystal fiber. Applied Physics Letters.. 2009; 94, 101109.

31. Halliday, D, Resnick, R, Walker, J. Fundamentals of Physics Extended. 10th Edition. New York (NY): Wiley; 2013.

32. Steinlechner, F, Ramelow, S, Jofre, M, Gilaberte, M, Jennewein, T, Torres, JP, Mitchell, MW, Pruneri, V. Phase-stable source of polarization-entangled photons in a linear double-pass configuration. Optics Express. 2013; 21, 11943–11951.

33. Bennett, CH, Brassard, G, Crepeau, C, Jozsa, R, Peres, A, Wooters, WK. Teleporting an unknown quantum state via dual classical and Einstein-Podolsky-Rosen channels. Physical Review Letters. 1993; 70, 1895–1899.

34. Bouwmeester, D, Pan, J-W, Mattle, K, Eibl, M, Weinfurter, H, Zeilinger, A. Experimental quantum teleportation. Nature. 1997; 390, 575–579.

35. Antonelli, C, Shtaif, M, Brodsky, M. Sudden death of entanglement induced by polarization mode dispersion. Physical Review Letters. 2011; 106.

36. Shtaif, M, Antonelli, C, Brodsky, M. Nonlocal compensation of polarization mode dispersion in the transmission of polarization entangled photons. Optics Express. 2011; 19, 1728–1733.

37. Brodsky, M, George, EC, Antonelli, C, Shtaif, M. Loss of polarization entanglement in a fiber-optic system with polarization mode dispersion in one optical path. Optics Letters. 2011; 36, 43–45.

38. Agrawal, P, Pati, AK. Probabilistic quantum teleportation. Physics Letters A. 2002; 305, 12–17.

39. Roa, L, Groiseau, C. Probabilistic teleportation without loss of information. Physical Review A. 2015; 91, 012344.

40. Azuma, K, Tamaki, K, Lo, H-K. All-photonic quantum repeaters. Nature Communications. 2015; 6, 6787.

41. James, DFV, Kwiat, PG, Munro, WJ, White, AG. Measurement of qubits. Physical Review A. 2001; 64, 052312.

42. White, AG, James, DFV, Eberhard, PH, Kwiat, PG. Nonmaximally entangled states: Production, characterization, and utilization. Physical Review Letters. 1999; 83, 3103–3107.

43. Meyers RE, Deacon KS. Quantum based information system and method. United States patent US 8,503,885 (ARL 04-62CIP), 2013 Aug 6.

44. Meyers RE, Deacon KS. Quantum based information transfer system and method United States patent US 8,983,303 (ARL 04-62CIP2), 2015 Mar 17.

45. Megidish, E, Halevy, A, Shacham, T, Dvir, T, Dovrat, L, Eisenberg, HS. Entanglement swapping between photons that have never coexisted. Physcial Review Letters. 2013; 110, 210403.

46. Wiegner, R, Thiel, C, von Zanthier, J, Agarwal, GS. Quantum interference and entanglement of photons that do not overlap in time. Optics Letters. 2011; 36, 1512–1514.

47. Clausen, C, Bussieres, F, Tiranov, A, Herrmann, H, Silberhorn, C, Sohler, W, Afzelius, M, Gisin, N. A source of polarization-entangled photon pairs interfacing quantum memories with telecom photons. New Journal of Physics. 2014; 16, 093058.

48. Christ, A, Laiho, K, Eckstein, A, Cassemiro, KN, Silberhorn, C. Probing multimode squeezing with correlation functions. New Journal of Physics. 2011; 13, 033027.

49. Nawareg, M, Muhammad, S, Amselem, E, Bourennane, M. Experimental measurement-device-independent entanglement detection. Nature: Scientific Reports. 2015; 5, 8048.

50. Giovannini, D, Romero, J, Padgett, MJ. Interference of probability amplitudes: a simple demonstration within the Hong-Ou-Mandel experiment. Journal of Optics. 2014; 16, 032002.

51. Munro, WJ, Nemoto, K, White, AG. The Bell inequality: a measure of entanglement? Journal of Modern Optics. 2001; 48:7, 1239–1246.

52. Clauser, J, Horne, M, Shimony, A, Holt, R. Proposed experiment to test local hidden-variable theories. Physical Review Letters. 1969; 23:15.

53. Wasak, T, Szankowski, P, Zin, P, Trippenbach, M, Chwedenczuk, J. Cauchy-Schwarz inequality and particle entanglement. Physical Review A. 2014; 90, 033616.

54. Jin, R-B, Takeoka, M, Takagi, U, Shimizu, R, Sasaki, M. Highly efficient entanglement swapping and teleportation at telecom wavelength. Nature: Scientific Reports. 2015; 5, 9333.

55. Shadbolt, P, Vertesi, T, Liang, Y-C, Branciard, C, Brunner, N, O'Brien, JL. Guaranteed violation of a Bell inequality without aligned reference frames or calibrated devices. Nature: Scientific Reports. 2012; 2, 470.

56. Brunner, N, Cavalcanti, D, Pironio, S, Scarani, V, Wehner, S. Bell nonlocality. Reviews of Modern Physics. 2014; 86, 419.

57. Tapster, PR, Rarity, JG. Photon statistics of pulsed parametric light. Journal of Modern Optics. 1998; 45, 595-604.

58. U'Ren, A, Silberhorn, C, Ball, J, Banaszek, K, Walmsley, I. Characterization of the nonclassical nature of conditionally prepared single photons. Physical Review A. 2005; 72, 021802R.

59. Karmakar, S, Meyers, RE. Color controllable polarization entanglement generation in optical fiber at telecommunication wavelengths. Optics Express. 2015; 23:16, 20605–20616.

60. Ding, D-S, Zhang, W, Shi, S, Zhou, Z-Y, Li, Y, Shi, B-S, Guo, G-C. Hybrid-cascaded generation of tripartite telecom photons using an atomic ensemble and a nonlinear waveguide. Optica. 2015; 2, 642-645.

61. Stevens, M, Glancy, S, Nam, S, Mirin, R. Third-order antibunching from an imperfect single-photon source. Optics Express. 2014; 22:3, 3244-3260.

62. Slodicka L. Generation of correlated photons with time resolution [thesis]. [Olomouc (Czech Republic)]: Palacky University; 2008.

63. Varnava, C, Stevenson, R, Nilsson, J, Skiba-Szymanska, J, Dzurnak, B, Lucamarini, M, Penty, R, Farrer, I, Ritchie, D, Shields, A. An entangled-LED driven quantum relay over 1 km. arXiv:1506.00518v2; 2015; Jun.

64. Nilsson, J. Electrically generated entangled light for optical quantum information applications [thesis]. Université Blaise Pascal-Clermont-Ferrand II; 2013.

65. Kheruntsyan, K, Jaskula, J, Deuar, P, Bonneau, M, Partridge, GB, Ruaudel, J, Lopes, R, Boiron, D, Westbrook, C. Violation of the Cauchy-Schwarz inequality with matter waves. Physical Review Letters. 2012; 108, 260401.

49

66. Reid, M, Walls, D. Violations of classical inequalities in quantum optics. Physical Review A. 1986; 34, 1260.

67. Glauber, R. The quantum theory of optical coherence. Physical Review. 1963; 130, 2529.

68. Miranowicz, A, Bartkowiak, M, Wang, X, Liu, Y-X, Noril, F. Testing nonclassicality in multimode fields: A unified derivation of classical inequalities. Physical Review A. 2010; 82, 013824.

69. Bartkowiak, M. Experimentally-friendly methods of generation and detection of quantum correlations [thesis]. [(Poland)]: Adam Mickiewicz University; 2012.

70. Srivathsan, B. Heralded single photons for efficient interaction with single atoms [thesis]. [Singapore)]: National University of Singapore; 2015.

71. Nilsson, J, Steverson, R, Chan, K, Skiba-Szymanska, J, Lucamarini, M, Bennett, A, Salter, C, Farrer, I., Ritchie, D., Shields, A. Quantum teleportation using a light-emitting diode. Nature Photonics. 2013; 7, 311–315.

72. Varnava, C, Stevenson, R, Nilsson, J, Skiba-Szymanska, J, Dzurnak, B, Lucamarini, M, Penty, R, Farrer, I, Ritchie, D, Shields, A. An entangled-LED-driven quantum relay over 1 km. Nature: Quantum Information. 2013; 2, 16006.

73. Khoshnegar, M, Huber, T, Predojevic, A, Dalacu, D, Prilmuller, M, Lapointe, J, Wu, X, Tamarat, P, Lounis, B, Poole, P, Weihs, G, Majedi, H. Bright solid state source of photon triplets. arXiv:1510.05898v1; 2015.

74. Takesue, H, Dyer, S, Stevens, M, Verma, V, Mirin, R, Nam, S-W. Quantum teleportation over 100 km of fiber using highly efficient superconducting nanowire single-photon detectors, Optica 2015; 2(10), 832-835.

75. Kwiat, P, Chiao, R. Observation of a non-classical Berry's phase for the photon, Physical Review Letters 1991; 66(5) 588-591.

76. Grangier, P, Roger, G, Aspect, A. Experimental evidence for a photon anticorrelation effect on a beam splitter: A new light on singer photon interferences, Europhys. Lett 1986; 1 173-179.

77. Meyers RE, Deacon K. Unpublished material, 2016.

50

6. Telecom-Wavelength Conversion for Quantum Communications

Authors: Sanjit Karmakar, Ronald E Meyers, Keith S. Deacon

6.1 Introduction

Because of the scarcity of suitable ground-state atomic transitions, quantum memories are not often available at telecommunication wavelengths. Most of the quantum memories reported have been in the wavelength range of 700–800 nm.[1–4] On the other hand, telecommunication optical fibers have their lowest losses of 0.2 dB/km in the optimal telecom wavelength of around 1.5 μm. Because of the low transmission loss in telecommunication fibers, down conversion to telecom-wavelengths is essential for long-distance quantum communications. Alternately, at typical quantum memory-wavelengths in the range of 700–800 nm, detection efficiencies can be very high. Hence, for the purpose of measurement, one may up convert the telecom-wavelength photons to a memory wavelength. In this section, we propose an experimental configuration with its theoretical explanation to down convert quantum memory photons to telecom wavelengths with high conversion efficiency. We also propose a second configuration for the conversion of telecom-wavelength photons to the quantum memory wavelength for measurement purposes to take the advantage of higher efficiency detection systems. While frequency conversion efficiencies that occur in atomic ensembles of Rb via FWM in a diamond configuration are usually very low due to the low absorption of the input beam, below we find in our analysis that the conversion efficiencies could be as high as 90.5% for the down conversion case and 96% in the up conversion case by implementing the idea of EIT.

6.2 Down Conversion to Telecom Wavelengths

6.2.1 Proposed Experiment

Without applying any frequency conversion processes, the 795-nm signal beam would otherwise be propagated through the telecommunication fiber. However, to minimize large transmission losses in optical fiber at 795 nm, the 795-nm photons are down-converted to telecom-wavelength photons at 1.53 μm . The signal field of the 795-nm photons is incident on an ultra-cold atomic ensemble of ^{87}Rb for down-conversion via a FWM process.[5–8,12] The atomic ensemble of ^{87}Rb is prepared in a cell of length L at ground state $|g\rangle$. Figure 35 shows the fields at their corresponding frequencies are coupling at the 4 levels of the atomic system.

51

The signal field E_1 couples the transition $|g\rangle \rightarrow |c\rangle$, the pump II field E_2 couples the transition $|c\rangle \rightarrow |e\rangle$, and the pump I field E_4 couples the transition $|g\rangle \rightarrow |d\rangle$. Following energy and momentum conservation, the FWM process generates photons of wavelength 1.53 μm, which is resonant with the transition $|d\rangle \rightarrow |e\rangle$.
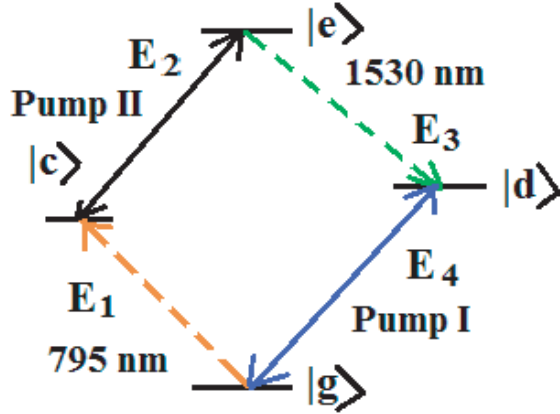
Fig. 35 Diamond configuration of frequency down conversion in ^{87}Rb atomic ensemble to generate telecom-wavelength. The energy levels in this diamond configuration are $|g\rangle = |5S_{1/2}, F = 1 >, |c\rangle = |5P_{1/2}, F = 2 >$, $|d\rangle = |5P_{3/2}, F = 2 >$ and $|e\rangle = |5D_{5/2}, F = 3 >$. Here 4 level atomic interaction through FWM occurs with input fields E_1, E_2 and E_4 with their corresponding angular frequencies $\omega_s(795\ nm)$, $\omega_{II}(1.48\ \mu m)$, and $\omega_I(780\ nm)$ respectively, and generates telecom wavelengths of $\omega_t(1.53\ \mu m)$.

6.2.2 Discussion and Analysis

When the 795-nm signal beam passes through the atomic ensemble at ground state $|g\rangle$, the signal is strongly absorbed as it is tuned through resonance.[9–11] This absorption of signal photons significantly affects conversion efficiency. However, some of the absorption can be mitigated by implementing the FWM process in a region of high transparency. As an example, if pump II is turn on and the signal beam then passes through the atomic ensemble at ground state $|g\rangle$, the signal beam will be resonantly transmitted. This process is shown in Fig. 35 and the explanation is given as follows.

After solving the wave equation,[6–8] we have

$$E_1 = E_1(0)exp\left[\frac{\omega_s z}{2c}Im\chi^{(1)}\right] \tag{19}$$

where ω_s is the angular frequency of the signal beam, $Im\chi^{(1)}$ is the imaginary part of the first-order susceptibility and $E_1(0)$ is the incident signal field at the Rb cell at $z = 0$. When

52

pump II is on and the signal passes through the ^{87}Rb cell, the signal beam is resonantly transmitted and the first-order susceptibility $\chi^{(1)}$ is

$$\chi^{(1)} = -\frac{|\mu_{gc}|^2 N}{\hbar} \frac{\Delta_{ge} - i\Gamma_{ge}}{(\Delta_{gc} - i\Gamma_{gc})(\Delta_{ge} - i\Gamma_{ge}) - \frac{|\Omega_{II}|^2}{4}} \tag{20}$$

where Γ_{gc} and Γ_{ge} are the decay rates of the transition $g \to c$, $g \to e$, respectively, Δ_{gc} and Δ_{ge} are their corresponding detuning; Ω_{II} is the Rabi frequency of pump II; μ_{gc} is the dipole moment of the transition $g \to c$; and N is the atomic density of ^{87}Rb.

The above equation can be rewritten as

$$\chi^{(1)} = -\frac{|\mu_{gc}|^2 N}{\hbar} \frac{(\Delta_s + \Delta_{II}) - i\Gamma_{ge}}{(\Delta_s - i\Gamma_{gc})[(\Delta_s + \Delta_{II}) - i\Gamma_{ge}] - \frac{|\Omega_{II}|^2}{4}} \tag{21}$$

where $\Delta_{gc} = \Delta_s$, $\Delta_{ge} = \Delta_s + \Delta_{II}$. Δ_s and Δ_{II} are the detuning of the signal and pump II, respectively.

Now the imaginary part of $\chi^{(1)}$ can be expressed as follows:

$$Im\chi^{(1)} = -\frac{|\mu_{gc}|^2 N}{\hbar} \frac{(\Delta_s + \Delta_{II})^2\Gamma_{gc} + \Gamma_{ge}(\frac{|\Omega_{II}|^2}{4} + \Gamma_{gc}\Gamma_{ge})}{[(\Delta_s + \Delta_{II})\Delta_s - \Gamma_{gc}\Gamma_{ge} - \frac{|\Omega_{II}|^2}{4}]^2 + [(\Delta_s + \Delta_{II})\Gamma_{gc} + \Delta_s\Gamma_{ge}]^2}. \tag{22}$$

Then Eq. 19 can be rewritten as

$$E_1 = E_1(0)exp\left[-\frac{1}{2}OD(z)f(\Delta_s)\right] \tag{23}$$

where $OD(z) = \frac{|\mu_{gc}|^2 N\omega_s z}{c\hbar}$ is the optical depth at z and

$$f(\Delta_s) = \frac{(\Delta_s + \Delta_{II})^2\Gamma_{gc} + \Gamma_{ge}(\frac{|\Omega_{II}|^2}{4} + \Gamma_{gc}\Gamma_{ge})}{[(\Delta_s + \Delta_{II})\Delta_s - \Gamma_{gc}\Gamma_{ge} - \frac{|\Omega_{II}|^2}{4}]^2 + [(\Delta_s + \Delta_{II})\Gamma_{gc} + \Delta_s\Gamma_{ge}]^2}. \tag{24}$$

In this case, $\Gamma_{gc} = 2\pi \times 2.88$ MHz, $\Gamma_{ge} = 2\pi \times 0.8$ MHz, and $\Gamma_{gd} = 2\pi \times 3$ MHz. The parameters $\Delta_I = 2\pi \times 41$ MHz, $\Delta_{II} = 2\pi \times 5$ MHz, $\Omega_I = 2\pi \times 4.8$ MHz, $\Omega_{II} = 2\pi \times 50$ MHz, and optical depth$= 2\pi \times 150$ MHz are chosen to have an optimized conversion efficiency. Here Ω_I is the Rabi frequency of pump I. Figure 36 shows the intensity of the signal beam ($I_1 = |E_1|^2$) plotted against the detuning of the signal beam (Δ_s), which shows the transmission window after turning on pump II.

In Fig. 36, the blue line shows that the absorption takes place when the signal beam is passed through the ^{87}Rb cell without turning on pump II. Alternately, the red line presents the high transparency regime of the signal beam after turning on the pump II. Now by further application of the pump I, the signal beam can be converted to telecom wavelength with high conversion efficiency.
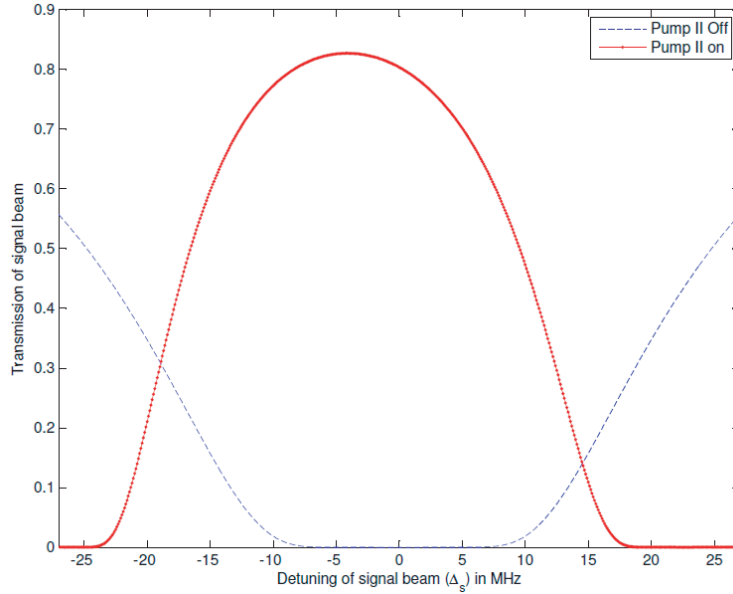
Fig. 36 Transmission window of the signal beam

The conversion efficiency is defined as

$$\eta_t = \frac{I_3(z = L)}{I_1(z = 0)} = \frac{|E_3(z = L)|^2}{|E_1(z = 0)|^2} \tag{25}$$

where I_1 and I_3 are the intensities of the input signal beam and converted telecom wavelength, respectively, and L is the length of the Rb cell.

When considering the phase-matching condition in the emission of telecom wavelength in field 3, the wave equation[6-8] is given by

$$\frac{\partial E_3}{\partial z} = -\frac{3}{4}\frac{\omega_t}{c}\chi^{(3)}E_1 E_2 E_4 \tag{26}$$

54

or

$$\frac{\partial E_3}{\partial z} = -a\chi^{(3)} E_1 \tag{27}$$

where $a = \frac{3}{4}\frac{\omega_t}{c} E_2 E_4$ and ω_t is the angular frequency of the telecom wavelength.

After solving the above equation with boundary condition of $E_3(0) = 0$, we have

$$E_3(z) = -\frac{2ca\chi^{(3)}}{\omega_s Im\chi^{(1)}} E_1(0)\left[exp\left(\frac{\omega_s z}{2c}Im\chi^{(1)}\right) - 1\right] \tag{28}$$

where ω_s is the angular frequency of the signal beam. For this case, the third-order suscep-
tibility $\chi^{(3)}$ is given by

$$\chi^{(3)} = \frac{\mu_{gc}\mu_{ce}\mu_{ed}\mu_{gd}}{6\hbar^3}\frac{1}{\Delta_I + i\Gamma_{gd}}\frac{1}{(\Delta_s - i\Gamma_{gc})\left[(\Delta_s + \Delta_{II}) - i\Gamma_{ge}\right] - \frac{|\Omega_{II}|^2}{4}}. \tag{29}$$

Let us consider $L = 1$ cm. Then, at $z = L$ the term $exp\left(\frac{\omega_s z}{2c}Im\chi^{(1)}\right)$ becomes much less than
unity (i.e., $exp\left(\frac{\omega_s z}{2c}Im\chi^{(1)}\right) \ll 1$). Now the $E_3(z)$ becomes

$$E_3(z = L) = \frac{2ca\chi^{(3)}}{\omega_s Im\chi^{(1)}} E_1(0). \tag{30}$$
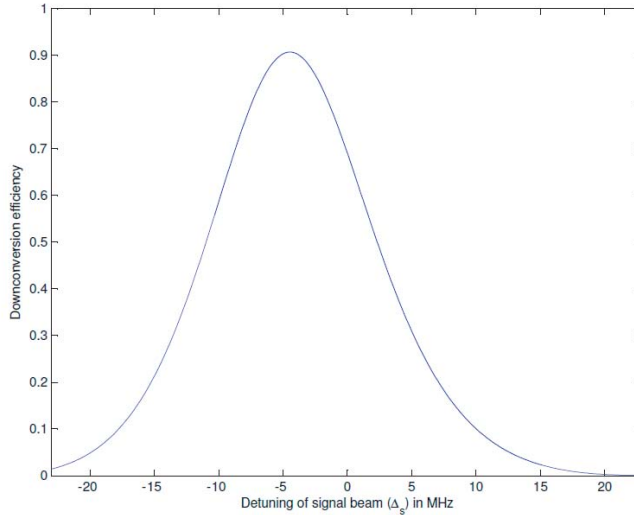
Fig. 37 Down-conversion efficiency of the signal beam into the telecom wavelength

55

Then the conversion efficiency becomes

$$\eta_t = \frac{|E_3(z=L)|^2}{|E_1(z=0)|^2} = \left(\frac{3}{2}\frac{\omega_t}{\omega_s}\right)^2 |E_2|^2 |E_4|^2 \left(\frac{|\chi^{(3)}|}{Im\chi^{(1)}}\right)^2. \tag{31}$$

After substituting $\chi^{(3)}$ and $Im\chi^{(1)}$, the conversion efficiency is as follows:

$$\eta_t = \left(\frac{1}{4}\frac{\omega_t}{\omega_s}|\Omega_I||\Omega_{II}|\right)^2 \frac{1}{\Delta_I^2 + \Gamma_{gd}^2} \frac{[(\Delta_s + \Delta_{II})\Delta_s - \Gamma_{gc}\Gamma_{ge} - \frac{|\Omega_{II}|^2}{4}]^2 + [(\Delta_s + \Delta_{II})\Gamma_{gc} + \Delta_s\Gamma_{ge}]^2}{\left[(\Delta_s + \Delta_{II})^2\Gamma_{gc} + \Gamma_{ge}(\frac{|\Omega_{II}|^2}{4} + \Gamma_{gc}\Gamma_{ge})\right]^2}$$

where the dipole moments are $\mu_{gd} \simeq \mu_{gc} \simeq 4.2ea_0$ and $\mu_{ce} \simeq \mu_{ed} \simeq 4.2ea_0$. Now Fig. 37 shows the down-conversion efficiency plotted against the detuning of the signal beam. From Fig. 37, it is clear that the maximum achievable conversion efficiency to telecom-wavelengths is 90.5%[1].

To further illustrate the frequency conversion process in the Rb cell, we show the intensity profiles of the signal beam and the converted telecom beam in Fig. 38, where the maximum transmission of the signal beam is at $\Delta_s = 4.1$ MHz. From Fig. 38, it is clear that the conversion process occurs at every point of the Rb cell.[2]
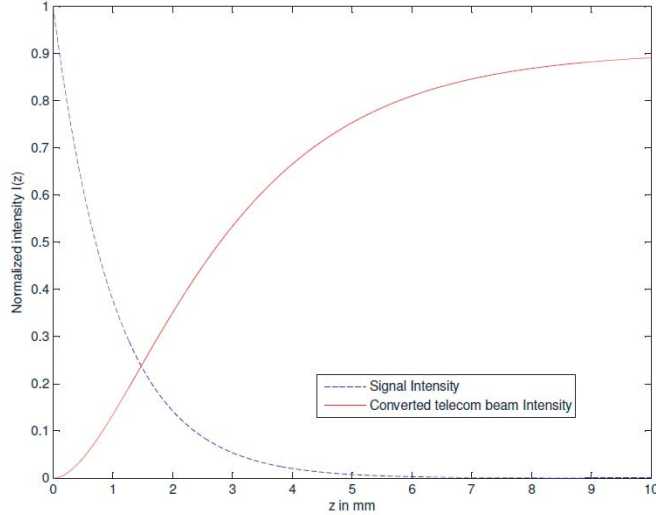
Fig. 38 Intensity profiles of the signal beam and converted telecom beams in a down-conversion process

---

[1] The peak efficiency is not centered at $\Delta_s = 0$ due to ac Stark shift.

[2] The predicted maximum efficiency from Fig. 38 is 89%, which is a little lower than in the above calculation of efficiency because of neglecting the term $exp\left(\frac{\omega_s z}{2c}Im\chi^{(1)}\right)$ due to its comparatively low value.

6.3 Up Conversion to Memory Wavelength

6.3.1 Proposed Experiment

The telecom wavelength photons can be up converted to the atomic memory wavelength through a FWM process, wherein the memory wavelength photons are much more efficient for measurement with high quality photon detection systems at this wavelength. This proposed experimental scheme is shown in Fig. 39. When the telecom field is passed through the Rb cell at state $|d\rangle$ pumped from state $|g\rangle$ by pump I, it is strongly absorbed as it tuned through resonance. But when pump II is turn on (before starting this process), the system acts as EIT and creates a regime of transparency to pass the telecom field for up conversion. This process is analogous to that described earlier for down conversion. Afterward, the telecom field is converted to the signal field via FWM processes with a high frequency conversion efficiency.
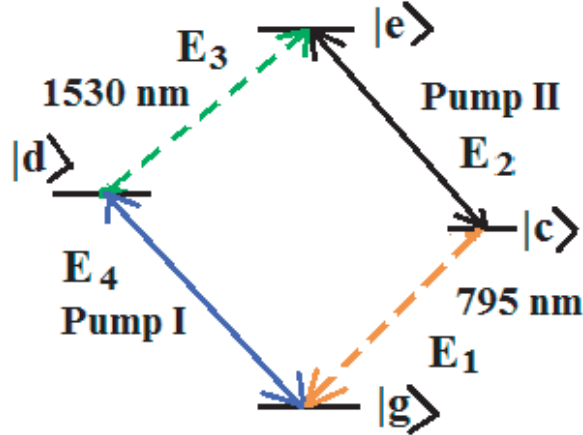
Fig. 39 Diamond configuration of frequency up conversion in ^{87}Rb atomic ensemble to generate memory wavelength. The energy levels in this diamond configuration are $|g\rangle = |5S_{1/2}, F = 1 >$, $|c\rangle = |5P_{1/2}, F = 2 >$, $|d\rangle = |5P_{3/2}, F = 2 >$ and $|e\rangle = |5D_{5/2}, F = 3 >$. Here 4 level atomic interaction through FWM occurs with input fields E_2, E_3 and E_4 with their corresponding frequencies $\omega_{II}(1.48\ \mu m)$, $\omega_t(1.53\ \mu m)$, and $\omega_I(780\ nm)$, respectively, and generates memory wavelengths of $\omega_s(795\ nm)$.

57

6.3.2 Discussion and Analysis

In the following, we analyze the up conversion process. At first, we solve the wave equation for the input telecom field E_3 in the ^{87}Rb cell, where it can be written as follows:

$$E_3(z) = E_3(0)exp\left[-\frac{1}{2}OD'(z)f'(\Delta_s)\right] \tag{32}$$

where $E_3(0)$ is the incident telecom field in the Rb cell at z=0, $OD'(z) = \frac{|\mu_{de}|^2 N\omega_t z}{c\hbar}$ is the optical depth at z and

$$f'(\Delta_s) = \frac{\Delta_s^2\Gamma_{ge} + \Gamma_{gc}(\frac{|\Omega_{II}|^2}{4} + \Gamma_{gc}\Gamma_{ge})}{[(\Delta_s + \Delta_{II})\Delta_s - \Gamma_{gc}\Gamma_{ge} - \frac{|\Omega_{II}|^2}{4}]^2 + [(\Delta_s + \Delta_{II})\Gamma_{gc} + \Delta_s\Gamma_{ge}]^2}. \tag{33}$$

After calculating the output field and simplifying as in the previous down-conversion case, the up-conversion efficiency can be expressed as follows:

$$\eta_s = \left(\frac{1}{4}\frac{\omega_s}{\omega_t}|\Omega_I||\Omega_{II}|\right)^2 \frac{1}{\Delta_I^2 + \Gamma_{gd}^2} \frac{[(\Delta_s + \Delta_{II})\Delta_s - \Gamma_{gc}\Gamma_{ge} - \frac{|\Omega_{II}|^2}{4}]^2 + [(\Delta_s + \Delta_{II})\Gamma_{gc} + \Delta_s\Gamma_{ge}]^2}{\left[\Delta_s^2\Gamma_{ge} + \Gamma_{gc}(\frac{|\Omega_{II}|^2}{4} + \Gamma_{gc}\Gamma_{ge})\right]^2} \tag{34}$$

where the dipole moments are $\mu_{gd} \simeq \mu_{gc} \simeq 4.2ea_0$ and $\mu_{ce} \simeq \mu_{ed} \simeq 4.2ea_0$. In this case, the same parameters are chosen as those for the down-conversion case (i.e., with the optical depth= $2\pi \times \frac{\omega_t}{\omega_s} \times 150$ MHz=$2\pi \times 78.13$ MHz so as to bring about the most optimal conversion efficiency). Figure 40 shows that the maximum achievable efficiency for this up-conversion process is 96%. Note again that the peak efficiency is not centered at $\Delta_s = 0$ due to the ac Stark shift.

To further illustrate the proposed up-conversion process, Fig. 41 shows the intensity profiles of both the telecom field and up-converted signal field at every point inside the Rb cell. Figure 41 clearly shows that telecom beam is up-converted to the signal beam inside the Rb cell.
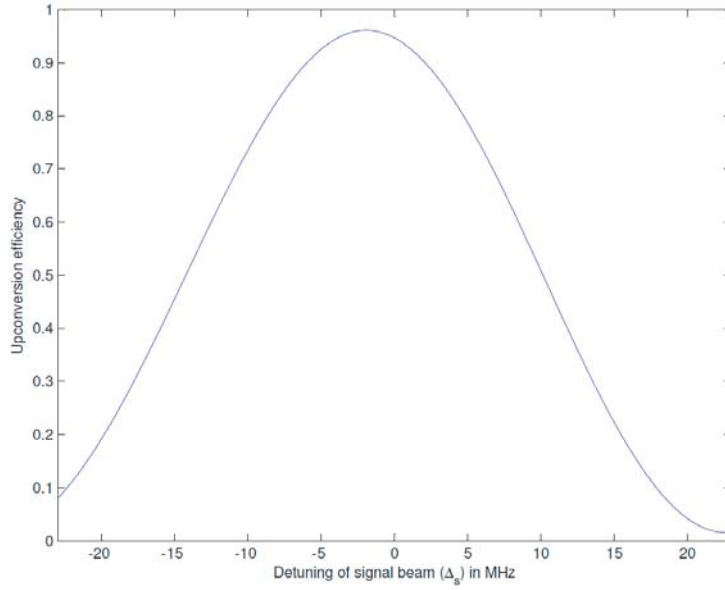
Fig. 40 Up-conversion efficiency of the telecom beam into memory-wavelength

6.4   Conclusion

For long-distance communications, a low-loss quantum channel is needed. Yet, the transmission through optical fiber of photons generated via atomic transitions can be significantly impeded over long distances because of very high losses at these wavelengths. However, at telecom wavelengths the losses are much smaller; hence, the necessity to implement frequency down conversion to telecom wavelengths where the losses are much smaller. On the other hand, the very high detection efficiency of photon measurement systems at quantum memory wavelengths makes a high efficiency up-conversion process desirable to retrieve quantum information transmitted via telecom wavelength photons.

The main concern for both frequency down conversion and frequency up conversion to achieve a robust quantum network is the need for high conversion efficiency. While frequency conversion efficiencies that occur in atomic ensembles of Rb via FWM in a diamond configuration are usually very low due to absorption of the input beam, we found in our analysis that the conversion efficiencies can be as high as 90.5% for the down-conversion case and 96% in the up-conversion case by implementing the idea of EIT. Here, a high transparency regime can be created to overcome the problem of low conversion efficiency. We expect that our proposed configurations will enable progress toward future quantum communication networks over long distances.

59
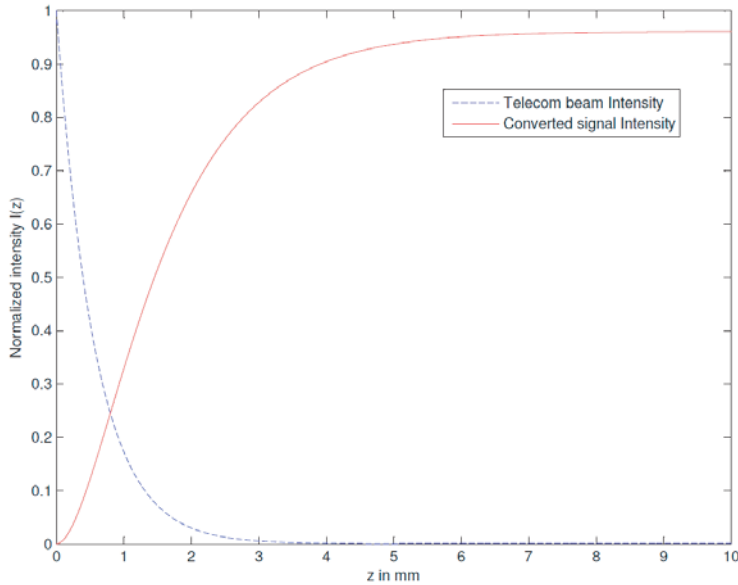
Fig. 41 Intensity profiles of the telecom beam and converted signal beams in a up-conversion process as a function of the position (z) in side the Rb cell

6.5　References

1.　　　　Specht, HP, et al. Nature. 2011; 473, 190.

2.　　　　Zhao, R, et al. Nature Physics. 2009; 5, 100.

3.　　　　Zhao, B, et al. Nature Physics. 2009; 5, 95.

4.　　　　Sangouard, N, et al. Review of Modern Physics. 2011; 83, 33.

5.　　　　Radnaev, AG, et al. Nature Physics. 2010; 6, 894.

6.　　　　Becerra, FE, et al. Physical Review A. 2010; 82, 043833.

7.　　　　Becerra, FE, et al. Physical Review A. 2008; 78, 013834.

8.　　　　Willis, RT, et al. Physical Review A. 2009; 79, 033814.

9.　　　　Harris, SE, et al, Physical Review Letters. 1990; 64, 1107.

10.　　　Field, JE, et al. Physical Review Letters. 1991; 67, 3062.

11.　　　Boller, K-J, et al. Physical Review Letters. 1991; 66, 2593.

12.　　　Wang, G, et al. Optics Letters. 2010; 35, 3778.

7. Color-Controllable Polarization Entanglement Generation

Authors: Sanjit Karmakar, Ronald E Meyers

7.1 Introduction

Entanglement, a quantum mechanical phenomenon in which the interacting states of 2 or more quantum systems cannot be described independently, is vital to a wide range of new technologies such as quantum imaging,[1–6] quantum computing,[7,8] and teleportation.[9,10]

Despite its importance, robust entangled photon generation and control with specific needed wavelengths (colors) is difficult to achieve. Two common sources of entangled light are based on non-linear optical interaction of parametric down conversion (PDC) and FWM in both spontaneous (SPDC, SFWM) and stimulated regimes. The SPDC process is commonly used to generate entangled photon pairs.[11–13] In addition, waveguide SPDC was developed to increase the rate of entangled photon pair generation (i.e., the brightness).[14,15] Nevertheless, SPDC in bulk crystals and waveguides is limited by the spectral width of the pump source. Yet, this limitation could be overcome by using the quasi-phase matching, birefringence, and self-phase or cross-phase modulation features of the material.

Because optical fiber is well suited for the transmission of quantum information, the progress of photon pair generation in optical fibers by FWM has gained a great deal of attention.[16–21] However, FWM presents a high probability of Raman noise contamination of the idler photon of the generated pair specifically at low pump power. Fortunately, optical fibers also have a third-order nonlinearity feature for self-phase and cross-phase modulations. These modulation effects can be used to generate 2 specified colors (wavelengths) of entangled photon pairs at a high rate.

We propose a polarization entanglement source in optical fiber at telecommunication wavelengths that features the controllable generation of specified colors (wavelengths) of entangled photon pairs.[22] In particular, this proposed experiment builds on and can be distinguished from earlier work by Fang,[18] Li,[19] and Takesue[21] by our use of increased peak pulse power to tune the phase matching conditions in the optical fiber. This tuning ability enables the generation of entangled photon pairs at separated (e.g., 50-nm separation at 100-mW) average pump powers that will help mitigate Raman contamination from the pump into the wavelengths of the entangled photon pairs.

61

7.2 Experimental Setup

The experimental setup for the color-controllable polarized entanglement source will probabilistically generate polarization entangled photons according to the quantum wavefunction:

$$|\Psi_p\rangle = \frac{1}{\sqrt{2}}\Big[|H\rangle_s|H\rangle_i + e^{2i\phi_p}|V\rangle_s|V\rangle_i\Big]. \tag{35}$$

Here, the relative phase between the 2 orthogonally polarized pump pulses is given by ϕ_p; the horizontally and vertically polarized pulses are H and V. As usual, s represents the signal and i is the idler. Appropriate settings of ϕ_p and a half-wave plate can be used to produce all 4 Bell states in the polarization degree of freedom.[19]
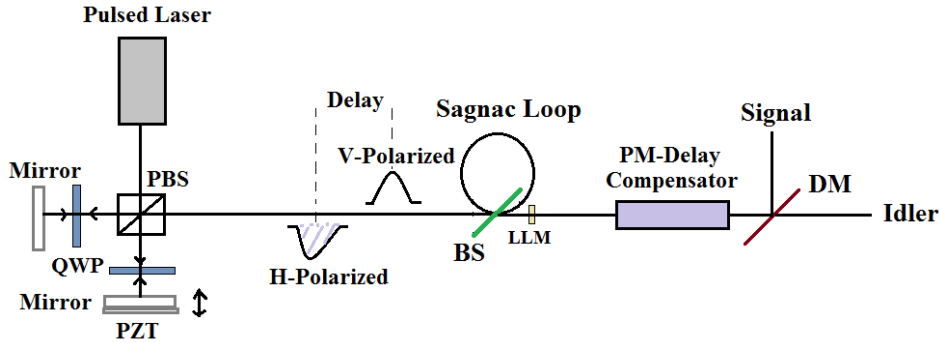
Fig. 42 Schematic of the proposed experimental setup to generate color controllable signal and idler photon pairs. BS is a 50-50 beam splitter and DM is a dichroic mirror that transmits idler photons and reflects signal photons. PM is polarization maintaining and PBS is a polarized beam splitter. LLM is a laser line mirror, which is used to remove the pump photons. V- and H- represent vertical and horizontal polarization, respectively. Also, PZT is a piezoelectric transducer driven translation stage that controls the delay between V-polarized and H-polarized pulses. Later, a PM-delay compensator is used to compensate the delay to overlap H- and V- polarized signal and idler photons. Two quarter wave plates (QWPs) are also used to avoid reflection back into the laser.

Figure 42 shows a schematic of the proposed experimental setup to generate signal and idler photon pairs in an optical fiber. A pump pulse is passed to a Sagnac loop through a 50-50 beam splitter. The Sagnac loop consists of a non-polarization maintaining optical fiber with a polarization controller, which is used to maintain polarization of the signal and idler to be the same as that of the pump. The FWM process occurs in the Sagnac loop to generate signal-idler photon pairs. A photon pair is created in each of the clockwise and counter-clockwise propagating Sagnac loop paths with equal probability producing superposition and interference.[18]

In the experiment, a delay of a few picoseconds (ps) is introduced between 2 orthogonally polarized pump pulses by adjusting the mirror mounted on a piezoelectric-transducer (PZT)

driven translation stage. This precisely adjusts the relative delay (i.e., phase difference) between the 2 orthogonally polarized pump pulses. When the H and V temporal indistinguishability is restored by the polarized-maintained (PM) delay compensator the generated state is given by Eq. 35, where ϕ_p is the relative phase between the states. After the delay compensator, the generated signal and idler photons in the Sagnac loop are passed through a dichroic mirror to separate the signal and idler photons.

In a FWM process, 2 pump photons of angular frequencies ω_p are converted to 2 daughter photons at angular frequencies ω_s and ω_i in a third-order nonlinear optical material, such as optical fiber. This third-order nonlinearity generates 2 side bands (i.e., signal and idler beams). During this process, energy is conserved and the phase-mismatch Δk is 0. Conditions for the co-polarized (i.e., pump, signal and idler have the same polarization) case are[17,23]

$$2\omega_p = \omega_s + \omega_i \tag{36}$$

$$\Delta k = 2\frac{\omega_p}{c}n(\omega_p) - \frac{\omega_s}{c}n(\omega_s) - \frac{\omega_i}{c}n(\omega_i) - \gamma P_p \tag{37}$$

where s and i refer to the signal and idler photons, respectively; γ is the nonlinear parameter of the fiber; P_p is the pump peak power; and $n(\omega)$ is the refractive index at angular frequency ω. At high pump peak power, the self- or cross-phase modulation term (a self/cross-phase modulation contribution comes from the 2 pumps each with peak power P_p), γP_p, can control the phase-matching where $\gamma = \frac{3\pi|\chi^{(3)}|}{2\lambda_p A_{eff} n^2 \epsilon_0 c} = \frac{2\pi n_2}{\lambda_p A_{eff}}$, n_2 is nonlinear index of the material and λ_p is center wavelength of the pump. The terms n, A_{eff} and $\chi^{(3)}$ are average refractive index, effective mode area and third-order susceptibility of the nonlinear fiber medium, respectively.

7.3 Analysis of Entangled Photons Generated, Color Controllability, and Noise Coincidences

7.3.1 Raman Noise

Now a laser with a 1560-nm emission wavelength, average power of 100-mW, repetition rate of 73.4 MHz, and a pulse duration of 150 fs is considered as the pump to generate signal and idler beams in an optical fiber. Here pump, signal, and idler are considered as being in an extraordinary polarized state. Using Eq. 36, Eq. 37, and Sellmeier's equations,[24] Fig. 43 shows the phase matching for the 1560-nm pump having 100-mW average power. From Fig. 43, we can see that phase matching occurs at a signal wavelength of 1532 nm at an average power of 100 mW, where the corresponding idler wavelength would be 1589 nm. Similarly, the occurrence of phase matching for other average pump powers of 200 and 300 mW are shown in Fig. 43 and illustrate how phase matching would shift with average pump power.

Figure 44 displays the variation of the signal and idler wavelengths with the pump power. Again, we can see that as the pump power increases, both wavelengths of signal and idler photons move away from that of the pump photons. At low power, the wavelength of the signal and idler photons are very close to that of the pump.
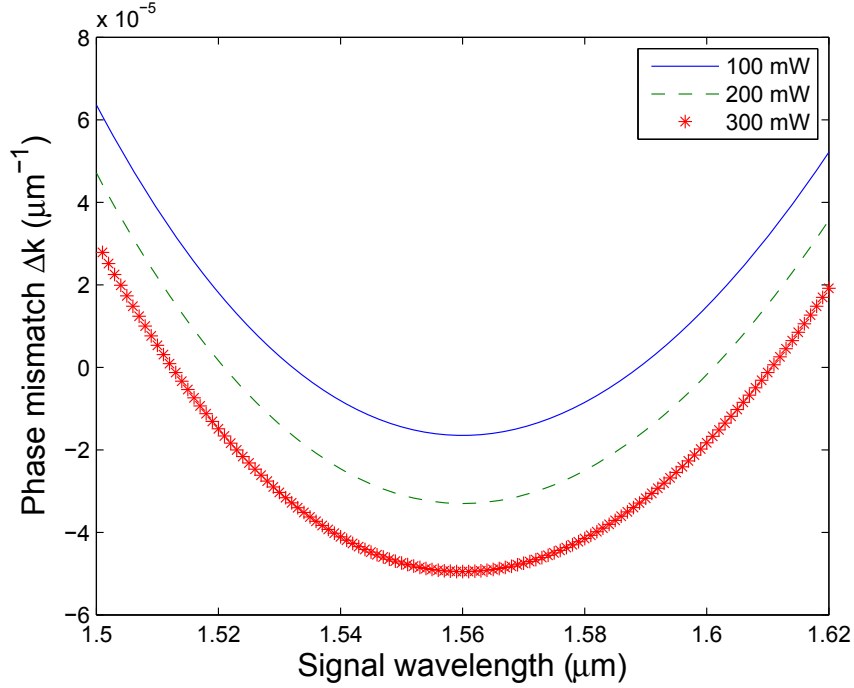
Fig. 43 Phase matching for a 1560-nm pump for 3 average pump powers

For a 1560-nm pump, stimulated Raman scattering would bring about a red-shift of approximately 100 nm.[25] As a result, the generated idler photons would have a high probability of Raman contamination. In general, for stimulated Raman contamination to occur a minimum pump power called the threshold pump power is needed. The Raman threshold pump can be defined as[26] $P_{th} \simeq \frac{16\,A_{eff}}{g_R\,L_{eff}}$, where $A_{eff} = 76.94\mu m^2$ is the mode area of the fiber and $g_R = 6.34 \times 10^{-12}$ is the Raman gain in cm/W.[25] At 1560 nm, $L_{eff} = 22$ km. Thus, the Raman threshold would be 882 mW. In this case, the fiber length (L) is 20 cm, which is much smaller than $L_{eff} = 22$ km, and the threshold power can be rewritten as $P_{th} \simeq \frac{16\,A_{eff}}{g_R\,L} = 97\,kW$.

In addition, the 1560-nm pump has a 150-fs pulse duration, a 73.4-MHz repetition rate, and a 100-mW average power to generate entangled photon pairs from each pulse. These specifications of the pump equate to a peak power of 9.08 kW, which is much smaller than the Raman threshold power. Hence, in this implementation, there would be negligible probability of contamination due to stimulated Raman scattering.

64
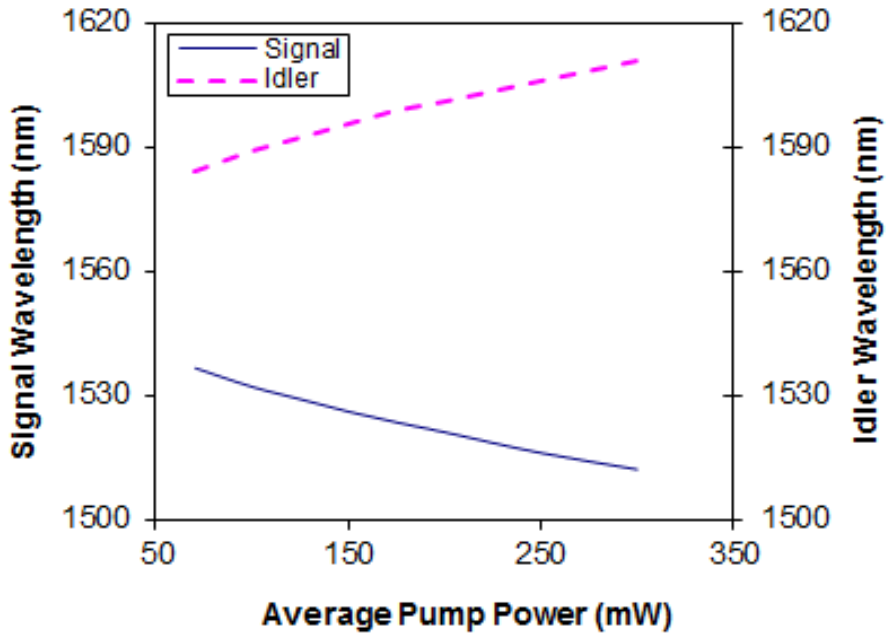
Fig. 44 Wavelength of the signal and idler photons as a function of average pump power

Below threshold spontaneous Raman photons are still generated. The probability or number of Raman (either Stokes or anti-Stokes) photons per pump pulse is calculated as[27,28]

$$R_c = P_p L N_{up} \frac{|g_R|}{A_{eff}} \frac{\sigma_u}{\sigma_p} \tag{38}$$

where

$$N_{up} = \begin{cases} n(\Omega_{up}) & when \ \Omega_{up} > 0 \\ n(\Omega_{up}) + 1 & when \ \Omega_{up} < 0 \end{cases}$$

$$n(\Omega_{ip}) = \frac{1}{\exp\left(\frac{\hbar|\Omega_{up}|}{k_B T} - 1\right)}$$

and $\Omega_{up} = \Omega_u - \Omega_p$, k_B is the Boltzmann constant, T is a temperature, g_R is the Raman gain, and $u = s, i$. Basically, the Stokes photons contaminates the idler photon where the signal is contaminated by anti-Stokes photons. The generation of Stokes and anti-Stokes photons are shown in Fig. 45. Only at very low power is the noise due to Raman photons comparable to photon pairs. As the power increases, the noise due to Raman photons is negligible in comparison to signal and idler photons.

65

7.3.2 Coincidence Generation

The quantum state of signal and idler pair generated via FWM at the output of fiber[16] can be calculated through a perturbation expansion[29] as

$$|\psi\rangle = |0\rangle + gL \sum_{k_s,k_i} F(k_s, k_i) a_{k_s}^\dagger a_{k_i}^\dagger |0\rangle + (gL)^2 \sum_{k_s,k_i,k_s',k_i'} F(k_s, k_i, k_s', k_i') a_{k_s}^\dagger a_{k_i}^\dagger a_{k_s'}^\dagger a_{k_i'}^\dagger |0\rangle + ... \quad (39)$$

where

$$F(k_s, k_i) = \frac{1}{L} \int_{-L}^{0} dz \, exp \left[i\Delta k z - \frac{(\nu_s + \nu_i)^2}{4\sigma_p^2} \right] \quad (40)$$

is the 2-photon spectral amplitude[30] and $F(k_s, k_i, k_s', k_i')$ is the 4-photon spectral amplitude. Higher order terms involving multi-photon states are relatively small and therefore can usually be neglected.[16] Here Δk is phase-mismatching, $g = \frac{\alpha_e \pi^2 \chi^{(3)} P_p}{i\epsilon_0 V_Q n^3 \lambda_p \sigma_p}$, the group velocity dispersion (GVD) in the fiber is negligible, α_e is a constant determined by experimental conditions, the wavevector $k = \frac{n(\omega)}{\omega} c$, V_Q is the quantization volume, σ_p is the bandwidth of the pump, $\omega_s = \Omega_s + \nu_s$, $\omega_i = \Omega_i + \nu_i$ and $\omega_p = \Omega_p + \nu_p$, where Ω and ν are the center angular frequencies and their corresponding detuning frequencies, respectively.

Regarding the higher-order terms of Eq. 39, the value of g in ordinary silicon fiber is $|g| = 3.468 \times 10^{-6}$ per unit length (in m) of fiber for a pump with average power of 300 mW. In 20-cm fiber, the value $|g| L$ is 6.936×10^{-7}. The values of the higher order perturbation coefficients in the quantum state shown in Eq. 39 are proportional to $(|g| L)^n$, where n=1, 2, 3... represent 1st, 2nd, 3rd and n^{th} order perturbations. Due to the small value of $|g| L$, higher orders powers can be safely neglected.

The signal photon counting probability of a photon in each pulse is given by[16]

$$S_c = \int_0^\infty dT \langle \psi | E_s^{(-)} E_s^{(+)} | \psi \rangle \quad (41)$$

where the electric field operator is

$$E_s^{(+)} = \sum_{k_s} \sqrt{\frac{cA_{eff}}{4V_Q}} \, a_{k_s} e^{-i\omega_s t} \, e^{-\frac{(\omega_s - \Omega_s)^2}{2\sigma_s^2}} \quad (42)$$

where σ_s is the bandwidth of the signal pulse, a_{k_s} is an annihilation operator of a photon with momentum k_s.

After simplification Eq. 41 at perfect phase-matching condition, $\Delta k = 0$, becomes

$$S_c = A \left(\gamma\, P_p\, L \right)^2 \frac{\sigma_s}{\sigma_p} \tag{43}$$

where $A = \frac{\alpha_e^2\, \pi\, n\, A_{eff}^3}{18\sqrt{2}\, V_Q^2}$. Similarly, the idler photon counting probability of a photon in each pulse can be calculated as

$$I_c = A \left(\gamma\, P_p\, L \right)^2 \frac{\sigma_i}{\sigma_p} \tag{44}$$

where σ_i is the bandwidth of generated idler pulse.

Here, the nonlinear coefficient of the refractive index is $n_2 = 3.4 \times 10^{-20} m^2/W$. For a 1560-nm optical fiber, $A_{eff} = 76.94\ \mu m^2$ and the value of γ becomes $1.7904 \times 10^{-9} \mu m^{-1} W^{-1}$. The parameters α_e and V_Q are given by $\alpha_e = 0.237$ and $V_Q = 1.6 \times 10^{-16}\ m^3$.[16] Equations 43 and 44 show that the number of signal and idler photons generated from a pulse increases with the pump power. This result is shown in Fig. 45.
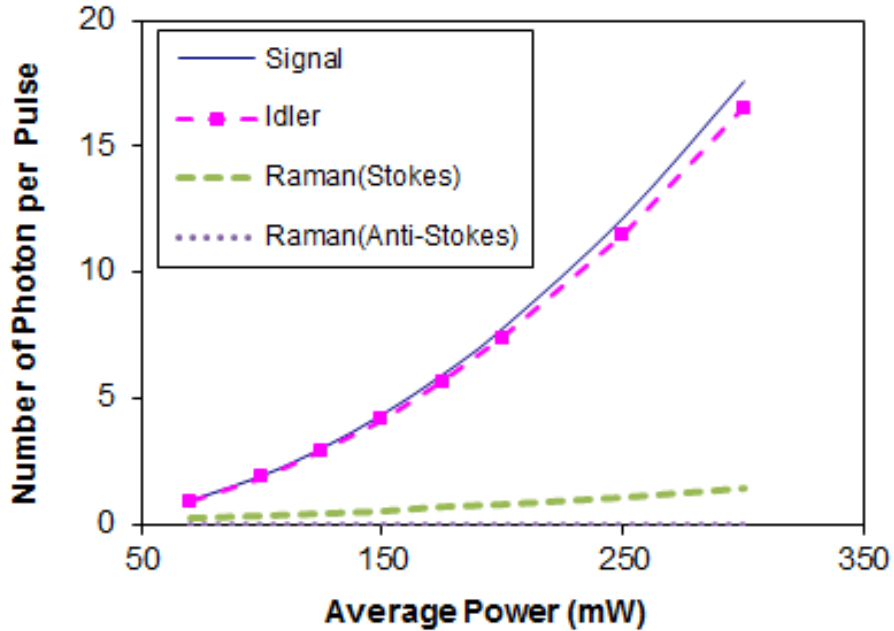

Fig. 45 Number of generated signal, idler, and Raman (Stokes and anti-Stokes at T=20 K) photons per pulse as a function of the average pump power

The probability of a coincidence from each pulse, assuming no loss and 100% detection

efficiency, can be written as[16]

$$CC = \int_0^\infty dT_1 \int_0^\infty dT_2 \langle\psi|E_1^{(-)}E_2^{(-)}E_2^{(+)}E_1^{(+)}|\psi\rangle \tag{45}$$

where the fields at the output fiber measured by the detector 1 and detector 2 are given by

$$E_1^{(+)} = \sum_{k_1} \sqrt{\frac{cA_{eff}}{4V_Q}}\, a_{k_1} e^{-i\omega_s t_1}\, e^{-\frac{(\omega_s - \Omega_s)^2}{2\sigma_s^2}} \tag{46}$$

and

$$E_2^{(+)} = \sum_{k_2} \sqrt{\frac{cA_{eff}}{4V_Q}}\, a_{k_2} e^{-i\omega_i t_2}\, e^{-\frac{(\omega_i - \Omega_i)^2}{2\sigma_i^2}} \tag{47}$$

Here, $t_m = T_m - l_m/c$ is the time at the output tip of the fiber and l_m is the optical path length from output tip of the fiber to the detectors, $m = 1, 2$ and T_m is the registration time at m^{th} detector. Now the integrand in Eq. 45 can be rewritten as

$$\langle\psi|E_1^{(-)}E_2^{(-)}E_2^{(+)}E_1^{(+)}|\psi\rangle = |\langle 0|E_2^{(+)}E_1^{(+)}|\psi\rangle|^2 \tag{48}$$

Since $\langle 0|E_2^{(+)}E_1^{(+)}|\psi\rangle \propto \langle 0|a_{k_2}a_{k_1}a_{k_s}^\dagger a_{k_i}^\dagger|0\rangle$, this (integrand) term only exists at $k_1 = k_s$ and $k_2 = k_i$ (see Chen et al,[16] p. 5). Using the 2-photon state in Eq. 39 and the fields defined in Eqs. 46 and 47, the 2-photon amplitude, Eq. 48 can be written as

$$\langle 0|E_2^{(+)}E_1^{(+)}|\psi\rangle = \frac{cA_{eff}}{4V_Q} \sum_{k_s,k_i} F(k_s, k_i) e^{-i(\omega_s t_1 + \omega_i t_2)} \times e^{-\frac{\nu_s^2 + \nu_i^2}{2\sigma_i^2}} \tag{49}$$

where $\sigma_s = \sigma_i$ is considered for this case.

After simplification, the probability of a coincidence from each pulse (without any Raman noise) (i.e., Eq. 45 at the condition of $\Delta k = 0$) becomes

$$CC = B(\gamma P_p L)^2 \frac{\sigma_i^2}{\sigma_p \sqrt{\sigma_p^2 + \sigma_i^2}} = B(\gamma P_p L)^2 \frac{1}{\frac{\sigma_p}{\sigma_i}\sqrt{\left(\frac{\sigma_p}{\sigma_i}\right)^2 + 1}} \tag{50}$$

where $B = \frac{\alpha_e^2 \pi n^2 A_{eff}^4}{144\, V_Q^{8/3}}$. Note that in Eq. 50 the CC scale quadratically with the pump power through the term $(\gamma P_p L)^2$.[16]

For our proposed experiment, the phase modulation term γP_p plays a major role in phase matching. In our proposal, the colors are chosen in a way where the phase introduced

68

by this modulation term is mostly compensated such that the phase introduced by this term would be much less than $\frac{\pi}{2}$. Then this introduced phased causes pulse broadening, which means all pump, signal, and idler bandwidths would be increasing according to their wavelengths.[28] The ratios of the bandwidths of idler or signal and pump remain the same as that without pulse broadening. Since both single counts and coincidences depend on the ratio of the bandwidths of idler or signal and pump, singles counts and coincidences would be largely unaffected by pulse broadening. Furthermore, because our proposed experiment would use a short (20 cm) non-polarization maintaining fiber to generate entangled photons the asymmetric spectral reshaping of the type measured in the experiment by Fang et al.[18] would be avoided. We anticipate insignificant changes caused by spectral reshaping to the quality of entanglement for our proposal.

The Raman noise also contaminates the coincidence counts, where the observed coincidence counts (CC_{obs}) can be written as

$$CC_{obs} = CC + CC_{acc} \tag{51}$$

and the accidental coincidence CC_{acc} can be written as $CC_{acc} = CC_{StAs} + CC_{sSt} + CC_{iAs}$. CC_{StAs} are coincidences between Stokes and anti-Stokes photons, CC_{sSt} the coincidences between signal and Stokes photons, and CC_{iAs} are coincidences between idler and anti-Stokes photons. At higher powers as shown in Fig. 46 the predicted coincidences and accidental coincidences may include contributions from higher-order correlated or entangled photon states.

The dependence of Raman noise on temperature is given by Eq. 38. Cooling the Sagnac fiber loop components is one method that can be used to reduce the number of accident coincidences caused by Raman noise to well below the true coincidence counts (Fig. 46). There are several potential options to cool the Sagnac fiber loop. Using a helium-based cryostat can cool from 1 to 5 K while hydrogen-based or closed-cycle cryostats can cool to 20 K. Tittel et al.[31] were successful in cooling fibers to 1 K.

7.4 Conclusions

In conclusion, our analysis indicates that polarization entangled photon pairs can be generated in an optical fiber by a FWM process. The key feature of this entangled photon source is the controllable generation of specified signal and idler colors (wavelengths). In this case,
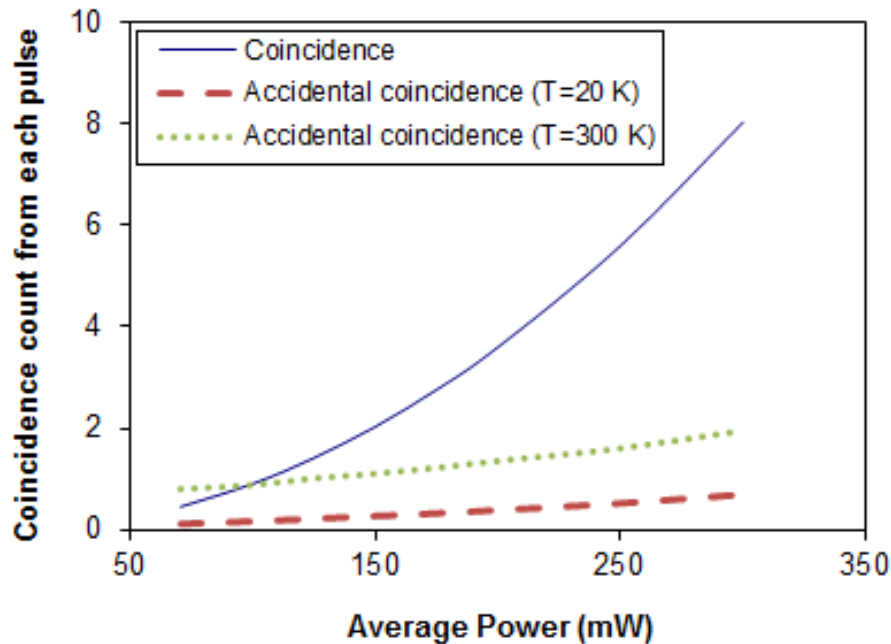
Fig. 46 Assuming no loss and 100% detection efficiency the number of generated coincidences in each pulse is shown as a function of the average pump power. Accidental coincidences are shown for 20 and 300 K for comparison.

the color (wavelength) selections may be accomplished by varying the pump power. Another important quality of this source is its feature of very low Raman noise photon pair generation. These kinds of color-controllable entangled photon pairs would be useful in certain applications for quantum communications, quantum computing, and quantum imaging. In particular, we expect that this single spatial mode source will be useful for fundamental studies investigating real-time quantum imaging of entanglement such as by extending the single wavelength experiment of Fickler et al.[32] to include the controllable generation of specified signal and idler wavelength entangled photons.

7.5   References

1.   Pittman, TB, Shih, YH, Strekalov, DV, Sergienko, AV. Optical imaging by means of two-photon quantum entanglement. Physical Review A. 1995; 52, R3429.

2.   Meyers, RE, Deacon, KS, Shih, Y. Ghost-imaging experiment by measuring reflected photons. Physical Review A. 2008; 77, 041801.

70

3. Meyers, RE, Deacon, KS, Shih, Y. A new two-photon ghost imaging experiment with distortion study. Journal of Modern Optics. 2007; 54:16, 2381–2392.

4. Meyers, RE, Deacon, KS, Shih, Y. Turbulence-free ghost imaging. Applied Physics Letters. 2011; 98, 111115.

5. Karmakar, S, Shih, Y. Two-color ghost imaging with enhanced angular resolving power. Physical Review A. 2010; 81, 033845.

6. Karmakar, S, Meyers, RE, Shih, Y. Noninvasive high resolving power entangled photon quantum microscope. Journal of Biomedical Optics. 2015; 20:1, 016008.

7. Raussendorf, R, Briegel, HJ. A one-way quantum computer. Physical Review Letters. 2001; 86, 5188.

8. Nielsen, MA,Chuang, IL. Quantum Computation and Quantum Information. Cambridge (UK): Cambridge University Press; 2002.

9. Bennett, CH, Brassard, G, Crepeau, C, Jozsa, R, Peres, A, Wootters, WK. Teleporting an unknown quantum state via dual classical and Einstein-Podolsky-Rosen channels. Physical Review Letters. 1993; 70, 1895.

10. Ma, X-S, Kropatschek, S, Naylor, W, Scheidl, T, Kofler, J, Herbst, T., Zeilinger, A, Ursin, R. Experimental quantum teleportation over a high-loss free-space channel. Optics Express. 2012; 20, 23126.

11. Burnham, DC, Weinberg, DL. Observation of simultaneity in parametric production of optical photon pairs. Physical Review Letters. 1970; 25, 84.

12. Shih, YH, Alley, CO. New type of Einstein-Podolsky-Rosen-Bohm experiment using pairs of light quanta produced by optical parametric down conversion. Physical Review Letters. 1988; 61, 2921.

13. Hong, CK, Ou, ZY, Mandel, L. Measurement of subpicosecond time intervals between two photons by interference. Physical Review Letters. 1987; 59, 2044.

14. Banaszek, K, U'Ren, AB, Walmsley, IA. Generation of correlated photons in controlled spatial modes by downconversion in nonlinear waveguides. Optics Letters. 2001; 26, 1367.

15.	Tanzilli, S, deRiedmatten, H, Tittel, H, Zbinden, H, Baldi, P, Micheli, MD, Ostrowsky, D, Gisin, N. Highly efficient photon-pair source using periodically poled lithium niobate waveguide. Electronics Letters. 2001; 73, 26.

16.	Chen, J, Li, X, Kumar, P. Two-photon-state generation via four-wave mixing in optical fibers. Physical Review A. 2005; 72, 033801.

17.	Smith, BJ, Mahou, P, Cohen, O, Lundeen, JS, Walmsley, IA. Photon pair generation in birefringent optical fibers. Optics Express. 2009; 17, 23589.

18.	Fang, B, Cohen, O, Lorenz, VO. Polarization-entangled photon-pair generation in commercial-grade polarization-maintaining fiber. Journal of the Optical Society of America B. 2014; 31, 277.

19.	Li, X, Voss, PL, Sharping, JE, Kumar, P. Optical-fiber source of polarization-entangled photons in the 1550 nm telecom band. Physical Review Letters. 2005; 94, 053601.

20.	Sharping, JE, Fiorentino, M, Kumar, P. Observation of twin-beam-type quantum correlation in optical fiber. Optics Letters. 2001; 26, 367–369.

21.	Takesue, H, Inoue, K. Generation of polarization-entangled photon pairs and violation of Bell's inequality using spontaneous four-wave mixing in a fiber loop. Physical Review A. 2004; 70, 031802R.

22.	Karmakar, S, Meyers, RE. Color controllable polarization entanglement generation in optical fiber at telecommunication wavelengths. Optics Express. 2015; 23:16, 20605–20616.

23.	Garay-Palmett, K, McGuinness, HJ, Cohen, O, Lundeen, JS, Rangel-Rojo, R, U'Ren, AB, Raymer, MG, McKinstrie, CJ, Radic, S, Walmsley, IA. Photon pair-state preparation with tailored spectral properties by spontaneous four-wave mixing in photonic-crystal fiber. Optics Express. 2007; 15, 14870.

24.	Ghosh, G. Dispersion-equation coefficients for the refractive index and birefringence of calcite and quartz crystals. Optics Communications. 1999; 163, 95.

25.	Stolen, RH, Lee, C, Jain, RK. Development of the stimulated Raman spectrum in single-mode silica fibers. Journal of the Optical Society of America B. 1984; 1, 652.

26.   Smith, RG. Optical power handling capacity of low loss optical fibers as determined by stimulated Raman and brillouin scattering. Applied Optics. 1972; 11, 2489.

27.   Lin, Q, Yaman, F, Agarwal, GP. Photon-pair generation in optical fibers through four-wave mixing: Role of Raman scattering and pump polarization. Physical Review A. 2007; 75, 023803.

28.   Agarwal, GP. Nonlinear Fiber Optics. Boston (MA): Academic Press; 1989.

29.   Sakurai, JJ, Napolitano, J. Modern Quantum Mechanics. Boston (MA): Addison Wesley; 2011. pp 356.

30.   Keller, TE, Rubin, MH. Theory of two-photon entanglement for spontaneous parametric down-conversion driven by a narrow pump pulse. Physical Review A. 1997; 56, 1534-1541.

31.   Saglamyurek, E, Jin, J, Verma, VB, Shaw, MD, Marsili, F, Nam, SW, Oblak, D, Tittel, W. Quantum storage of entangled telecom-wavelength photons in an erbium-doped optical fibre. Nature Photonics. 2015; 9, 83.

32.   Fickler, R, Krenn, M, Lapkiewicz, R, Ramelow, S, Zeilinger, A. Real-time imaging of quantum entanglement. Nature: Scientific Reports. 2013; 3, 1914.

8. Study on Environmental Effects on Polarized Light Fiber Distribution

Authors: Ronald Meyers, Keith Deacon, Sanjit Karmakar, Arnold Tunick

8.1 Introduction

This section analyzes the environmental effects on the transmission of polarized light through our 27-km round trip optical fibers between ARL and JQI. Measurements of the light transmission were made with an optical time-domain reflectometer (OTDR) at 1310 and 1550 nm and are shown in Figs. 47 and 48. Subsequently, polarization measurements were performed from our laboratory using a setup built and operated by SEDD. Data were obtained on the ambient temperature in the area. A model was made based on light scattering by phase screens to assess the impact that ambient temperature would have on the polarization change in light transiting the 27-km fiber loop. The model and results are given below. The analysis clearly shows that a few degrees of temperature variation can cause the effects on observed polarization change. In addition, to allow for future joint experiments we implemented a CISD to SEDD quantum channel, 6-strand fiber link (300 m) as depicted in Figs. 49, 50 and 51.
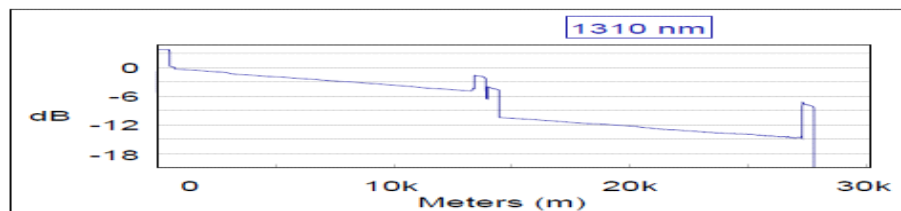

**Fig. 47 The 1310-nm, 6 dB loss, 1-way (-14 dB, roundtrip) ARL-JQI**
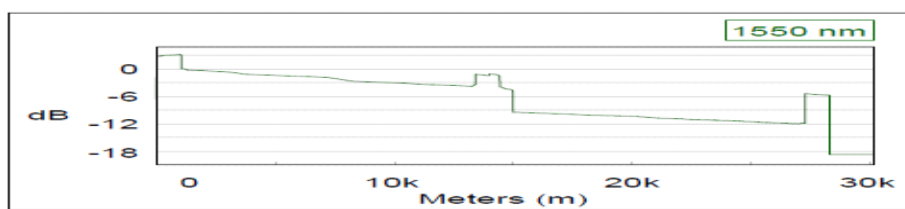
Fig. 48 The 1550-nm, 4 dB loss, 1-way (-12 dB, roundtrip) ARL-JQI

74
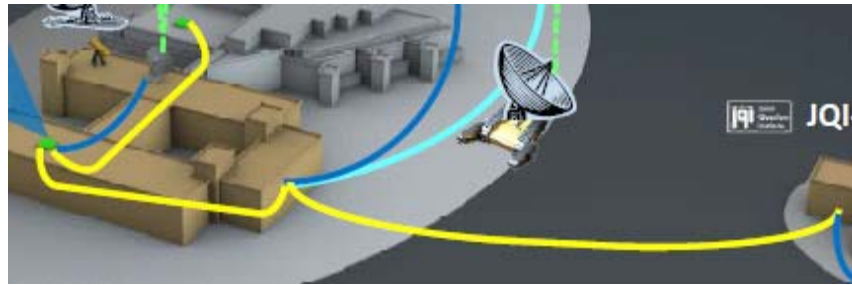
Fig. 49 Six-strand fiber link enables quantum communications experiments between CISD and SEDD labs
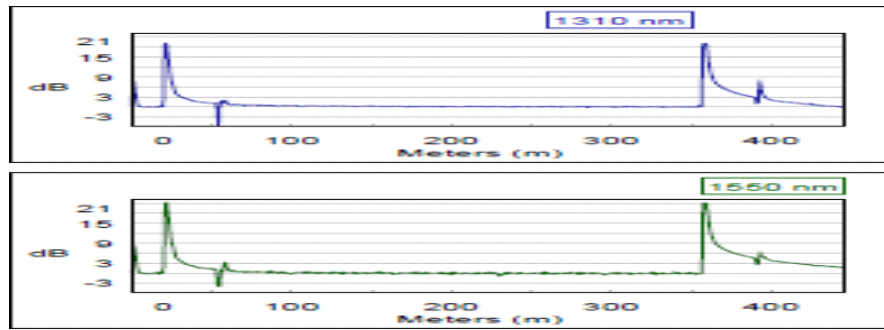

Fig. 50 A 5-ns pulse OTDR, 1310-nm, 0.03 db loss, and 1510 nm, 0.06 db loss

8.2 Background on Environment Effects on the Polarization over a Fiber

Ambient temperature and light can affect the transmission of quantum information over fiber and free-space paths. The transmission of quantum information, unlike the transmission of classical information, involves relatively few photons so their absorption or transformation can cause significant adverse effects. In this study, we analyze the potential for temperature to impact transmission of polarized light over a multi-kilometer path.

Long-distance entanglement distribution over free-space has been demonstrated at night to avoid the daytime background light from the sun.[1–5] By using spectral, spatial, and temporal filtering techniques, Peloso et al.[6] were able to produce distant entanglement distribution over several days under varying light and weather conditions.

When optical fiber is used as a quantum channel to transmit quantum information, background noise due to daylight is not typically a problem, although it is important to use the appropriate fiber-optic cables for outdoor transmission. It has been reported that the Japanese fiber-optic network, which runs partially over ground is susceptible to daylight degradation of their quantum signal due to sunlight penetration through the fiber. Nevertheless, to avoid background noise, outdoor fiber-optic cables are often jacketed with a

75
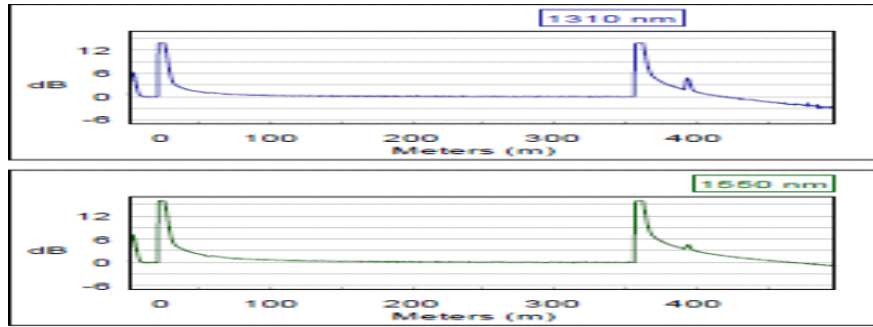
Fig. 51 A 10μs pulse OTDR 1310-nm, 0.04-dB loss, and 1510-nm, 0.04-dB loss

polyethylene black color jacket. Polyethylene has excellent moisture and weather resistance features and the black color helps to reduce the background noise to low levels.

Cohen et. al.[7] has studied the effects of changes in temperature in the environment on fiber-optic cables with variations from -40 to 67 °C. They found that the loss in light transmission through optical fiber does not change significantly due to changes in temperature in the environment and also the dispersion in lower bit rate transmission is not significantly affected by temperature changes.[7–10]

Yet, when the transmission through optical fiber occurs only in the laboratory, the rate of change of temperature is low. As a result, the transmission of quantum properties in optical fiber in the laboratory is not greatly affected. But when the transmission of quantum properties takes place in optical fiber that is affected by the outdoor environment (i.e., where the temperature changes can be significant), then the information carried by the photons can lose its quantum properties easily during propagation, for example, its polarization properties. In this section, we report on the effect on the polarization property of photons in fiber due to the change of temperature in environment.

8.3 Environmental Effect on State of Polarization

Let us consider an electromagnetic wave with field intensity vector $\vec{E}$ that propagates in the direction of z axis. This field intensity vector can be represented by 2 orthogonal field $\vec{E}_x$ and $\vec{E}_y$ as

$$\vec{E} = \vec{E}_x + \vec{E}_y \tag{52}$$

where xyz is an orthogonal coordinate system. The field intensities $\vec{E}_x$ and $\vec{E}_y$ are defined

76

by

$$E_x = E_{0x} \, cos(kz - \omega t + \phi_x) \tag{53}$$

$$E_y = E_{0y} \, cos(kz - \omega t + \phi_y) \tag{54}$$

where E_{0x} and E_{0y} are wave amplitudes, ω is the angular frequency, k is the magnitude of wavevector, t is the time, and ϕ_x and ϕ_y are the phases of the wave. Now we consider a linearly polarized wave as an initial state where $E_{0x} = E_{0y}$ and $\phi = \phi_x - \phi_y = 0$.

Due to imperfections in optical fibers, 2 polarizations will travel at different speeds. These imperfections causes birefringence (i.e., introduces additional phase changes in polarization modes). This additional phase change determines output state of the polarization.[11–13] Basically, these imperfections are categorized as 1) imperfection due to slightly elliptical core and 2) imperfection due to asymmetry in thermal stress.

The birefringence due to elliptical core is defined as[14,15]

$$B_e = \frac{e^2 (2\delta)^{3/2}}{r} \frac{4}{V^3} \frac{(lnV)^3}{1 + lnV} \tag{55}$$

where $\delta = n_{core} - n_{cladding}$ is the difference of refractive between core and cladding, r is the radius of the fiber core, and e is the ellipticity that is defined as $e^2 = 1 - \frac{b^2}{a^2}$ with a and b are the semi-major and semi-minor axes of the ellipse. The parameter V is defined as $V = k_0 \, r \, \sqrt{n_{core}^2 - n_{cladding}^2}$ with $k_0 = \frac{2\pi}{\lambda_0}$ is the free-space propagation constant.[16]

The change of temperature also causes birefringence in the fiber and this can be expressed as[14,15]

$$B_T = k_0 \left[1 - \frac{U^2}{V^2} \right] \left[\frac{1}{2} n_T^3 \frac{\Delta\alpha\Delta T}{1 - \nu^2} \frac{a - b}{a + b} (p_{11} - p_{12}) \right] \tag{56}$$

where p_{11} and p_{12} are the components of the strain-optical tensor of the fiber material, ν is the Poisson's ratio of the fiber core, $\Delta\alpha$ is the difference of coefficients of the thermal expansion in the core and cladding of the fiber, ΔT is the temperature difference of the glass softening temperature and the environmental temperature, and $U = r \, \sqrt{k_0^2 n_{core}^2 - \beta_0^2}$ with β_0 is the propagation with circular core. The temperature dependent refractive index n_T of fiber is given by

$$n_T = n_R + (T - R) \left(\frac{\delta n}{\delta T} \right) \tag{57}$$

where R and T represent room temperature and environmental temperature, respectively.

$\left(\frac{\delta n}{\delta T}\right)$ is the thermo-optic coefficient of the fiber material. The total birefringence is given by

$$B = B_e + B_T \qquad (58)$$

and the introduced phase difference due to birefringence is

$$\phi = B\,L \qquad (59)$$

where L is length of the fiber.

The variation of total birefringence with temperature is shown in Fig. 52. For this case, the values of parameters are $\Delta\alpha = 3.5 \times 10^{-7}\,°C^{-1}$, $\Delta T = (T - 1065)\,°C$, $\nu = 0.166$, $p_{11} = 0.126$, $p_{12} = 0.26$, $r = 4.1\,\mu$m, $e = 0.2$, $n_{cladding} = 1.44402$, $n_{core} = 1.44924$, $\lambda_0 = 1.324\mu$m, $(\delta n/\delta T) = 10^{-5}\,°C^{-1}$ and $U << V$.
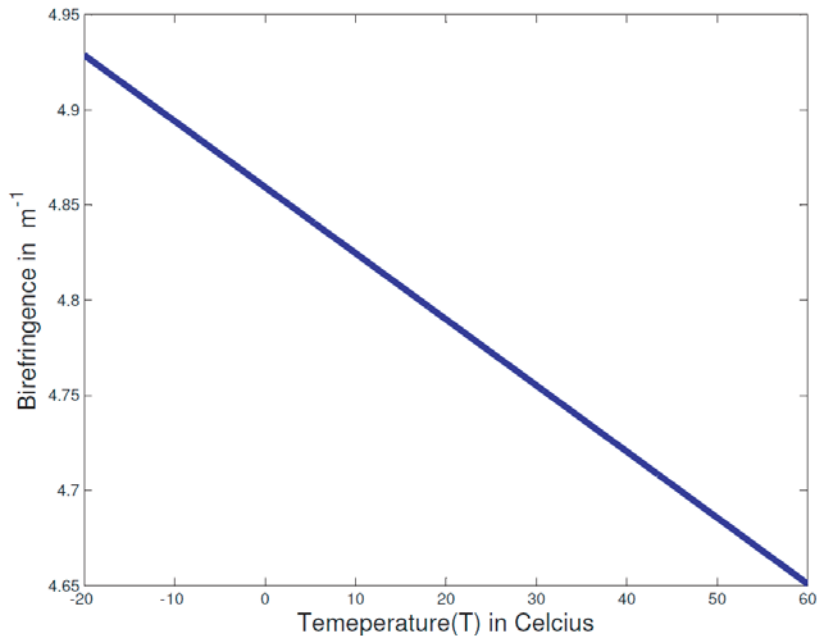

Fig. 52 Variation of birefringence in fiber with an environmental change of temperature

Since the environmental effect on an optical fiber causes random changes in birefringence, it is reasonable to treat it as a randomly rotating wave-plate. The randomly rotating wave-plate

78

is represented by a Mueller matrix[16] and it is given below as

$$M = \begin{vmatrix} 1 & 0 & 0 & 0 \\ 0 & \cos^2 2\theta + \sin^2 2\theta \cos\phi & \cos 2\theta \sin 2\theta (1 - \cos\phi) & \sin 2\theta \sin\phi \\ 0 & \cos 2\theta \sin 2\theta (1 - \cos\phi) & \sin^2 2\theta + \cos^2 2\theta \cos\phi & -\cos 2\theta \sin\phi \\ 0 & -\sin 2\theta \sin\phi & \cos 2\theta \sin\phi & \cos\phi \end{vmatrix} \quad (60)$$

where θ is the angle between fast axis and the horizontal axis of the reference system and ϕ is the total phase shift between 2 polarization mode. Let us now consider the case of a fast axis as the horizontal axis (i.e., $\theta = 0$), then the Muller matrix becomes

$$M = \begin{vmatrix} 1 & 0 & 0 & 0 \\ 0 & 1 & 0 & 0 \\ 0 & 0 & \cos\phi & -\sin\phi \\ 0 & 0 & \sin\phi & \cos\phi \end{vmatrix}. \quad (61)$$

The polarization of light in a system is expressed as

$$\vec{S}_o = M \vec{S}_i \quad (62)$$

where $\vec{S}_0$ and $\vec{S}_i$ are the input and output stokes vectors determined the input and out states of polarizations, respectively. Consider the input state as linearly polarized with an angle of 45°. Then the stokes parameter for input case is given by

$$\vec{S}_i = \begin{pmatrix} 1 \\ 0 \\ 1 \\ 0 \end{pmatrix}. \quad (63)$$

Now we consider the fiber is divided into N number of wave-plate with contributing the phase-difference of ϕ_1, ϕ_2, ϕ_3,.....,ϕ_N. Then the output stokes vector after 1 wave-plate becomes

$$\vec{S}_{01} = \begin{pmatrix} 1 \\ 0 \\ \cos\phi_1 \\ \sin\phi_1 \end{pmatrix}. \quad (64)$$

This output Stokes vector is the input vector for the second wave-plate. Now the output

Stokes vector after the second wave-plate is

$$\vec{S}_{02} = \begin{pmatrix} 1 \\ 0 \\ \cos(\phi_1 + \phi_2) \\ \sin(\phi_1 + \phi_2) \end{pmatrix}. \tag{65}$$

similarly, it is calculated that the output Stokes vector after the N th wave-plate is

$$\vec{S}_{02} = \begin{pmatrix} 1 \\ 0 \\ \cos(\phi_1 + \phi_2 + ... + \phi_N) \\ \sin(\phi_1 + \phi_2 + ... + \phi_N) \end{pmatrix}. \tag{66}$$

Now one can say that the angle between the input and output states of polarization (α) is $cos\alpha = cos(\phi_1 + \phi_2 + ... + \phi_N)$, that is,

$$\alpha = \phi_1 + \phi_2 + ... + \phi_N. \tag{67}$$

A communication system connected through single mode fiber is considered where the distance between departure station and receiver station is 26 km. Here we divide this distance into 5 sections: 1) the fiber inside the departure station, 2) the room in a different temperature, 3) the fiber in outdoor ambient temperature, 4) the room in different temperature, and 5) the fiber inside the receiver station. Each section consists of several numbers of randomly rotating wave-plates. The outdoor temperature variations during this experiment are shown in Fig. 53.

The temperature inside both the departure and receiver stations are almost constant. But the outdoor temperatures change with time. In Fig. 52, it is shown that the birefringence decreases by an amount of $0.0035/m$ with an increment of temperature of $1\ ^\circ C$. When we consider several numbers of wave-plates, the calculated total change of the phase difference between 2 polarization modes (using Eq. 59) and Eq. 67 can explain the measured result shown in Fig. 54.
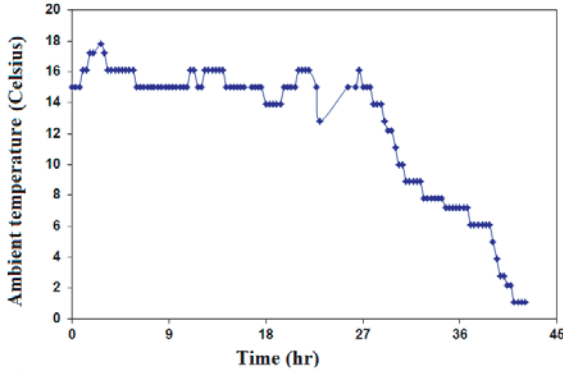
**Fig. 53 Ambient temperature variation as function of time in hours**
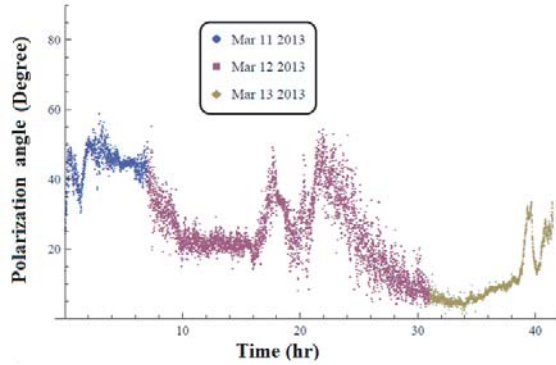
Fig. 54 Measured output polarization angle at the end of a fiber as function of time in hours

Because the temperature inside the departure and receiver stations and rooms at different temperatures do not vary with time, we only consider the temperature variations of the outdoor fiber-optic cable. Let us consider the outdoor cable is 25 km, where it is a combination of 1000 parts (i.e., $N = 1000$ and each part has a length of 25 m). Even though the outdoor cable is underground, there is still a slow temperature variation with time and position. Due to temperature variations in position, each 25-m part contributes a phase retardation either positively or negatively. Because of a large number of wave-plates, there is a high chance of total positive phase contribution canceling with total negative phase contribution. Alternately, there is a chance that they do not completely cancel with each other. Hence, this will contribute to a phase retardation which depends on the temperature variation with time, which will degrade the quality of the propagation of polarized light in the optical fiber. This result is shown in Table 5.

81
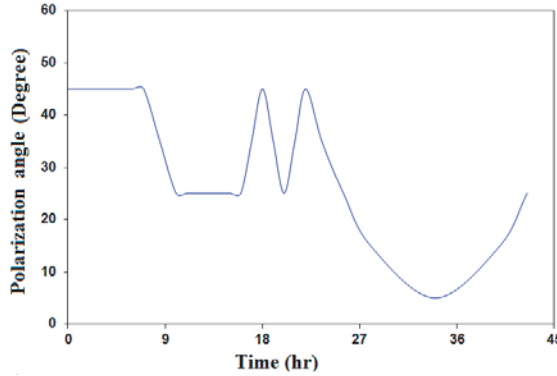
Fig. 55 Theoretical output polarization angle at the end of a fiber as function of time in hours

Table 5. Quality of the propagation of polarized light in the optical fiber

Time (h)	Temperature Variation	$\dfrac{Phase}{contribution(deg)}$	$\dfrac{Polarization}{angle\ (deg)}$
0-7	$\dfrac{500\ parts\ \Delta T'=+1°C}{500\ parts\ \Delta T'=-1°C}$	0	45
8.5	$\dfrac{501\ parts\ \Delta T'=+1°C}{499\ parts\ \Delta T'=-1°C}$	-10	35
10-16	$\dfrac{502\ parts\ \Delta T'=+1°C}{498\ parts\ \Delta T'=-1°C}$	-20	25
17	$\dfrac{501\ parts\ \Delta T'=+1°C}{499\ parts\ \Delta T'=-1°C}$	-10	35
18	$\dfrac{500\ parts\ \Delta T'=+1°C}{500\ parts\ \Delta T'=-1°C}$	0	45
19	$\dfrac{501\ parts\ \Delta T'=+1°C}{499\ parts\ \Delta T'=-1°C}$	-10	35
20	$\dfrac{502\ parts\ \Delta T'=+1°C}{498\ parts\ \Delta T'=-1°C}$	-20	25
21	$\dfrac{501\ parts\ \Delta T'=+1°C}{499\ parts\ \Delta T'=-1°C}$	-10	35
22	$\dfrac{500\ parts\ \Delta T'=+1°C}{500\ parts\ \Delta T'=-1°C}$	0	45
23.5	$\dfrac{501\ parts\ \Delta T'=+1°C}{499\ parts\ \Delta T'=-1°C}$	-10	35
25.5	$\dfrac{502\ parts\ \Delta T'=+1°C}{498\ parts\ \Delta T'=-1°C}$	-20	25
28	$\dfrac{503\ parts\ \Delta T'=+1°C}{497\ parts\ \Delta T'=-1°C}$	-30	15
34	$\dfrac{502\ parts\ \Delta T'=+1°C}{498\ parts\ \Delta T'=-1°C}$	-40	5
40	$\dfrac{501\ parts\ \Delta T'=+3°C}{499\ parts\ \Delta T'=-3°C}$	-30	15
42.5	$\dfrac{501\ parts\ \Delta T'=+2°C}{499\ parts\ \Delta T'=-2°C}$	-20	25

82

Considering this model and using Eqs. (59) and (67), the variation of the polarization angle with time at the output end of fiber is shown in Fig. 55. This predicted result agrees well with the experimental results shown in Fig. 54.

8.4   Conclusion

The main problem addressed in this section with regard to keeping the state of polarization of the input state the same as the state at the output of the fiber is the temperature fluctuation, even though the fluctuations are small. Since the outdoor fiber is underground, temperature variations in the fiber are slower in comparison with the environmental outdoor temperature changes. Yet, small temperature changes are enough to significantly affect the polarization property of the propagating photons. Basically, the temperature fluctuations cause birefringence in the optical fiber, which results in a phase difference between two polarization modes. This degrades the state of output polarization and also makes the quantum state of the photon unstable.

Figure 54 shows the measured experimental result of the output state of polarization after propagating 26 km through optical fiber as function of the time of day. In contrast, the predicted theoretical result of the output state of polarization for the same experimental conditions as function of the time of day is shown in Fig. 55. Both of these results agree well with each other. Now one can say that the angle between the input and output states of polarization (α) is $cos\,(\alpha) = cos(\phi_1 + \phi_2 + ... + \phi_N)$, that is,

$$\alpha = \phi_1 + \phi_2 + ... + \phi_N. \tag{68}$$

8.5   References

1.   Ling, A, et al. Physical Review A. 2008; 78, 020301.

2.   Peng, CZ, et al. Physical Review Letters. 2005; 94, 150501.

3.   Ursin, R, et al. Nature Physics. 2007; 3, 481.

4.   Marcikic, I, et al. Applied Physics Letters. 2006; 89, 101122.

5.   Erven, C, et al. Optics Express. 2008; 16, 16840.

6.   Peloso, MP, et al. arXiv:0812.1880v1;2008.

7.   Cohen, LG, et al. The Bell System Technical Journal. 1979; 58, 945.

8.   Andre, PS, et al. Journal of Microwave and Optoelectronics. 2005; 3, 65.

9.   Kato, T, et al. Optics Letters. 2000; 25, 1156.

10.   Hatton, WH, et al. Journal of Lightwave Technology. 1986; LT-4, 1552.

11.   Agarwal, GP. Nonlinear Fiber Optics. Boston (MA): Academic Press; 1989.

12.   Saleh, B, Teich, M. Fundamentals of Photonics. New York (NY): John Wiley & Sons;1991.

13.   Sundoy, PR. Depolarization of orthogonal states of polarization in fiber optics high speed transmission [PhD thesis]. [Trondheim (Norway)]: Norwegian University of Science and Technology; 2004.

14.   Gupta, D, et al. Optics Communications. 2006; 263, 36.

15.   Boudrioua, N, et al. Optics Communications. 2008; 281, 4870.

16.   Perlicki, K. Optical and Quantum Electronics. 2005; 37, 1141.

9. SEDD

Authors and Major Contributors: Daniel Stack, Patricia Lee, Qudsia Quraishi

This section describes some of the progress of the QNET-AP DSI project conducted primarily by the SEDD quantum team. In the following we describe research toward 1) building the atomic memory and 2) testing the polarization stability of the ARL to JQI to ARL fiber-optic line, which will be used to carry the photon "flying qbits" that will entangle the distant atomic memories. Schematics of the atom trap and QNET-AP setup are shown in Figs. 56 and 57. The research also includes development of a photon frequency filter for the atomic memory that will help exclude photons at the wrong frequencies.
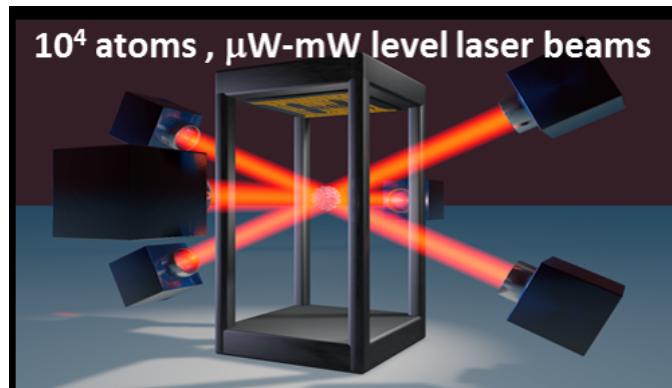

Fig. 56 Atom trap schematic
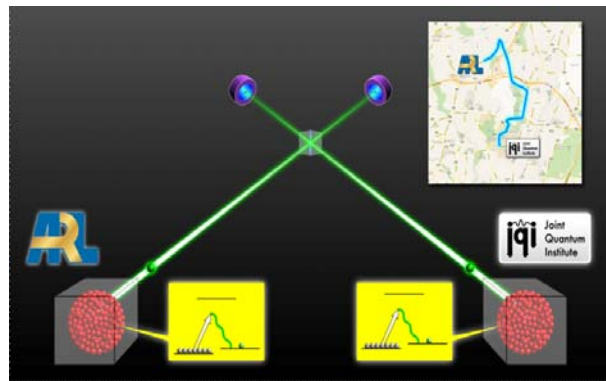
Fig. 57 Schematic of the QNET-AP setup

9.1 Primary Components and Tasks

The key components that need to considered are the fiber connection between ARL and JQI and the distant atomic memories that can be entangled with photons. The atomic memories using Rb read and write photons in the 795-nm range. However, these would be absorbed by the fiber-optic line before traveling the 13.5 km needed. Our strategy is to convert single photons from 795 nm to telecom wavelengths at 1324 nm that are not readily absorbed by the optical fiber. Since ARL/JQI fiber already in place, we began by testing the polarization change of photons from a 1324-nm laser going 27 km over the round trip. We also built a laser-cooled atomic quantum system. To verify the non-classical properties of the quantum memory, we demonstrated quantum correlations of photons emitted by laser-cooled atoms.

9.1.1 Measurement of ARL/JQI Fiber Polarization Stability

SEDD designed an experiment to measure the polarization stability of light propagating the 27-km fiber loop shown in Fig. 8 in Section 5. The experimental design used a 1324-nm laser with beam splitters and wave-plates to measure the polarization drift as shown in Fig. 58. A short time sample of the measured data is presented in Fig. 59. Even on short time scales, roughly 3 min, the polarization variability can be $10°$ of polarization or larger. A longer (24 h) sample of the data is shown in Fig. 60. It is important to note that there are large variations of the polarization over time scales of hours in these data. In summary, the polarization stability was measured, and it was determined that it could be made sufficiently stable with feedback control. The project is currently working to establish this feedback control.
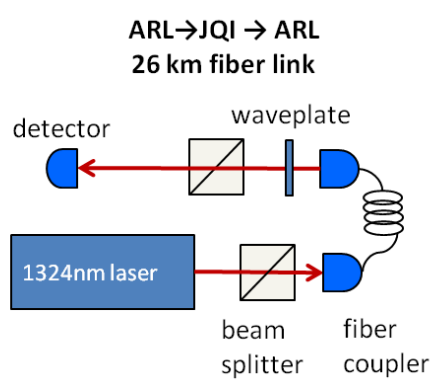

Fig. 58 Polarization stability experimental layout

86
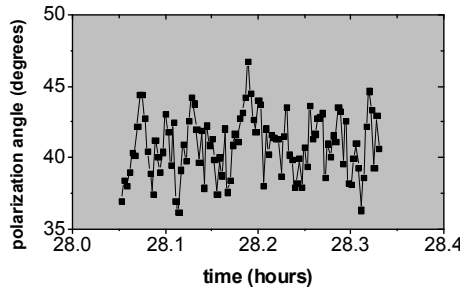
Fig. 59 Measurements Day 2
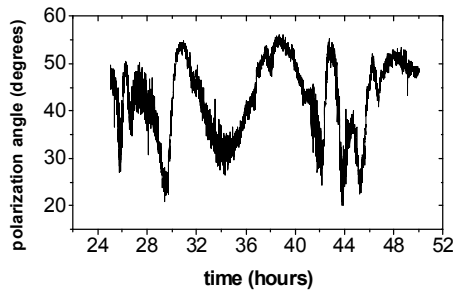
Fig. 60 Approximately 24 h of polarization measurements

9.2 Progress Toward a Quantum Memory

The quantum memory that is under development at ARL for the QNET-AP DSI[1] uses cold ^{87}Rb in a MOT as the fundamental component for the quantum memory. The choice of ^{87}Rb was due to the relatively long coherence time. An image of the atomic memory in our laboratory with the atomic ensemble operating in the MOT is shown in Fig. 61

A MOT of ^{87}Rb atoms produces an optically thick atomic ensemble for our experiment. The vacuum system is the Cold Quanta miniMOT^{TM} consisting of a vapor cell, Rb getter, ion pump, and a set of current carrying coils in anti-Helmholtz configuration. The coils produce a quadrupole magnetic field at the center of vapor cell with a gradient of 10 $\frac{Gauss}{cm \cdot A}$. Three sets of current carrying coils in Helmholtz configuration are mounted on the system to compensate for ambient, bias magnetic fields.

The cooling and repump laser light required for the MOT are provided by Toptica TA Pro and Vortex II laser systems, respectively. Approximately 80 mW of cooling light, detuned 18 MHz below the $5S_{1/2}$ F = 2 → $5P_{3/2}$ F = 3 transition in ^{87}Rb, and 5 mW of repump light, on resonance with the $5S_{1/2}$ F = 1 → $5P_{3/2}$ F = 2 transition, are delivered collinearly to the miniMOT^{TM} system. Three orthogonal beams of circularly polarized light are produced

87
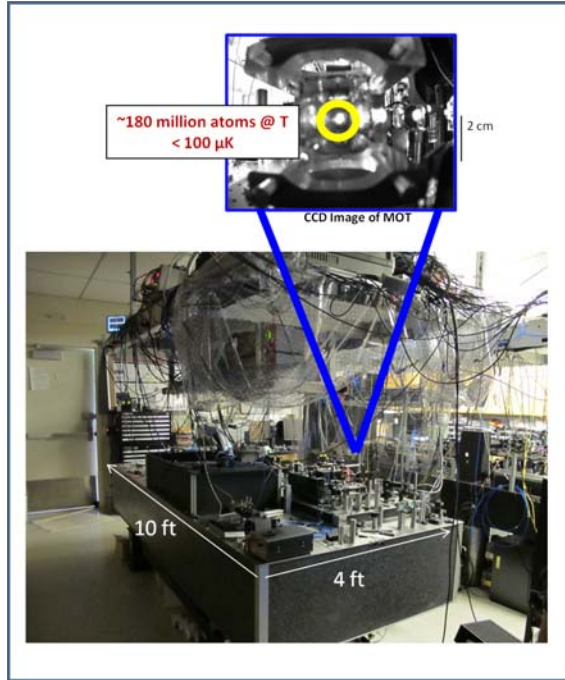
Fig. 61 MOT setup

via mirrors, polarizing beamsplitters, $\lambda/2$, and $\lambda/4$ waveplates. Each beam is retro-reflected and has its polarization flipped once passing through the vapor cell by a compound mirror consisting of a highly reflecting mirror and quarter-wave plate. This configuration of optical fields, along with the quadrupole magnetic field, produces a velocity damping, spatially trapping system that can produce very cold, very dense ensembles. Loading from a room-temperature Rb vapor, a cloud of ~1.8 x 10^8 ^{87}Rb atoms at a temperature of ~100 μK is produced in roughly 5 s (Fig. 62).
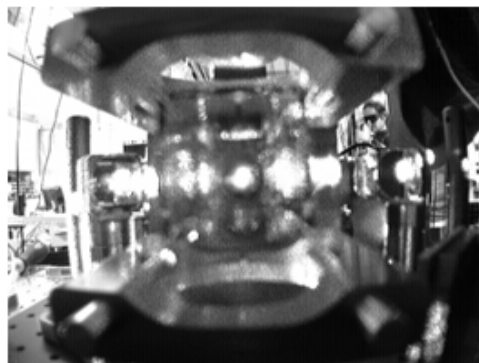

Fig. 62 QNET-AP ^{87}Rb cold atom memory operation shown by light emitted at MOT center

9.2.1 Quantum Memory Operation

The hyperfine ground state levels of ^{87}Rb ($5S_{1/2}$, $F_{a,b} = 1,2$) serve as the initial ($|b\rangle$) and storage ($|a\rangle$) states of the quantum memory. The $5P_{1/2}$, $F = 2$ ($5P_{3/2}$, $F = 2$) state is the excited state $|c\rangle$($|d\rangle$) in the write (read) procedure. A MOT of ~10^8 Rb atoms is formed in 5 s. Then the quadrupole magnetic field is turned off, the cooling light 2 ms later, and the repump light 2 μs after that, leaving all of the atoms in the $5S_{1/2}$, $F = 2$ ground state. A sequence of 1,000 trials with duration ~1 μs is performed as follows: a weak write pulse, tuned 20 MHz below the transition, is shone on the atomic ensemble (Figs. 63 and 64).
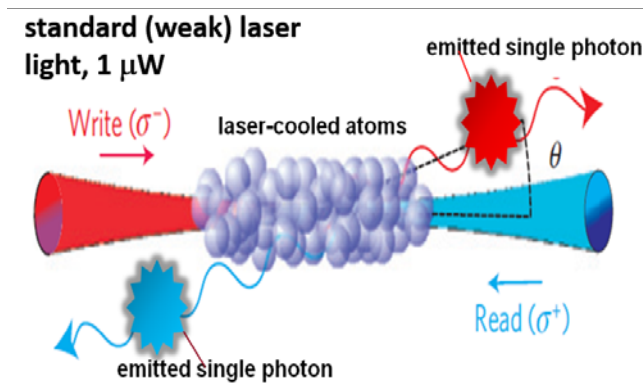

Fig. 63 Graphical representation of a typical cold atom close atomic memory

For a low enough excitation probability (10^{-3}–10^{-4}), a photon detection in the signal arm heralds the transfer of 1 atom from $F = 2$ to the $F = 1$ ground state. The polarization of the generated single photon is orthogonal to the write pulse.

When the weak laser light (1 μW) excites the laser-cooled atoms, the state of the atomic system can be described by Fig. 65. Because it is unknown which atom is excited, collective interference will lead the ensemble to emit 1 photon.

After a hold time of 300 ns, a strong, resonant read pulse of duration 500 ns interacts with the ensemble, producing a photon in the idler arm that is then detected by a silicon avalanche photodiode (APD). The idler photon has a polarization orthogonal to the read pulse (Fig. 64). The APD signals are sent to a time-interval analyzer to measure the time intervals between detections in the signal and idler arms. The experimental layout to measure the single photon emission from the atomic memory is shown in Fig. 66. D1 would measure the photon emitted when the memory has a "write" operation performed on it. Detectors D2 and D3 measure the photon emitted after a "read" operation. The strength of the correlations between the photon-pairs generated by the atomic ensemble can be measured by the normalized intensity
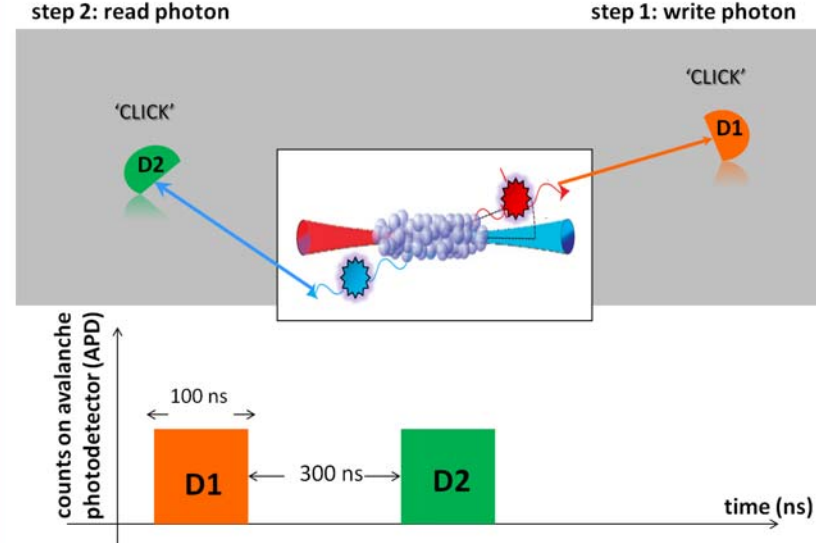
Fig. 64 Write-read single photon measurement setup

$$\Psi = |1,0,0,0...> + |0,1,0,0...> + |0,0,1,0...> + ...$$

Fig. 65 State of ensemble atomic memory

cross-correlation function,

$$g_{i,s}^{(2)} = \frac{p_{i,s}}{p_i p_s} \tag{69}$$

where $p_{i,s}$ is the probability to detect a photon pair and $p_i p_s$ are the probabilities to detect a photon in the idler and signal arms, respectively. A measurement of $g_{i,s}^{(2)} > 2$ implies that the correlations are nonclassical in nature. As shown in Fig. 67, the experimental data indicate that the quantum memory with write-read is operating in a quantum regime. Figure 68 provides further analysis of the measured photon counts from read-write experiments performed on the SEDD atomic memory. Delayed coincidence measurements between detectors D1-D2 and D1-D3 are indicative of a successful write-read operation. The insignificant number of D1-D2-D3 coincidences is indicative that the memory is emitting only a single photon for the write operation and the read operation. Additionally, the estimated entanglement rate calculation for the SEDD atomic memory is presented in Fig. 69

90
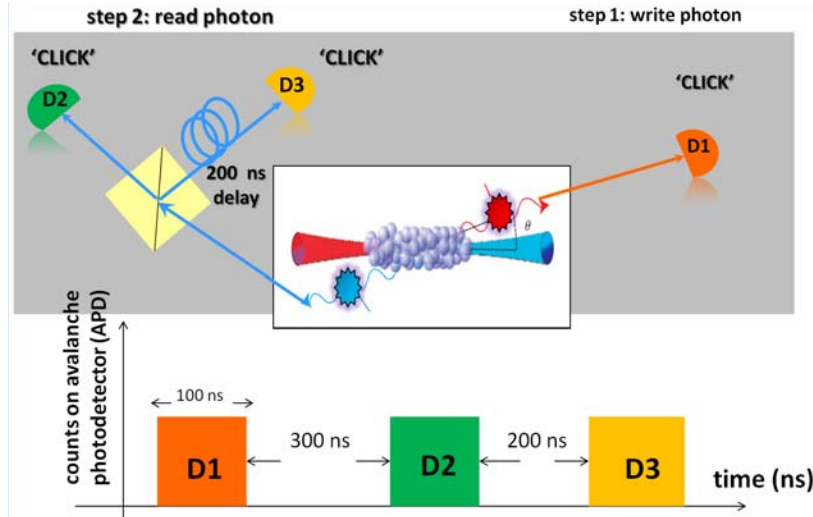
Fig. 66 Setup for single photon determination
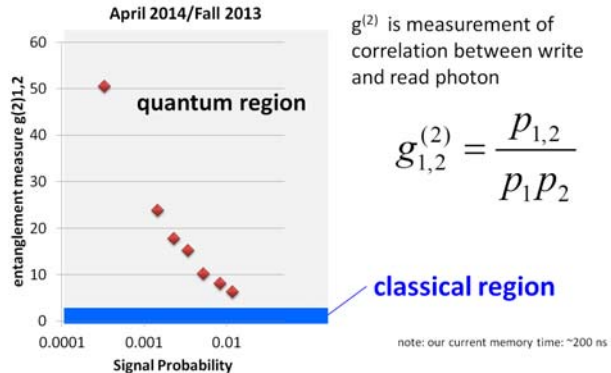
Fig. 67 These data demonstrate temporal quantum entanglement between write and read photons

9.2.2   Summary

In summary, we successfully trapped cold ^{87}Rb atoms in a MOT (Fig. 62), a system that is suitable for quantum memory and quantum frequency conversion via FWM. The 13.5-km distance from ARL to JQI requires the coherence of the quantum memory to be at least 45 μs, which a cloud of ^{87}Rb atoms in a MOT should be able to achieve (~100-μs coherence time). The write step was accomplished through an off-resonant Raman process, for which we had the laser and the optoelectronics to control, and the read step was accomplished through resonant scattering. We achieved initial implementation of hardware and software for controlling the lasers and electronics for the memory read/write processes.[1]

Progress needs to be made improving the memory lifetime (less than 1 μs), readout efficiency (~2%), and increasing the single photon generation rate (~1 kHz) to make the implementation

91
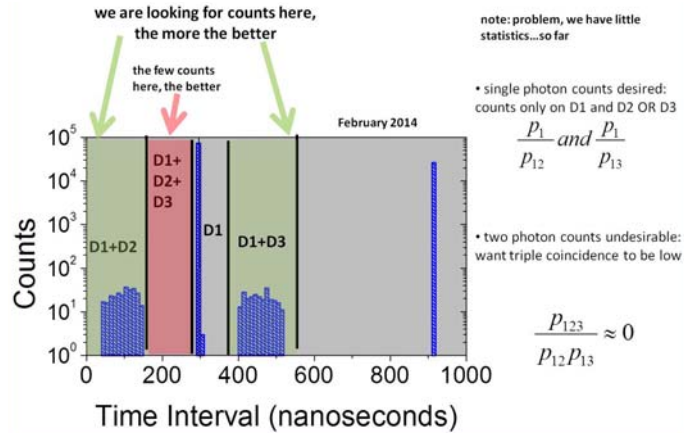
Fig. 68 Experimental results showing quantum corelated single photons
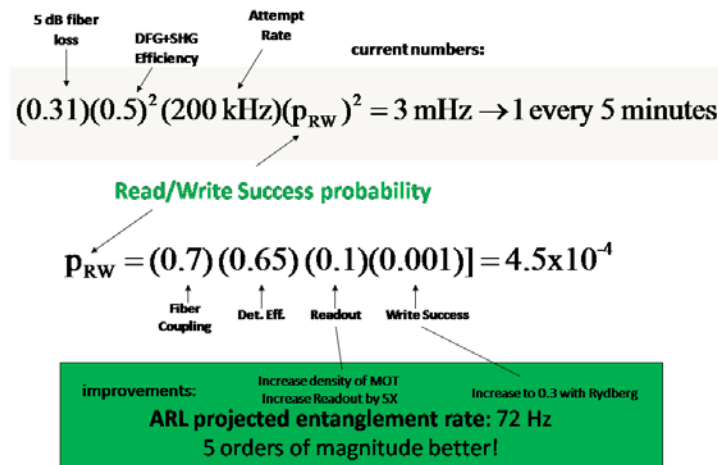
Fig. 69 Entanglement rate calculation for atomic memory

of a quantum repeater practical. The memory lifetime can be extended to greater than 1 s by optically pumping the atoms into a clock state and trapping them in an optical lattice. The readout efficiency can be increased to greater than 90% by increasing the optical depth of the atomic ensemble. Rydberg atoms are a promising platform for increasing the generation of entangled photons to nearly 1 MHz. Rydberg atoms are very good single photon sources due to the Rydberg blockade, which prevents multiple excitations within the Rydberg radius. The inclusion of these techniques should allow the practical implementation of a quantum repeater in a quantum communication network.[1]

9.3 Filtering for Cold Atom Quantum Memories

To mitigate some extraneous noise photon measurements from the quantum memory SEDD developed and experimentally tested the use of a ^{85}Rb vapor cell to attenuate pump laser photons and spontaneous emissions from the cold ^{87}Rb quantum memory. A paper with the results from these experiments by Daniel Stack, Patricia Lee, and Qudsia Quraishi titled "A Simple and Efficient Absorption Filter for Single Photons from a Cold Atom Quantum Memory," was published in Optics Express on 5 Mar 2015.[2] The abstract of the paper is presented below:

"The ability to filter unwanted light signals is critical to the operation of quantum memories based on neutral atom ensembles. Here we demonstrate an efficient frequency filter which uses a vapor cell filled with ^{85}Rb and a buffer gas to attenuate both residual laser light and noise photons by nearly two orders of magnitude with little loss to the single photons associated with our cold ^{87}Rb quantum memory. This simple, passive filter provides an additional 18 dB attenuation of our pump laser and erroneous spontaneous emissions for every 1 dB loss of the single photon signal. We show that the addition of a frequency filter increases the non-classical correlations and readout efficiency of our quantum memory by 35%."[2]

The measured results from these experiments indicate that a 35% increased readout rate efficiency can be achieved through the use of the ^{85}Rb vapor cell as a filter. These results are important to maximizing the operating parameters that are critical to the realization of a quantum network based on neutral atom quantum memories.[2]

9.4 SEDD Accomplishments and Conclusions

Our accomplishments can be summarized as follows. We constructed new atom-based vacuum chamber setup, established quantum memory in laser-cooled atoms, and designed architecture and obtained components to do quantum frequency conversion. In conclusion, we have achieved quantum correlated photons; however, we need to improve rates. We have quantified 27-km fiber polarization drift and will be able to stabilize it. We have determined that determined that entanglement rates must be improved for viable transmission rates. Our next steps include increasing optical density to improve rates. We need to achieve quantum frequency conversion of single 780-nm atomic photons into 1324-nm telecom photon. We

93

need to demonstrate single photon emission of write, read, and telecom photons to establish polarization control over ARL/JQI fiber. We have already started in-lab tests with a fiber spool.

9.4.1 Collaborations

We established strong local and international collaborations with preeminent scientists, including Prof. Winfield Hensinger, Univ of Sussex, England, scalable quantum system; Prof. Dzmitry Matsukevich, Univ of Singapore, atom-based quantum memories; and Prof. Steve Rolston, JQI, remote quantum systems.

9.4.2 Publications

The following are publications and presentations by SEDD personnel accomplished during the QNET-AP project:

D Stack, PJ Lee, Q Quraishi, A simple and efficient absorption filter for single photons from a cold atom quantum memory. Optics Express 6822 (5 Mar 2015).

D Stack, P Lee, Q Quraishi, Progress toward a quantum memory with telecom wavelength conversion. Proc. SPIE 9123, 91230D-7 (2014).

D Stack, I Grissom, P Tang, PJ Lee, Q. Quraishi, A quantum memory with telecom-wavelength frequency conversion. Technical Report (in progress) (2014).

D Stack, Cold atom quantum memory and quantum frequency conversion for use in a quantum network. ARL Seminar (15 Jan 2015).

D Stack, I Grissom, P Lee, Q Quraishi, Optimization of a quantum memory with telecom-wavelength conversion. American Physical Society, Division on Molecular and Optical Physics, (DAMOP) (2014).

D Stack, Q Quraishi, P Lee, Progress towards a quantum memory with telecom-wavelength conversion. SPIE International Symposium on Defense, Security and Sensing (2014).

D Stack, I Grissom, P Lee, Q Quraishi, Towards a quantum memory with telecom-wavelength conversion. Southwest Quantum Information and Technology (SQUINT) Meeting (2014).

D Stack, P Lee, Q Quraishi, Progress toward a quantum memory with telecom wavelength conversion, SPIE Baltimore, 2014.

D Stack, Q Quraishi, I Grissom, RE Meyers, KS Deacon, A Tunick, P Lee, Progress toward

a quantum memory with telecom wavelength conversion. American Physical Society (5 June 2013).

D Stack, Q Quraishi, P Lee, I Grissom, R Meyers, K Deacon, A Tunick, Progress towards a quantum memory with telecom-wavelength conversion. American Physical Society, Division of Atomic, Molecular & Optical Physics (DAMOP) (Poster) (2013).

Q Quraishi, D Stack, P Lee, Quantum frequency conversion of atomic ensembles with PPLN. Southwest Quantum Information and Technology (SQUINT) (Poster) Meeting (2013).

RE Meyers, P Lee, KS Deacon, A Tunick, Q Quraishi, D Stack, A quantum network with atoms and photons. Proc. SPIE 8518, 8518–14 (2012).

9.5   References

1.   Stack, D, Lee, P, Quraishi, Q. Progress toward a quantum memory with telecom wavelength conversion. Proc. SPIE 9123. 2014; 91230D-7.

2.   Stack, DT, Lee, PJ, Quraishi, Q. A simple and efficient absorption filter for single photons from a cold atom quantum memory. Optics Express Optics. 2015; 23, 6822.

List of Symbols, Abbreviations, and Acronyms

AFOSR	Air Force Office of Scientific Research
APD	avalanche photodiode
APT	acquisition, pointing and tracking
ARL	US Army Research Laboratory
ARO	Army Research Office
BBO	beta-barium borate
CC	coincidence counts
CHSH	Clauser-Horne-Shimony-Holt
CISD	Computational and Information Sciences Directorate
CPDS	correlated photon detection system
DFG	difference frequency generation
DLCZ	Duan, Lukin, Cirac, and Zoller
DM	dichroic mirror
DOD	Department of Defense
DOE	Department of Energy
DSI	Director's Strategic Initiative
EIT	electromagnetically induced transparency
EOARD	Air Force European Office of Aerospace Research & Development
FWM	four-wave mixing
GPS	global positioning system
HBT	Hanbury-Brown and Twiss
HOM	Hong-Ou-Mandel
ICFO	Institute of Photonic Sciences
ITC	International Technology Center
JQI	Joint Quantum Institute

LBO	lithium borate
LLM	laser line mirror
MOT	magneto optical trap
NGIC	National Ground Intelligence Center
NIST	National Institute of Standards and Technology
ONR	Office of Naval Research
OTDR	optical time-domain reflectometer PBS polarized beam splitter
PCMC	photon coincidence measurement component
PM	polarized-maintained
PMD	polarization mode dispersion
POVM	positive operator valued measurement
PPLN	periodically poled lithium niobate
PZT	piezoelectric transducer
QNET-AP	Quantum Network with Atoms and Photons
QWP	quarter wave plate
RDECOM	US Army Research Development & Engineering Command
SEDD	Sensors and Electron Devices Directorate
SPDC	Spontaneous Parametric Down conversion
TAMU	Texas A&M University
UMBC	University of Maryland, Baltimore County
USPTO	US Patent and Trademark Office
WDM	wave division multiplexer

1 (PDF)	DEFENSE TECHNICAL INFORMATION CTR DTIC OCA
2 (PDF)	DIRECTOR US ARMY RESEARCH LAB RDRL CIO LL IMAL HRA MAIL & RECORDS MGMT
1 (PDF)	GOVT PRINTG OFC A MALHOTRA
5 (PDF)	DIRECTOR. US ARMY RESEARCH LAB RDRL CI A KOTT RDRL CIN-T B RIVERA R MEYERS K DEACON RDRL CII-A A TUNICK